UNIVERSIDADE DE LISBOA
INSTITUTO SUPERIOR TÉCNICO

Günther Uecker, *1987*

Numerical modeling of fully coupled solid-fluid flows

Ricardo Jorge Fonseca Birjukovs Canelas

Supervisor:	**Doctor Rui Miguel Lage Ferreira**
Co-Supervisor:	**Doctor Ramón Gómez-Gesteira**

Thesis approved in public session to obtain the PhD Degree in Civil Engineering

Jury final classification: Pass with Distinction

Jury

Chairperson: Chairman of the IST Scientific Board

Members of the Committee:
    Doctor João Gouveia Aparício Bento Leal
    Doctor Ramon Gómez-Gesteira
    Doctor Ramiro Joaquim de Jesus Neves
    Doctor Alejandro Jacobo Cabrera Crespo
    Doctor Rui Miguel Lage Ferreira
    Doctor Carlos Manuel Tiago Tavares Fernandes

2015

UNIVERSIDADE DE LISBOA
INSTITUTO SUPERIOR TÉCNICO

Numerical modeling of fully coupled solid-fluid flows

Ricardo Jorge Fonseca Birjukovs Canelas

Supervisor:	Doctor Rui Miguel Lage Ferreira
Co-Supervisor:	Doctor Ramón Gómez-Gesteira

Thesis approved in public session to obtain the PhD Degree in Civil Engineering

Jury final classification: Pass with Distinction

Jury

Chairperson: Chairman of the IST Scientific Board

Members of the Committee:
Doctor João Gouveia Aparício Bento Leal, Professor, Faculty of Engineering and Science, University of Agder, Norway
Doctor Ramon Gómez-Gesteira, Professor Catedrático de la Faculdad de Ciencias, Universidad de Vigo, Spain
Doctor Ramiro Joaquim de Jesus Neves, Professor Associado do Instituto Superior Técnico, Universidade de Lisboa
Doctor Alejandro Jacobo Cabrera Crespo, Investigador de la Faculdad de Ciencias, Universidad de Vigo, Spain
Doctor Rui Miguel Lage Ferreira, Professor Auxiliar do Instituto Superior Técnico, Universidade de Lisboa
Doctor Carlos Manuel Tiago Tavares Fernandes, Professor Auxiliar do Instituto Superior Técnico, Universidade de Lisboa

Funding Institutions

2015

Remember that all models are wrong; the practical question is how wrong do they have to be to not be useful.

George E.P. Box and Norman R. Draper, Empirical Model-Building and Response Surfaces (1987)

Acknowledgments

Existe muito por que estar grato aos meus pais. O sacrifício e a alegria com que o cometeram, as longas horas a lidar com uma mente incassiável, o ninho sempre pronto a que recorrer quando o mundo se demonstrou demasiado ventoso. A vós.

Ao Luís e Ana, pela infindável disponibilidade, pelo genuíno interesse, pelo carinho sem fim. A vós.

Ao meu irmão Diogo, pela presença e apoios constantes quando os dias assim o pedem. Pelas conversas, discussões e olhares de muitos anos de cumplicidade, a ti.

Aos meus tios, pelo sempre presente sorriso, boa disposição e óptimos conselhos de viagem. Pelo incondicional amor e disponibilidade com que sempre me presentearam.

I have been fortunate enough to share the stimulating working environments of two research groups. In all of CEris, I would like to thank particularly Ana Margarida, for proudly sharing the same space with someone as dubious as a numerics researcher. Daniel Conde for always being ready to defend the said numerics researcher, besides sharing my pains with compilers. To Artur Silva, for always bringing a new perspective, and particularly good 7th art recommendations. To Pedro Sanches, for transforming my descents into the pits of physical experimentation into highly enjoyable moments. I would also like to acknowledge Dulce Fernandes, Nuno Martins, Ana Quaresma, Rui Aleixo and Luis Mendes.

Part of my work was developed in UVigo, at EPHYSLAB, Ourense. Alejandro Crespo deserves special acknowledgment for the sheer effort to make me feel welcome and part of the team. Alex employed the full extend of his availability and critical approach to promote this work to a better level. He also took the entire team to the thermal baths whenever possible, in a great contribution towards the understanding of fluid mechanics. José Dominguéz shared many hours looking at code and compiler warnings. I am ever so thankful to him, knowing that he made this work possible by helping me express my ideas within the computational maze that the project grew into. Anxo Barreiro, I will never forget that couch. A very big thank you to Angel Fernandez, Fran Santos, Orlando Feal, Xurxo, Corrado Altomare and Carlos Alvarado.

Behind a PhD there is always a well of vision, experience and support. I had two, Rui Ferreira and Rámon Gómez-Gesteira, my advisors. To both, I need to acknowledge the great opportunities that I was presented with. The amount of knowledge, patience and dedication devoted to this project make me proud, humbled and thankful.

To FCT, for supporting the program with a full PhD scholarship, a fundamental requisite for its

development.

To Olya, my wife, confidant and everything positive one can be to another. For sharing everything, for transmuting the good into sublime and the bad to part of the good. For the endless monologues you had to endure and the love you poured into every attempt at supporting me. To you.

Abstract

Flows of solid-fluid mixtures pose persistent challenges to our conceptualization, experimentation and modeling capabilities. The wide array of possibly relevant scales, both spatial and temporal, have prevented the design of models capable of providing useful solutions for complex, multi-scale situations. Competent models are applied to very specific scales and types of flow, facing severe problems out of their narrow domain of application.

Direct observation and measurement of many of these flows quantities are difficult or impossible to achieve, justifying the limited amount of literature on the subject of more robust conceptual models. With increasing computational capabilities, there is hope that highly resolved models with small number of assumptions can lead to approximate solutions for these flows. This has the potential to impose new research prompts, leading to better understandings of the phenomena.

The key objective of this dissertation is to introduce a unified discretisation of rigid solids and fluids, allowing for resolved simulations of fluid-solid phases within a meshless framework. The numerical solution, attained by Smoothed Particle Hydrodynamics (SPH) and a variation of Discrete Element Method (DEM), the Distributed Contact Discrete Element Method (DCDEM) discretisations, is achieved by directly considering solid-solid and solid-fluid interactions. The novelty of the work is centered on the generalization of the coupling of the DEM and SPH methodologies for resolved simulations, allowing for state-of-the-art contact mechanics theories to be used in arbitrary geometries, while fluid to solid and vice versa momentum transfers are accurately described. The methods are introduced, analyzed and discussed.

A series of experimental campaigns are devised to serve as validation for complex solid-fluid flows simulations and together with analytical and other benchmark numerical solutions, allow for a comprehensive characterization of the model. Unique experiments were performed, such as dam-break flow with movable objects and settling dynamics of macroscopic solid particles. For the dam-break tests, a set of blocks is placed in several configurations and then subjected to the bore and subsequent unsteady flow. Blocks are tracked and positions are then compared between experimental data and the numerical solutions. A PIV technique allows for the quantification of the flow field and direct comparison with numerical data. The results show that the model is accurate and is capable of treating highly complex interactions, such as transport of debris or unsteady hydrodynamic actions on structures, if relevant scales are reproduced. The settling case allowed to guarantee that relevant hydrodynamic forces are correctly modeled.

Preliminary results in limit cases are presented and discussed. These are cases whose numerical

treatment has proven challenging for other models and experimental initiatives are either expensive or limited in the amount of data that can be extracted.

Keywords

Resumo

Escoamentos multifásicos de material fluido e sólido representam um desafio às actuais capacidades de experimentação, conceptualização e modelação. O grande leque de escalas, quer temporais quer espaciais, envolvidas nestes fenómenos parece ter prevenido o desenvolvimento de modelos capazes de fornecer soluções atraentes para casos complexos, onde estas várias escalas são relevantes. Modelos competentes são aplicados tipicamente a escoamentos específicos, com escalas bem definidas, sofrendo de severos problemas fora do seu estreito domínio de aplicabilidade.

Observação directa, assim como medição de muitas quantidades neste tipo de escoamentos torna-se díficil ou impossível com os meios actuais, justificando-se assim a rarefeita literatura em modelos conceptuais robustos. Com o actual ritmo de crescimento de recursos computacionais, existe a esperança de que modelos resolvidos, com um número mínimo de hipoteses, possam levar a soluções aproximadas para estes escoamentos. Tais soluções terão o potencial de promover novas perguntas para investigar, levando a uma melhor compreensão dos fenómenos envolvidos.

O objectivo chave desta dissertação é a introdução de uma discretização sem malha unificada para sólidos rígidos e fluidos, permitindo a elaboração de simulações resolvidas de ambas as fases. A solução numérica, obtida por Smoothed Particle Hydrodynamics (SPH) e uma variante de Discrete Element Method (DEM), o Distributed Contact Discrete Element Method (DCDEM), é fruto da caracterização directa e local de contactos sólido-sólido e das interfaces sólido-fluido. A inovação do trabalho está centrada na generalização do acoplamento entre os métodos SPH e DEM para simulações resolvidas. Isto permite que teorias estado-da-arte para mecânica de contacto posam ser usadas em geometrias aleatórias, assim como o tratamento de tranferências de quantidade de movimento entre as fases sólida e fluida. Os métodos são introduzidos e analisados em detalhe.

Uma série de campanhas experimentais foi desenhada de modo a fornecer validação para simulações de escoamentos complexos. Juntamente com soluções analíticas e outras soluções numéricas encontradas na literatura, procede-se à caracterização do modelo quanto à qualidade das suas soluções. Experiências inéditas foram levadas a cabo, como escoamento do tipo rotura de barragem com objectos móveis a jusante e medição de velocidades de sedimentação de partículas macroscópicas. Para os casos de rotura de barragem, um conjunto de blocos foi colocado em várias configurações e depois sujeito à onda de frente abrupta e subsequente escoamento não-permanente. Os blocos são seguidos e as suas posições ao longo do tempo servem de comparação com os resultados numéricos. Uma técnica de Particle Image Velocimetry (PIV) permite a medição do campo de velocidade no local de impacte e uma comparação directa com os resultados numéricos. Os resultados apontam para a precisão do

modelo, assim como a capacidade de lidar com interações complexas, como o transporte de detritos ou quantificação de acções hidrodinâmicas não permanentes em estruturas. O caso de sedimentação confirma que as forças hidrodinâmicas relevantes são bem reproduzidas.

Resultados preliminares em casos limite são apresentados e discutidos. Estes são casos onde o tratamento numéricos se demonstra desafiante para outros modelos e iniciativas experimentais são simplesmente demasiado dispendiosas ou limitadas na quantidade de informação que podem recuperar.

Palavras Chave

Escoamentos multifásicos, Métodos sem malha, Smooth Particle Hydrodynamics, Discrete Element Method, Escoamento de detritos, Leis de contacto, Transporte sólido, Computação de alta performance, Impulsão, Validação

Contents

List of Figures

List of Tables

Abbreviations

CFL Courant-Friedrichs-Lewy

CPU Central Processing Unit

CUDA Compute Unified Device Architecture

DCDEM Distributed Contact Discrete Element Method

DEM Discrete Element Method

DTL Direct Linear Transform

DOF Degrees of Freedom

DNS Direct Numerical Simulation

EOS Equation of State

GPU Graphics Processing Unit

HPC High-Performance Computation

IBM Immersed Boundary Method

IVP Initial Value Problem

JKR Johnson, Kendall and Roberts

LES Large Eddy Simulation

MPI Message Passing Interface

MPS Moving Particle Simulation

PIV Particle Image Velocimetry

PDE Partial Differential Equations

RANS Reynolds-averaged Navier-Stokes Equations

SPH Smooth Particle Hydrodynamics

SPS Sub-Particle Stress

VOF Volume of Fluid

WCSPH Weakly Compressible Smooth Particle Hydrodynamics

PIC Particle-in-cell

PFEM Particle Finite Element Method

FEM Finite Element Method

RMSE Root Mean Square Error

List of Symbols

Symbol	Description	Dimensions
a	Contact radius	$[L]$
C_S	Smagorinsky constant	$[-]$
C_s	Sound celerity	$[LT^{-1}]$
$d95$	Particle diameter larger than 95% of the entire reported distribution	$[L]$
$\boldsymbol{D}$	Strain rate tensor	$[T^{-1}]$
Dp	Particle diameter, interparticle spacing	$[L]$
e_n	Normal restitution coefficient	$[-]$
E	Young modulus	$[ML^{-1}T^{-2}]$
E^*	Generalized Young modulus	$[ML^{-1}T^{-2}]$
$\boldsymbol{F}_\Omega$	Force source term per unit volume	$[ML^{-2}T^{-2}]$
$\boldsymbol{F}_g$	Gravitational force per unit mass	$[LT^{-2}]$
$\boldsymbol{F}_n$	Normal force	$[MLT^{-2}]$
$\boldsymbol{F}_t$	Tangential force	$[MLT^{-2}]$
$\boldsymbol{g}$	Gravitational acceleration vector	$[LT^{-2}]$
h	Smoothing length	$[L]$
$\boldsymbol{I}_k$	Rigid body inertia tensor	$[ML^2]$
$\boldsymbol{I}$	Identity matrix	$[-]$
k_n	Normal stiffness constant	$[MT^{-2}]$
k_t	Tangential stiffness constant	$[MT^{-2}]$
$m, \ M$	Mass	$[M]$
M^*	Reduced mass of the system	$[M]$
p	Pressure	$[ML^{-1}T^{-2}]$
$\boldsymbol{r}$	Position vector	$[L]$
R^*	Generalized curvature radius	$[L]$
$\boldsymbol{R}_k$	Rigid body center of mass	$[ML^2]$
s	Slit spacing	$[L]$
t	Time	$[T]$
t_c	Collision duration	$[T]$
$\boldsymbol{T}$	Contact force per unit area	$[ML^{-1}T^{-2}]$
$\boldsymbol{u}$	Velocity vector	$[LT^{-1}]$
u_k	Velocity component	$[LT^{-1}]$
$\overline{\boldsymbol{u}}$	Imposed velocity vector	$[LT^{-1}]$
$\boldsymbol{n}$	Outward normal unit vector	$[-]$
V	Volume	$[L^3]$
$\boldsymbol{V}_k$	Rigid body velocity	$[LT^{-1}]$
W	Interpolation kernel	$[-]$
ρ	Density	$[ML^{-3}]$
ρ_0	Reference density	$[ML^{-3}]$
$\boldsymbol{\sigma}$	Cauchy stress tensor	$[ML^{-1}T^{-2}]$
$\overline{\boldsymbol{\sigma}}$	Imposed Cauchy stress tensor	$[ML^{-1}T^{-2}]$
$\boldsymbol{\tau}$	Shear stress tensor	$[ML^{-1}T^{-2}]$
μ	Shear viscosity coefficient	$[ML^{-1}T^{-1}]$
μ_f	friction coefficient	$[-]$
λ	Bulk viscosity coefficient	$[ML^{-1}T^{-1}]$
ν	Kinematic viscosity coefficient	$[L^2T^{-1}]$

ν_p	Poisson ratio	$[-]$
δ	Indentation depth, spring compression	$[L]$
$\boldsymbol{\tau}^*$	SPS stress tensor	$[ML^{-1}T^{-2}]$
ν_t	Eddy viscosity	$[ML^{-1}T^{-1}]$
δ_Φ	δ-SPH coefficient	$[-]$
$\boldsymbol{\Omega}_k$	Rigid body angular velocity	$[T^{-1}]$
γ_n	Normal damping constant	$[MT^{-1}]$
γ_t	Tangential damping constant	$[MT^{-1}]$
γ_s	Slit density	$[-]$
Ω	Domain or Material system of particles	$[-]$
Ω'	Domain centered at point of interest	$[-]$
Ω_0	Ω' translated to origin	$[-]$
Ω_L	Spatial domain	$[-]$
$\partial\Omega_L$	Boundary of spatial domain	$[-]$
$d\Gamma$	Surface element	$[-]$
$\partial\Omega_B$	Solid boundaries	$[-]$
$\partial\Omega_B$	Free surface boundaries	$[-]$

1

Introduction

1. Introduction

1.1   Mathematical Modeling of Solid-Fluid Flows, an Overview

Flows of solid-fluid mixtures cover a large spectrum of scales: from particles so small that its kinematics are dominated by random molecular motion, to groups of kilometre-wide icebergs being dragged by oceanic currents, in geophysical settings. Such flows, however, present a series of challenges for both experimental and numerical research. In an experimental campaign, efficient techniques used in single-phase measurements such as hot-wire anemometry, Laser Doppler Anemometry (LDA) or Particle Image Velocimetry (PIV), only provide accurate measures of the velocity field if the flows are dilute and the particles are relatively small. Measuring solid concentration and local variations is equally problematic. As only recently non-intrusive techniques, such as Nuclear Magnetic Resonance (Fukushima, 1999; Lemonnier, 2010), are being explored to study these flows, optical methods continue to be the main approaches (Douxchamps et al., 2002; Armanini et al., 2008), again with serious difficulties for dense and highly three-dimensional flows (Spinewine et al., 2003).

In a similar fashion, numerical simulations of solid-liquid flows are demanding because of the complex geometries and the types of momentum transfer modes that arise from the fluid-solid interactions. Accurate and numerically efficient simulations are of substantial importance for research and industrial fields, as they allow to derive many important constitutive relations and further research prompts. A special success story, close to the current topic would be dry granular flows. Considering mainly spherical particles, interactions are easier to approximate, resulting in a large body of work being produced (Campbell, 2006), with profound implications in the industry.

Due to the difficulties associated with the modeling of solid-fluid flows, simulations are usually constrained to a relatively small range of the scale spectrum. Several proposals for unresolved models were presented, both in coupled and uncoupled versions (Calantoni et al., 2004; Robinson et al., 2014; Cleary, 2014). These rely on the parametrization of the bulk solid-fluid interactions. Resolved models are also typically scale specific, as the solid fraction is generally described by spherical Discrete Element Method (DEM) particles (Potapov et al., 2001; Kempe and Fröhlich, 2012) and special considerations to account for contact lubrication are derived from small scale experimental studies, such as the works of Yang and Hunt (2006) and Joseph et al. (2001).

The model presented in this thesis was designed to accommodate the concerns common in several technical disciplines, including coastal, offshore, maritime and a large part of fluvial engineering. In these disciplines, the common simplification that the solid material is perfectly rigid allows for robust solutions to a large array of problems. A computational model capable of providing meaningful solutions for the interaction of fluid and rigid solid objects is a valuable tool for the quantification of severity of hydrodynamic actions in several contexts, including risk assessment studies, design of floating bodies or design of exposed structures. Such tool must be computationally scalable, should be able to model all physically relevant scales which fluid-solid interaction occurs. In most engineering applications involving fluids and structures, solid objects are much larger than the smallest flow scales. For instance, viscous modes of momentum transfer are often negligible since the involved Reynolds numbers are normally large (Shu et al., 2011). However, the relevant modes of interaction are not always

evident, in which case the model must be designed to offer high spatial and temporal resolutions. Also, to minimize the influence of imposed non-physical boundaries (lateral walls or periodic zones in an open beach for example), some simulations require remarkably large domains. This highlights the need for high performance models and implementations. Finally, such models should be based on consistent conceptual models, i.e. systems of conservation equations and closure equations, avoiding *ad hoc* formulations, and should be subjected to a discretization that preserves the key mathematical properties of the conceptual model. All of the required characteristics point to the need for a resolved model, in order to cope with complex geometries and the range of potentially important spatial and temporal scales.

Three-dimensional, fully coupled and interface-resolving simulations of flows with arbitrary numbers of solid particles have attracted considerable attention from the academic environment. Within the mesh-based ideas, the Immersed Boundary Method (IBM), as originally proposed by Peskin (1977), has arguably been the most adapted (Prosperetti and Tryggvason, 2007). The basic idea of this approach is to employ a mesh for the discretization of the fluid phase and to represent the immersed fluid-solid interface by surface markers. In order to satisfy the required boundary conditions at the interface additional source terms are used in the momentum equation. Fekken (2004) coupled a Volume of Fluid (VOF) method to a quarterion solver by using a modified IBM version. It allowed for complex flows with simple geometries to be studied, including the effects of the free-surface, but no solid-solid considerations were made. The main problem with the meshed approach is the growing numerical and computational complexity with growing scene complexity. This imposes hard limits on the applicability of models that are not tailor tuned to a specific application, as optimization as data management become increasingly difficult.

Within the meshless framework, efforts have been made on unifying solid and fluid modeling. Koshizuka et al. (1998) modeled a rigid body as a collection of Moving Particle Simulation (MPS) fluid particles that keep their relative distance by default. This has become the standard approach due to its simplicity and elegance. Monaghan et al. (2003) and Rogers et al. (2010), employing the same principle, modeled the effects of wave interaction on rigid bodies resorting to Smooth Particle Hydrodynamics (SPH) and special considerations for the particles that belonged to the solid body, effectively including a form of frictional behavior. In his work, Potapov et al. (2001) used a standard DEM formulation to treat the solid phase, employing contact mechanics formulations. The fluid phase is treated with a standard SPH model, treating the interface between solid and fluid with a ghost particle method. This allows to interpolate the pressure and drag forces to the solid body, resolving the interface to the desired scale. Even limited to spherical solid bodies, the model presented unique results concerning neutrally buoyant particles contained between two plates for different solid fractions, fluid viscosities and shear rates, reproducing results from the Bagnold experiments (Bagnold, 1954).

Effective blends of meshed and meshless methods have been explored recently, such as Particle-in-cell (PIC) methods and Particle Finite Element Method (PFEM) (Liu, 2003). PIC methods have been used since the 50s, mostly in plasma and other high energy physics (Evans et al., 1957). It poses the same difficulties as most of the mesh based models, as Lagrangian particles are in fact being advected

on Eulerian fields. PFEM uses much of the Finite Element Method (FEM) formulation, with nodes that are moved at every time step, with a constant need for re-meshing (Oñate et al., 2004; Idelsohn et al., 2004). This imposes great computational complexity and limits the mapping of the code to massively parallel architectures, while allowing for seamless integration with decades FEM research and development.

1.2 Objectives and Structure of the Dissertation

The range of relevant spatial and time scales, coupled with potentially very complex geometries, has prevented the appearance of generalized models, that can claim to provide solutions for very different problems in the realm of solid-fluid flows. The main ambition of this dissertation is the development of a model capable of providing meaningful solutions to such problems. The scope of the work are problems of fluvial hydraulics such as debris flows, up to large scale industrial and urban problems such as large debris transport by fluid action. The key objectives are then to propose a model that is able to cope with truly arbitrary geometries, distinct bodies, of distinct materials interacting in a highly non-linear fashion with a highly unsteady, discontinuous flow, with relevant scales ranging from few centimeters to tens of meters. The proposed dissertation work draws inspiration from the seminal works of Koshizuka et al. (1998) and Potapov et al. (2001), effectively combining a general form of DEM, Distributed Contact Discrete Element Method (DCDEM), with an SPH formulation.

The basic tools to ensure the completion of the objectives are coincident with that of any work that attempts at mathematical modeling of any phenomena in any specific framework: i) the design of a sound conceptual model, composed of system of conservation equations, as well as all necessary closure equations, if the system is open; ii) the discretization of the system and the assembly of an appropriate numerical scheme and iii) validation of the model with the application to documented case studies, that were not used as a phenomenological basis for the conceptual model. A largely neglected component of exploratory numerical studies is the quality of the implementation and the adaptation of the devised scheme to High-Performance Computation (HPC) architectures. One of the fundamental premises of this work was precisely the possibility of use of the model under realistic conditions. Thus adding to the points previously presented, implementation of the numerical scheme using state-of-the-art techniques to ensure simultaneous readability, modularity, expandability and maximum performance of the code is a paramount objective.

Under these general guidelines, the detailed objectives are presented simultaneously as the structure of the thesis, so structured to reinforce the several steps that compose the work.

Chapter 2, dealing with the derivation of conceptual models that will serve as a basis for numerical discretization, has the objective of introducing a coherent language, both at the notation and phenomenological levels. Continuum descriptions are derived and an almost complete form of the final conceptual model is presented. Some of the phenomenology treated in this chapter, namely contact laws for solid-solid interactions, are a conundrum, at best. They correspond to a higher form of educated guesses, based on limited data on hard to observe microscopic events, but trivial to record macroscopic effects. The conceptual model is promoted in Chapter 2, but the final form of the contact

laws only appears in Chapter 3, as they are designed in discrete form.

Chapter 3 is devoted to introducing and analyzing fundamental aspects of the discretization methods, SPH and DEM. Known difficulties are explored in order to allow for an easier reading of the following chapters. The discrete operators of the SPH method are derived for generic problems, and applied to different phases trough the sections of the chapter. A rigid body formulation is introduced, enabling the coexistence of solid and fluid particles in the same solution. Further discussion of the contact laws that provide contact force estimates for the DEM model takes place. Numerical stability is discussed in an attempt to enforce a correct description of all involved time scales, on both models. The formulation roughly corresponds to the initial iterations of the model, first presented in Canelas et al. (2013) and Canelas et al. (2013). Canelas et al. (2015) and Canelas et al. (2015) provide a complete reference to the model. Portraying to the SPH model alone, the work follows Crespo et al. (2015) closely, since this dissertation feeds into the open source code DualSPHysics, developed in colaboration between teams at the Univerity of Vigo, University of Manchester and Instituto Superior Técnico.

Chapter 4 has the objective of addressing important implementation details. The algorithmic structure of the method is analyzed and used to expose possible parallelism and predictable bottlenecks. A superficial introduction to the structure of the code in its Central Processing Unit (CPU) and Graphics Processing Unit (GPU) manifestations is carried out, with special care to point out major differences and particular adaptations to the particularities of the architectures, loosely adhering to the work in Canelas et al. (2013) and also explored in Crespo et al. (2015). This chapter serves as a warning: performance comes at a cost, greatly deductible if the design process is integrated. The numerical scheme should be written in a way to maximize computability for a given computer architecture, at the risk of voting to irrelevance an otherwise successful or even revolutionary approach.

In Chapter 5, one of the fundamental requirements of mathematical modeling is fulfilled. The model is compared against known solutions for both canonical problems and more subtle cases. Analytical solutions, reference numerical results and original experimental campaigns were used to provide a broad spectrum testing program of the proposed model. Canelas et al. (2015) focused on fluid-solid interactions, corresponding to sections 5.2.1 and 5.2.2. Sections 5.2.4 and 5.2.5 follow the structure of the solid-solid and fluid-solid interaction validations presented in Canelas et al. (2015).

As the model is intended to provide data on scenarios currently inaccessible by other means, Chapter 6 provides initial results on such three cases. The large scale harbor case presented in section 6.2 draws from the work presented in Canelas et al. (2014).

Chapter 7 draws global conclusions, comments on the results of each individual chapter and provides a small series of recommendations for future developments.

List of published related works

- Canelas, R.B., Crespo, A.J.C., Domínguez, J.M., Gómez-Gesteira, M., and Ferreira, R.M.L. "SPH-DCDEM model for arbitrary geometries in free surface solid-fluid flows." Computer Physics Communications (2015) Submitted.

1. Introduction

- Canelas, R.B., Domínguez, J.M., Crespo, A.J.C., Gómez-Gesteira, M., and Ferreira, R.M.L. "A Smooth Particle Hydrodynamics discretization for the modelling of free surface flows and rigid body dynamics." International Journal for Numerical Methods in Fluids (2015), 78, 581-593.

- Crespo, A.J.C., J.M. Domínguez, B.D. Rogers, M. Gómez-Gesteira, S. Longshaw, R.B. Canelas, R. Vacondio, A. Barreiro, and O. García-Feal. "DualSPHysics: Open-source parallel CFD solver based on Smoothed Particle Hydrodynamics (SPH)." Computer Physics Communications 187 (2015): 204-216.

- Canelas, R.B., Aleixo, R., Ferreira, R.M.L. "SPH-based numerical simulation of the velocity field in a dam-break flow." In MEFTE 2012, APMTAC (ed), Lisbon

- Canelas, R.B., R.M.L. Ferreira, A.J.C. Crespo, and J.M. Domínguez. "A generalized SPH-DEM discretization for the modelling of complex multiphasic free surface flows." In the 8th international SPHERIC workshop. 2013.

- Canelas, R.B., Ferreira, R.M.L., Domínguez, J.M. and Crespo, A.J.C. "Modelling Of Wave Impacts On Harbour Structures And Objects With SPH And DEM." In the 9th international SPHERIC workshop. 2014.

- Canelas, R.B., J.M. Domínguez, and R.M.L. Ferreira. "Coupling a Generalized DEM and an SPH Models Under a Heterogeneous Massively Parallel Framework." In CMN 2013, Bilbao, SEMNI (ed) (2013).

- Canelas, R.B., R.M.L. Ferreira, A.J.C. Crespo, and J.M. Domínguez. "Numerical modeling of complex solid-fluid flows with meshless methods." RiverFlow 2014 (2014)

2

Conceptual Models

Contents

This chapter introduces the conceptual models that allow for the description of the fluid and solid phases. Each is described in detail in separate sections and the details concerning their interaction are further elaborated in Section 3.

2.1 Governing Equations for a Fluid Model

Fluid dynamics may be summarized as the attempt to describe motion of a fluid in a given domain, with given forces and boundary conditions. This section encompasses the derivation of the fluid flow equations, that allows to attempt a solution at this problem. They are the continuity equation (Section 2.1.1) and the Navier-Stokes (Section 2.1.2) equations, which are conservation equations for mass and momentum, respectively. They will be derived from a material standpoint, i.e., following a material point in the fluid. Although it represents a relevant misnomer (indicative of history of continuum mechanics as a subject)[1], the material approach is typically called Lagrangian approach, and so it will be treated throughout this work. These equations rely on the continuum hypothesis, i.e., they are the result of averaging the discrete, molecular velocities, positions and densities and treating the flow at a coarse scale, from the molecular standpoint. This allows for a description of the medium as a continuum, were these intensive (or bulk) properties vary smoothly at the scale of the flow.

In a domain, flow equations must be solved considering adequate boundary conditions, that are discussed in Section 2.1.4.

An important tool in deriving equations for continuous media is the Reynolds transport theorem. Consider a material system of particles, Ω, with boundary $\partial\Omega$, moving with velocity $\boldsymbol{u}(\boldsymbol{r})$, where $\boldsymbol{r}$ is a position vector. Consider also a spacial domain Ω_L with boundary $\partial\Omega_L$ [2], convenient for the purpose of expressing conservation equations. For an intensive quantity A, the material derivative of $\int A d\Omega$ is written as

$$\frac{d}{dt}\int_\Omega A(\boldsymbol{r},t)d\Omega = \int_{\Omega_L}\frac{\partial A}{\partial t}d\Omega + \oint_{\partial\Omega_L} A\boldsymbol{u}\cdot\boldsymbol{n}d\Gamma, \tag{2.1}$$

where t is the time, $\boldsymbol{n}$ is the outward normal unit vector of the surface element, $d\Gamma$. Applying Gauss' theorem to the previous expression renders

$$\frac{d}{dt}\int_\Omega A d\Omega = \int_{\Omega_L}\left(\frac{\partial A}{\partial t} + \boldsymbol{\nabla}\cdot(A\boldsymbol{u})\right)d\Omega \tag{2.2}$$

This represents a conservation equation for a given control volume, valid for any quantity A, both scalar and vectorial.

2.1.1 Continuity equation

In the case of mass conservation, by applying $A = \rho$, Equation (2.2) is written as

$$\int_{\Omega_L}\left(\frac{\partial\rho}{\partial t} + \boldsymbol{\nabla}\cdot(\rho\boldsymbol{u})\right)d\Omega = 0, \tag{2.3}$$

since

$$\frac{d}{dt}\int_\Omega \rho d\Omega = \frac{dM}{dt} = 0, \tag{2.4}$$

---

[1] As Truesdell (1954) explains, spatial (Eulerian) and material (Lagrangian) approaches were both considered by Euler before Lagrange. Due to a series of misreports, the material approach is commonly attributed to Lagrange.
[2] Herein referring to control volume and control surface, respectively.

where M is the total mass of Ω, assumed to be conserved in the material system. Expression (2.3) can be written as

$$\frac{\partial \rho}{\partial t} + \boldsymbol{\nabla} \cdot (\rho \boldsymbol{u}) = 0, \tag{2.5}$$

known as the continuity equation of a continuous medium, representing the local conservation of mass. By using the definition of material derivative

$$\frac{dA}{dt} = \frac{\partial A}{\partial t} + \boldsymbol{\nabla} A \cdot \boldsymbol{u}, \tag{2.6}$$

Equation (2.5) can be written as

$$\frac{d\rho}{dt} = -\rho \boldsymbol{\nabla} \cdot \boldsymbol{u} \tag{2.7}$$

2.1.2 Navier-Stokes equation

The Navier-Stokes equations represent momentum conservation. Using $A = \rho \boldsymbol{u}$, Equation (2.2) can be transformed in

$$\frac{d}{dt} \int_{\Omega} \rho \boldsymbol{u} d\Omega = \int_{\Omega_L} \left(\frac{\partial \rho \boldsymbol{u}}{\partial t} + \boldsymbol{\nabla} \cdot (\rho \boldsymbol{u}\boldsymbol{u}) \right) d\Omega \tag{2.8}$$

Applying Newton's second law, we can write

$$\frac{d}{dt} \int_{\Omega} \rho \boldsymbol{u} d\Omega = \boldsymbol{F}_{\Omega}, \tag{2.9}$$

where $\boldsymbol{F}_{\Omega}$ represents a force source term for momentum. Expanding the right side of Equation (2.8) renders

$$\boldsymbol{F}_{\Omega} = \int_{\Omega_L} \left(\boldsymbol{u} \frac{\partial \rho}{\partial t} + \rho \frac{\partial \boldsymbol{u}}{\partial t} + \boldsymbol{u}\boldsymbol{u} \cdot \boldsymbol{\nabla} \rho + \rho \boldsymbol{u} \cdot \boldsymbol{\nabla} \boldsymbol{u} + \rho \boldsymbol{u} \boldsymbol{\nabla} \cdot \boldsymbol{u} \right) d\Omega, \tag{2.10}$$

that can be rearranged into

$$\boldsymbol{F}_{\Omega} = \int_{\Omega_L} \left[\boldsymbol{u} \left(\frac{\partial \rho}{\partial t} + \boldsymbol{u} \cdot \boldsymbol{\nabla} \rho + \rho \boldsymbol{\nabla} \cdot \boldsymbol{u} \right) + \rho \left(\frac{\partial \boldsymbol{u}}{\partial t} + \boldsymbol{u} \cdot \boldsymbol{\nabla} \boldsymbol{u} \right) \right] d\Omega \tag{2.11}$$

Noting that $\boldsymbol{u} \cdot \boldsymbol{\nabla} \rho + \rho \boldsymbol{\nabla} \cdot \boldsymbol{u} = \boldsymbol{\nabla} \cdot (\rho \boldsymbol{u})$ and introducing the continuity equation (2.7), one obtains the non-conservative, integral form of the momentum conservation equation

$$\boldsymbol{F}_{\Omega} = \int_{\Omega_L} \rho \frac{d\boldsymbol{u}}{dt} d\Omega \tag{2.12}$$

For an isolated medium with no external acting forces, total conservation of momentum is then given by $\boldsymbol{F}_{\Omega} = 0$. On a general case $\boldsymbol{F}_{\Omega} \neq 0$, meaning that external forces are applied on a control volume Ω_L. These can be written as

$$\boldsymbol{F}_{\Omega} = \int_{\Omega_L} \boldsymbol{F}_g dm + \oint_{\partial \Omega_L} \boldsymbol{T} d\Gamma, \tag{2.13}$$

where $\boldsymbol{F}_g$ is the gravitational force (or the resultant of any other body forces) per unit mass and $\boldsymbol{T}$ is the contact force, per unit area, on the boundary of Ω_L. Writing the last term as a volume integral by using Gauss' theorem renders

2. Conceptual Models

$$\oint_{\partial\Omega_L} \boldsymbol{T} d\Gamma = \int_{\Omega_L} \boldsymbol{\nabla} \cdot \boldsymbol{\sigma} d\Omega, \tag{2.14}$$

where $\boldsymbol{\sigma} \cdot \boldsymbol{n} = \boldsymbol{T}$. Tensor $\boldsymbol{\sigma}$ is known as the Cauchy stress tensor and is so that $\sigma_{ij} n_j$ is a component of the force being exerted on an surface oriented by $\boldsymbol{n}$, per unit area. Since the integral is over an arbitrary fluid element Ω_L, and writing Equation (2.13) in a local form

$$\frac{d\boldsymbol{u}}{dt} = \frac{1}{\rho} \boldsymbol{\nabla} \cdot \boldsymbol{\sigma} + \boldsymbol{g}, \tag{2.15}$$

where $\boldsymbol{g}$ is the gravitational acceleration vector. The stress tensor can be demonstrated to be symmetrical, Galilean invariant (Aris, 1962) and can also be written as a sum of an isotropic tensor and a deviatoric part

$$\boldsymbol{\sigma} = -p\boldsymbol{I} + \boldsymbol{\tau} \tag{2.16}$$

with

$$p = -\frac{1}{3} \mathrm{tr}(\boldsymbol{\sigma}) \tag{2.17}$$

$\boldsymbol{I}$ is the identity, $\boldsymbol{\tau}$ are deviatoric stresses and the isotropic part is represented by pressure or tensile loads. The separation in isotropic and deviatoric stress tensors is useful for most fluids, since p is an important variable and $\boldsymbol{\tau}$ takes known values in specific conditions, for specific fluids[3]. The momentum conservation equation can now be written as

$$\frac{d\boldsymbol{u}}{dt} = -\frac{1}{\rho} \boldsymbol{\nabla} p + \frac{1}{\rho} \boldsymbol{\nabla} \cdot \boldsymbol{\tau} + \boldsymbol{g}, \tag{2.18}$$

Equation (2.18) is open, since the form of the shear stress tensor is not known. It is written in a general form for any continuous medium, and different media require different constitutive equations for the deviatoric stress.

2.1.3 Newtonian Fluids

Newtonian fluids represent the simplest fluid model that accounts for viscosity, with fluids like clear water and air being very well represented. The formulation stems from Newton's observation that the shear stress seems to be proportional to the strain rate (Batchelor, 2000), i.e.

$$\boldsymbol{\tau} \propto \frac{\partial \boldsymbol{u}}{\partial y}, \tag{2.19}$$

The mechanism by which stress is exerted by one fluid volume against another finds its explanation at the molecular level. An individual molecule in a fluid executes a random motion, result of thermal fluctuations, bouncing against other molecules, which is superposed on the mean drift motion associated with the flow. Normal stress on a given surface arises from average momentum transfer by the fluid molecules executing their random thermal motion, each molecule imparting an impulse as it collides

---
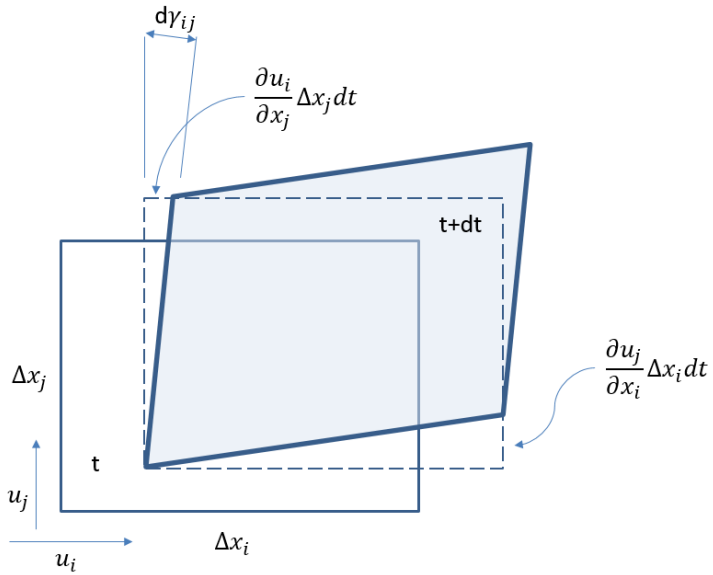
[3]For example, a Newtonian fluid has $\boldsymbol{\tau} = 0$ in hydrostatic conditions, as will be discussed in section 2.1.3.

with the surface and rebounds. Normal stress is exerted even in a static, non-deforming fluid. Generally , shear stress arises when there is a mean velocity gradient in the direction transverse to the flow. Molecules which move by random thermal motion transverse to the flow from a higher mean velocity region toward a lower mean velocity region carry more streamwise momentum than those moving in the opposite direction, and the net transfer of the streamwise molecular momentum manifests itself as a shear stress on the macroscopic level at which we view the fluid.

Three assumptions must be made to derive a form of the shear stresses: i) the shear stress tensor is in fact a linear function of the strain rates; ii) $\boldsymbol{\tau} = 0$ when the rate of shear is zero (as can be observed by measuring a hydrostatic pressure profile in a water column) and iii) the relationship is isotropic (Batchelor, 2000). Figure 2.1 depicts the deformation of a fluid volume as it moves between time t and $t + dt$.

Figure 2.1: Shear deformation in a fluid volume.

In this interval the shear stress τ_{ij} produces in the fluid volume an incremental shear strain, $d\gamma_{ij}$, that can be written in a fixed reference frame as

$$d\gamma_{ij} = \left(\frac{\partial u_i}{\partial x_i} \delta x_i dt \right) / \delta x_i + \left(\frac{\partial u_j}{\partial x_j} \delta x_j dt \right) / \delta x_j \qquad (2.20)$$

In a Lagrangian perspective, the rate of shear strain can be written as

$$\frac{d\gamma_{ij}}{dt} = \frac{\partial u_j}{\partial x_i} + \frac{\partial u_i}{\partial x_j} \qquad (2.21)$$

Imposing assumptions i) and ii), the shear stress is given by

$$\boldsymbol{\tau} = \mu \frac{d\gamma_{ij}}{dt} = \mu \left(\frac{\partial u_i}{\partial x_j} + \frac{\partial u_j}{\partial x_i} \right) = \mu(\boldsymbol{\nabla u} + (\boldsymbol{\nabla u})^T) = 2\mu\boldsymbol{D}; \qquad (i \neq j) \qquad (2.22)$$

where $\boldsymbol{D}$ is the strain rate tensor. Assumption iii) imposes that the coefficient of proportionality μ, the shear viscosity coefficient, is the same for any direction and independent from any kinematic quantities.

2. Conceptual Models

Expression (2.22) is valid in the case of incompressible flow, where Equation (2.7) is reduced to $\nabla \cdot \boldsymbol{u} = 0$ and isotropic stresses are not related to shear stresses. If the flow is compressible however, this relationship takes the form of

$$\boldsymbol{\tau} = \lambda \mathrm{tr}(\boldsymbol{D})\boldsymbol{I} + 2\mu \boldsymbol{D} \tag{2.23}$$

where λ is another proportionality coefficient, called bulk viscosity[4]. The effect on the flow of the term which involves the bulk viscosity is usually very small even in compressible flows (Batchelor, 2000). Only when density changes are induced either over extremely small distances (e.g. in the interior of shock waves, where they occur over a molecular scale) or over very short time scales (e.g. in high-intensity ultrasound) will the term involving $\mathrm{tr}(\boldsymbol{D}) = \nabla \cdot \boldsymbol{u}$ be large enough to have a noticeable effect (Zel'dovich and Raizer, 1967).

Disregarding the terms introduced in Equation (2.23), Equation (2.18) can finally be written as the Navier Stokes equation

$$\frac{d\boldsymbol{u}}{dt} = -\frac{1}{\rho}\nabla p + \frac{1}{\rho}\mu\nabla^2\boldsymbol{u} + \boldsymbol{g} \tag{2.24}$$

2.1.4 Boundary conditions

A particular flow problem may be solved by integrating the Navier-Stokes equation, together with the mass conservation equation plus whatever other equations are required to form a complete set, with the boundary conditions appropriate to the particular problem at hand. Equations (2.7) and (2.24) are applied on a domain Ω, bounded by $\partial\Omega$, composed of solid boundaries $\partial\Omega_B$ and free surfaces $\partial\Omega_F$. A solution yields the velocity components and pressure at the boundaries, from which one obtains the stress tensor via Equations (2.16) and (2.22). In the absence of surface tension, the boundary conditions consistent with the continuum hypothesis are that i) the velocity components and ii) the stress tensor components must be continuous at all points in the domain, including across phase interfaces such as $\partial\Omega_B$ and $\partial\Omega_F$. These conditions can be translated into kinematic and dynamic impositions. The kinematic boundary condition reads

$$\boldsymbol{u}|_{\partial\Omega} = \overline{\boldsymbol{u}}|_{\partial\Omega}, \tag{2.25}$$

where $\overline{\boldsymbol{u}}$ corresponds to an imposed velocity. This condition is inherently verified by the Lagrangian framework. The dynamic boundary condition must express ii), i.e., the continuity of stresses across the interface. Such condition is evident to impose at $\partial\Omega_B$

$$\boldsymbol{\sigma}|_{\partial\Omega_B} = \boldsymbol{\sigma}|_{\partial\Omega}; \quad \forall : \partial\Omega_B \in \partial\Omega \tag{2.26}$$

Equation (2.26) simply interprets (2.14) as a boundary condition. The same can be done in the case of the free-surface, typically imposing a given stress tensor, $\overline{\boldsymbol{\sigma}}$, at each point:

---

[4]For the sake of simplicity, the derivation of Equation (2.23) was not shown. The details can be consulted on Batchelor (2000) and Aris (1962).

$$\boldsymbol{\sigma}|_{\partial\Omega_F} = (-p\boldsymbol{I} + 2\mu\boldsymbol{D})|_{\partial\Omega_F} = \overline{\boldsymbol{\sigma}}|_{\partial\Omega_F} \tag{2.27}$$

After normal projections, one can write

$$p = 2\mu\boldsymbol{n} \cdot \frac{\partial\boldsymbol{u}}{\partial\boldsymbol{n}} \tag{2.28}$$
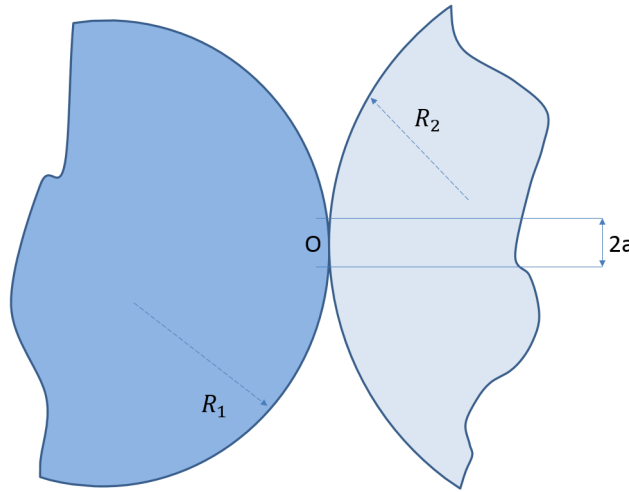
where $\boldsymbol{n}$ is the unit vector normal to the free surface. This relation implies that the pressure field may be discontinuous at the free surface.

$$\boldsymbol{\sigma}|_{\partial\Omega_F} = (-p\boldsymbol{I} + 2\mu\boldsymbol{D})|_{\partial\Omega_F} = \overline{\boldsymbol{\sigma}}|_{\partial\Omega_F}$$

2.2   Contact Mechanics for Fully Elastic Stiff Solids

Contact mechanics considers geometrical and surface effects to deal with material bulk properties. The effects of geometrical effects on local elastic deformations seem to have been first considered by Hertz (1882). The developed theory of Hertzian elastic deformation links the circular contact area of a sphere with a plane or another sphere with the elastic deformation of the materials. The original framework completely disregards any surface interactions. Adhesive interactions were introduced with the Johnson, Kendall and Roberts (JKR) theory (Johnson et al., 1971), using a balance between the stored elastic energy and the loss in surface energy, or interface energy.

By analyzing the stresses at the contact of two elastic solids, small strains within the elastic limit can be assumed. The contact radius a is considered significantly smaller than the radius of curvature R_i of the two contacting surfaces, as depicted in Figure 2.2

Figure 2.2: Contact of two elastic spheres.

Assuming frictionless contact and using an elastic infinite half-space analysis, the contact radius a can be written as

$$a = \left(\frac{3FR^*}{4E^*} \right)^{\frac{1}{3}}$$

(2.29)

where F is the normal applied force, R^* is the generalized radious of curvature of the interaction and E^* is the generalized Young modulus, with

$$R^* = \left(\frac{1}{R_1} + \frac{1}{R_2} \right)^{-1}; \quad E^* = \left(\frac{1 - \nu_{p1}^2}{E_1} + \frac{1 - \nu_{p2}^2}{E_2} \right)^{-1}$$

(2.30)

where ν_p is the Poisson ratio (Johnson, 1987). The force is given by

$$F = \frac{4}{3} E^* \sqrt{R^*} \delta^{3/2}$$

(2.31)

where δ is the depth of indentation, a measure of the deformation of the sphere, given by $\delta = a^2/R^*$. The normal tension distribution (Hertz tension) can be estimated as

$$p(r) = p_0 \left(1 - \frac{r^2}{a^2}\right)^{1/2} \quad ; \quad p_0 = \frac{3F}{2\pi a^2} = \frac{1}{\pi}\left(\frac{6FE^{*2}}{R^{*2}}\right)^{1/3} \tag{2.32}$$

where r is the distance from the contact center.

The application of a tangential load F_t to a Hertzian contact is done by assuming that normal stresses do not cause relative tangential displacements and shear stress do not produce relative normal displacements, i.e., in the absence of a tangential force, contacting points will not undergo tangential displacements (Adams and Nosonovsky, 2000). It is usually assumed that, when F_t is introduced, a central stick region surrounded by two slip zones is present. As the tangential force increases, the size of the stick region decreases and eventually sliding surfaces begins. This sliding respects Coulomb's friction law

$$F_t = \mu_f F_n \tag{2.33}$$

where μ_f is the friction coefficient. This law is general for static and kinetic friction, with a non-constant μ_f value. Conceptual models for the tensions developed prior to sliding are scarce. The traditional model is introduced in Chapter 3, since it is described and assembled in discrete terms.

2. Conceptual Models

3

Numerical Discretization

Contents

In this chapter the discretization methods are introduced and discussed, followed by a proposal for the discretization for the previously presented conceptual models. Competing formulations may be introduced in order to further justify a specific choice or drive a given idea. Continuous interpolation theory is explored, introducing interpolating kernels. Discrete interpolation is described and analyzed, with discrete differential operators being derived. The DEM method is introduced and expanded within the SPH framework. A time integration scheme is introduced and discussed briefly, as well as the corresponding stability region.

3.1 Integral Interpolation and the SPH Method

3.1.1 Introduction

In SPH an approximate numerical solution is obtained by expressing the continuous media by a set of interpolation points from which to compute the quantities being conserved. These points represent material particles, since the Lagrangian description implies that they move with the flow, 'carrying' a given mass. This perspective into the fundamental idea of the method justifies the *particle* term being applied, in the sense of a numerical mass lump, a macroscopic *quanta* of the discretized medium.

The method was introduced by Gingold and Monaghan (1977) and simultaneously by Lucy (1977), initially to solve astrophysical problems where Eulerian mesh-based methods were insufficient. As a purely Lagrangian, meshless scheme, SPH poses a number of advantages over mesh-based methods. Advection is treated explicitly, since particles carry their properties with them. Motion of the media maps directly as motion of the SPH particles. This provides an important advantage for multi-phase problems, as each particle can be assigned to a different phase. Similarly, interfacial or free-surface flows do not require the explicit tracking of the interface or free-surface of interest, as it will be implicitly defined by the positions of the particles. Unlike mesh-based methods, there is no topological connectivity[1] between traditional SPH particles, as they interact with all of the neighbors according to their radial separation, mediated by an interpolating kernel function. This has profound implications, as many of the issues with generation and evolution of a complex, time-varying mesh are bypassed. Problems involving complex, moving geometry, elastic solids or the fracture of brittle solids are significantly simpler to treat using Lagrangian meshless methods.

Disadvantages of the approach include mostly accuracy and stability concerns, due to their difficult formal description. SPH particles are not constrained to stay in a well-ordered, stable configuration. In a regular lattice traditional techniques for stability analysis and convergence studies are well known; in a purely random sampling, as a Monte Carlo method, these qualities are also simple to compute, at least approximately. In SPH however, any lattice deforms, not randomly, but according to the conservation equations being solved, introducing an unexpected difficulty in analyzing the method under normal conditions. If on one hand, by respecting the conservation equations, the particles tend to keep evenly spaced, the instantaneous dynamics of the medium can cause the particles to become locally disordered. Monaghan (2005) presents an analysis of the interpolation errors that occur for

---

[1]Topological connectivity is employed in the context of a numerical discretization exclusively, meaning a fixed list of neighbors with whom to interact does not exist in SPH.

a 1D equi-spaced line of SPH particles. Swegle et al. (1995) and Morris et al. (1997) performed a stability analysis of SPH, providing results for 1D and 2D regular grids of particles. In contrast, there is much less information available on SPH errors and instabilities for disordered particles (Ellero and Adams, 2011). Monaghan (2005) and Dehnen and Aly (2012) calculated an upper bound on the errors due to a randomly distributed set of particles, corresponding to a Monte Carlo simulation. Both noted that the distributions resulting from SPH simulations are significantly more ordered than pure random positions, hence with higher accuracy than traditional Monte Carlo methods, as Quinlan et al. (2006) explored by attempting to actually derive an error estimate for a generic SPH particle distribution. Even if second order seems to be the limit for traditional SPH models (Monaghan, 2005; Oger et al., 2007), satisfactory results are achieved due to their inherent conservation properties, that coupled with the other advantages, seem to provide a uniquely useful tool.

3.1.2 Continuous Interpolation

Consider a scalar field A, expressed as a spatial convolution product with the Dirac Delta function δ

$$A(\boldsymbol{r}) = \int_{\Omega} A(\boldsymbol{r}')\ \delta(\boldsymbol{r} - \boldsymbol{r}')\, dr', \tag{3.1}$$

where Ω denotes the domain corresponding to the continuous medium. The nature of the Dirac Delta function renders (3.1) computationally inadequate, forcing its approximation by a suitable weight function $W(\boldsymbol{r} - \boldsymbol{r}')$, called an interpolation kernel, which is a regular function and defines a compact support region[2]. With Ω' being the domain centered in $\boldsymbol{r}$, one can write

$$A(\boldsymbol{r}) \approx \langle A \rangle(\boldsymbol{r}) = \int_{\Omega'} A(\boldsymbol{r}')\ W(\boldsymbol{r} - \boldsymbol{r}')\, dr', \tag{3.2}$$

with $\langle A \rangle(\boldsymbol{r})$ defining an interpolated field. Expanding field A as a Taylor series around point $\boldsymbol{r}$ and writing $\bar{\boldsymbol{r}} = \boldsymbol{r} - \boldsymbol{r}'$

$$A(\boldsymbol{r}') = A(\boldsymbol{r}) - \frac{\partial A}{\partial \boldsymbol{r}} \cdot \bar{\boldsymbol{r}} + \frac{1}{2} \bar{\boldsymbol{r}}^T \frac{\partial^2 A}{\partial \boldsymbol{r}^T \partial \boldsymbol{r}} \bar{\boldsymbol{r}} + O\left(|\bar{\boldsymbol{r}}|^3\right) \tag{3.3}$$

Replacing (3.3) back to (3.2)

$$\langle A \rangle(\boldsymbol{r}) = A(\boldsymbol{r}) \int_{\Omega_0} W(\bar{\boldsymbol{r}})\, dr' - \frac{\partial A}{\partial \boldsymbol{r}} \cdot \int_{\Omega_0} \bar{\boldsymbol{r}} W(\bar{\boldsymbol{r}})\, dr' +$$
$$+ \frac{1}{2} \text{tr}\left(\frac{\partial^2 A}{\partial \boldsymbol{r}^T \partial \boldsymbol{r}}\right) \cdot \int_{\Omega_0} \bar{\boldsymbol{r}} \times \bar{\boldsymbol{r}} W(\bar{\boldsymbol{r}})\, dr' + \int_{\Omega_0} O\left(|\bar{\boldsymbol{r}}|^3\right) W(\bar{\boldsymbol{r}})\, dr' \tag{3.4}$$

where Ω_0 is Ω' translated to the origin. Noting that in such conditions $dr' = d\bar{r}$, for the approximation $\langle A \rangle \approx A$ to be accurate up to first order, then

$$\int_{\Omega_0} W(\bar{\boldsymbol{r}})\, dr' = 1 \tag{3.5}$$

and

---

[2] A function is said to have compact support if it is zero outside of a compact set. In the context of this work, the compact support region is therefore defined as the $\boldsymbol{r}$ centered region for which the kernel function W is not zero.

3. Numerical Discretization

$$\int_{\Omega_0} W\left(\bar{r}\right)\bar{r}dr' = 0 \tag{3.6}$$

Condition (3.5) implies that the kernel zeroth-order moment should be equal to one, similarly to the Dirac delta distribution. Condition (3.6) asks that the kernel first order moment should be zero. By construction, Ω_0 is centrally symmetric[3] and for an even kernel

$$W\left(-\bar{r}\right) = W\left(\bar{r}\right) \tag{3.7}$$

and

$$\nabla W\left(-\bar{r}\right) = -\nabla W\left(\bar{r}\right) \tag{3.8}$$

Making a variable change $\bar{r}' = -\bar{r}$, one can write condition (3.6) as

$$\int_{\Omega_0} W\left(\bar{r}\right)\bar{r}d\bar{r} = \int_{\Omega_0} W\left(-\bar{r}\right)\bar{r}d\bar{r} = -\int_{\bar{\Omega}_0} W\left(\bar{r}'\right)\bar{r}'d\bar{r}', \tag{3.9}$$

where $\bar{\Omega}_0$ is the symmetric of Ω_0. Assuming symmetrical invariance ($\bar{\Omega}_0 = \Omega_0$), the integral must be equal to its opposite, true only if both integrals are null, rendering condition (3.6) satisfied. We can now reduce (3.4) to

$$\langle A\rangle\left(r\right) = A\left(r\right) + O(h^2), \tag{3.10}$$

where the integral giving the error is $O(h^2)$ because $W\left(\bar{r}'\right)\bar{r}'d\bar{r}' \sim 1/h$.

Applying approximation (3.2) to the field ∇A we may write

$$\langle \nabla A\rangle\left(r\right) = \int_{\Omega'} \frac{\partial A\left(r'\right)}{\partial r'} W\left(\bar{r}\right)dr' =$$
$$= \int_{\Omega'} \frac{\partial}{\partial r'}\left(A\left(r'\right) W\left(\bar{r}\right)\right)dr' - \int_{\Omega'} A\left(r'\right)\frac{\partial W\left(\bar{r}\right)}{\partial r'}dr' \tag{3.11}$$

It is important to write the identity

$$\frac{\partial W\left(\bar{r}\right)}{\partial r'} = -\frac{\partial W\left(\bar{r}\right)}{\partial r} \tag{3.12}$$

Applying the Gauss theorem to the first integral and the identity to the second yields

$$\langle \nabla A\rangle\left(r\right) = \oint_{\partial\Omega'} A\left(r'\right) W\left(\bar{r}\right)n\left(r'\right)d\Gamma + \int_{\Omega'} A\left(r'\right)\frac{\partial W\left(\bar{r}\right)}{\partial r}dr', \tag{3.13}$$

where $n\left(r'\right)$ is the normal unit vector to $\partial\Omega'$. Assuming that the kernel has compact support, the surface integral is reduced to $\partial\Omega \cap \Omega'$ (refer to Figure 3.1). In an infinite domain, or with a sufficiently distant point r from $\partial\Omega$, this boundary integral is zero and Equation (3.13) renders

$$\langle \nabla A\rangle\left(r\right) = \int_{\Omega'} A\left(r'\right) \nabla W\left(\bar{r}\right)dr', \tag{3.14}$$

This defines a continuously interpolated gradient operator, identical to (3.2), but using the kernel gradient as the interpolation function. This is equivalent to writing

---

[3]A centrally symmetric object in Euclidean space is invariant under point reflection through its center.

$$\nabla \langle A \rangle (\boldsymbol{r}) = \langle \nabla A \rangle (\boldsymbol{r}) + O(h^2), \tag{3.15}$$

demonstrated by applying the gradient operator to (3.10). Inserting (3.3) into (3.14) we may write

$$\langle \nabla A \rangle (\boldsymbol{r}) = A(\boldsymbol{r}) \int_{\Omega'} \nabla W(\bar{\boldsymbol{r}}) d\boldsymbol{r}' - \frac{\partial A}{\partial \boldsymbol{r}} \cdot \left(\int_{\Omega'} \nabla W(\bar{\boldsymbol{r}}) \times \bar{\boldsymbol{r}} d\boldsymbol{r}' \right) +$$
$$+ \frac{1}{2} \frac{\partial^2 A}{\partial \boldsymbol{r}^T \partial \boldsymbol{r}} \cdot \left(\int_{\Omega'} \nabla W(\bar{\boldsymbol{r}}) \times \bar{\boldsymbol{r}} \times \bar{\boldsymbol{r}} d\boldsymbol{r}' \right) + O(h^2) \tag{3.16}$$

In order to have second-order accuracy on $\nabla \langle A \rangle (\boldsymbol{r}) \approx \langle \nabla A \rangle (\boldsymbol{r})$ the conditions are
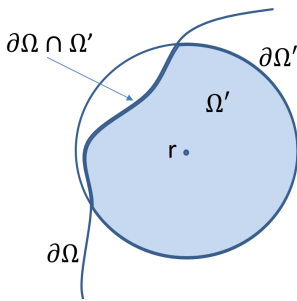
$$\int_{\Omega_0} \nabla W(\bar{\boldsymbol{r}}) d\bar{\boldsymbol{r}} = 0$$
$$\int_{\Omega_0} \nabla W(\bar{\boldsymbol{r}}) \times \bar{\boldsymbol{r}} d\bar{\boldsymbol{r}} = -\boldsymbol{I} \tag{3.17}$$
$$\int_{\Omega_0} \nabla W(\bar{\boldsymbol{r}}) \times \bar{\boldsymbol{r}} \times \bar{\boldsymbol{r}} d\bar{\boldsymbol{r}} = 0$$

where $\boldsymbol{I}$ is the identity. The first and last conditions are inherently satisfied by (3.8). The second condition requires some manipulation:

$$\int_{\Omega_0} \nabla W(\bar{\boldsymbol{r}}) \times \bar{\boldsymbol{r}} d\bar{\boldsymbol{r}} = \int_{\Omega_0} \left[\frac{\partial}{\partial \bar{\boldsymbol{r}}} (W(\bar{\boldsymbol{r}}) \bar{\boldsymbol{r}}) - W(\bar{\boldsymbol{r}}) \left(\frac{\partial \bar{\boldsymbol{r}}}{\partial \bar{\boldsymbol{r}}} \right)^T \right] d\bar{\boldsymbol{r}} =$$
$$= \oint_{\partial \Omega_0} W(\bar{\boldsymbol{r}}) \bar{\boldsymbol{r}} \times \boldsymbol{n}(\bar{\boldsymbol{r}}) d\Gamma - \left(\int_{\Omega_0} W(\bar{\boldsymbol{r}}) d\bar{\boldsymbol{r}} \right) \boldsymbol{I} \tag{3.18}$$

The surface integral is zero in the domain and property (3.5) renders the second condition of (3.17) true.

A note should be made on a crucial assumption on these demonstrations, regarding a typical concern on interpolation methods: the boundaries. Conditions (3.5), (3.6) and (3.17) are true assuming that the compact support kernel $W(\bar{\boldsymbol{r}})$ has no intersection with the boundary of the domain, *i.e.* $\partial \Omega \cap \Omega' = 0$. Figure 3.1 illustrates an intersection of $\partial \Omega$ and Ω'.

Figure 3.1: Compact support kernel and domain boundary.

In this case the kernel zeroth-order momentum would not be one, deviating from the Dirac delta distribution and we would not be able to ensure first order consistency for the kernel approximation. Surface integrals in expressions (3.13) and (3.18) would not disappear, leading to a loss of gradient information near the boundary and also order consistency. These problems meet various mitigation strategies at the discrete level, treated in section 3.1.4.

3. Numerical Discretization

3.1.3 Kernels

In order to ensure the qualities of the continuous interpolation derived in Section 3.1.2, the kernels must define a compact support region and have defined derivatives. A vast body of literature has been dedicated to the subject of kernels, their properties and their performance in the context of an SPH simulation. Apparently similar kernels can produce very different results (Monaghan, 2005; Macià et al., 2011; Violeau, 2012), and it is an ongoing task to formally identify and quantify the characteristics that lead to such differences. For the purpose of this thesis, only two kernels are described, a 5th order class 2 Wendland (Wendland, 1995) and a cubic spline kernel. Both can be written as

$$W(\boldsymbol{r}, h) = \frac{1}{h^d} \tilde{W}(q) \tag{3.19}$$

where h is the smoothing length and defines the scale of the compact support radius for kernel, d is the dimensionality and $q = |\boldsymbol{r}|/h$ is a non-dimensional distance.

For the Wendland kernel, the 5th order class 2 radial interpolation function was reformulated to have a $2h$ radius compact support
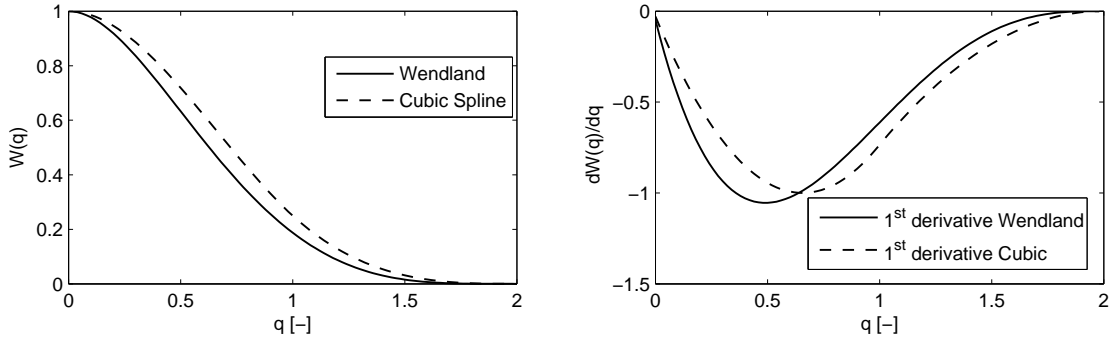
$$\tilde{W}(q) = \alpha_d \begin{cases} (1 - \frac{q}{2})^4 (1 + 2q) & \text{for} \quad 0 \leq q \leq 2 \\ \\ 0 & \text{for} \quad q > 2 \end{cases} \tag{3.20}$$

where α_d takes values $\alpha_2 = 7/4\pi$ and $\alpha_3 = 21/16\pi$.

The cubic spline kernel can be defined as

$$\tilde{W}(q) = \alpha_d \begin{cases} 1 - \frac{3}{2}q^2 + \frac{3}{4}q^3 & \text{for} \quad 0 \leq q \leq 1 \\ \\ \frac{1}{4}(2 - q)^3 & \text{for} \quad 1 \leq q \leq 2 \\ \\ 0 & \text{for} \quad q > 2 \end{cases} \tag{3.21}$$

where $\alpha_2 = 10/7\pi$ and $\alpha_3 = 1/\pi$. Figure 3.2 plots the kernels and respective first derivatives.
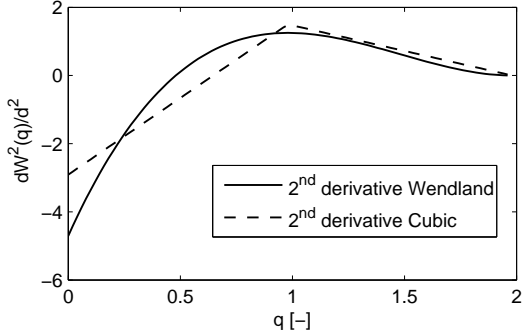
Figure 3.2: Left - Wendland and Cubic spline kernels; Right - First derivatives.

The kernels and the derivatives show very similar profiles, even tough they are one order apart. The cubic spline kernel is however known to cause tensile instability Monaghan and Kos (1999), and requires corrections to definition (3.21). According to Swegle et al. (1995), tensile instability seems

to be directly related to the size of the region of the kernel where the second derivative is negative. Figure 3.3 shows the second derivative of the considered kernels.

Figure 3.3: Second derivative of Wendland and Cubic spline kernels.

As can be noticed the size of these regions is similar, although the shape of the derivatives varies considerably. Macià et al. (2011) performs an analysis of the performance of the Wendland kernel against a Gaussian kernel and finds that, even if apparently similar to the present comparison, the Wendland kernel out-performs other kernels considerably.

3.1.4 Discrete Interpolation

As previously introduced, SPH discretizes a continuous medium as a collection of Lagrangian interpolation nodes with mass. These points are called particles since they coincide with macroscopic material points that bear quantities such as velocity, density and position that change over time. Particle i has a fixed mass of m_i, with volume V_i and density ρ_i related by

$$V_i = \frac{m_i}{\rho_i} \tag{3.22}$$

Assuming a reference density, a diameter Dp can be set to compute the mass and reference volume of the particle.

In a strict Lagrangian framework, quantities of the particle will suffer a variation rate given by its Lagrangian derivative. For example, in the case of position and velocity

$$\dot{\boldsymbol{r}}_i = \boldsymbol{v}_i = \frac{d\boldsymbol{r}_i}{dt} \tag{3.23}$$

Expression (3.23) contrasts with the Eulerian equivalent, since no advection terms are present, greatly simplifying the discretization.
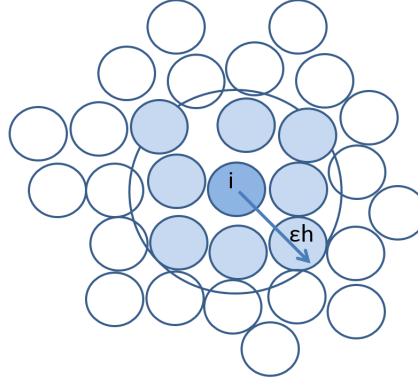
The discretization of operators in SPH is done by approximating the continuous integrals in section 3.1.2 by discrete summations. Employing a Riemann sum, one can write a scalar field as

$$\langle A \rangle \, (\boldsymbol{r}_i) = \int_{\Omega'} A\,(\boldsymbol{r}')\ W\,(\boldsymbol{r}_i - \boldsymbol{r}', h)\, dr' \approx \sum_j A_j V_j W(\boldsymbol{r}_{ij}, h) \tag{3.24}$$

The summation points are particle positions $\boldsymbol{r}_j$, where $A_j = A(\boldsymbol{r}_j)$. $\boldsymbol{r}_{ij}$ represents $\boldsymbol{r}_i - \boldsymbol{r}_j$ and the volume of each j particle accounts for the integration volume dr'. Henceforth, without any loss of

3. Numerical Discretization

richness, the notation will be simplified: the subscripts i and j will tend to identify particles in the summation, $\boldsymbol{r}_{ij}$ will be used and it will be assumed that, dealing with a numerical approximation, the approximation notation will simply be represented by equality. The field is defined by the summation over all particles, but assuming compact support of the kernel this number is rendered finite. The sum is reduced to the particles inside the sphere of radius ϵh, as shown in Figure 3.4

Figure 3.4: Summation extent for interpolation on particle i.

In a 3 dimensions problem, the number of neighbors of a particle can range from a few tens to hundreds of points, summing an important disadvantage SPH presents when compared with traditional, mesh-based methods: large computational cost.

Applying the discrete operator (3.24) to vectorial quantities and notion (3.14) to differential operators we can write

$$
\begin{aligned}
A_i &= \sum_j A_j V_j W(\boldsymbol{r}_{ij}, h) \\
\nabla A_i &= \sum_j A_j V_j \nabla W(\boldsymbol{r}_{ij}, h) \\
\boldsymbol{A}_i &= \sum_j \boldsymbol{A}_j V_j W(\boldsymbol{r}_{ij}, h) \\
\boldsymbol{\nabla} \cdot \boldsymbol{A}_i &= \sum_j V_j \boldsymbol{A}_j \cdot \boldsymbol{\nabla} W(\boldsymbol{r}_{ij}, h)
\end{aligned}
\tag{3.25}
$$

It should be noted that these expressions, although representing an exact derivative of the approximate function (considering no truncation effects on the kernel sampling), are written in a form that leads to a non zero derivative for a constant field. To ensure that gradients respect these properties one can write

$$
\nabla A = \frac{1}{\Phi} \left(\nabla(\Phi A) - A \nabla \Phi \right)
\tag{3.26}
$$

where Φ is a differentiable function. In SPH form

$$
\nabla A_i = \frac{1}{\Phi_i} \sum_j \Phi_j V_j (A_j - A_i) \nabla W(\boldsymbol{r}_{ij}, h)
\tag{3.27}
$$

Equation (3.27) returns a zero gradient for a constant field.

Second derivatives can be estimated by differentiating an SPH interpolant (Equation (3.24)) twice:

$$\nabla^2 A_i = \sum_j A_j V_j \nabla^2 W(\boldsymbol{r}_{ij}, h) \tag{3.28}$$

This expression, however elegant, presents a series of problems: i) it is very sensitive to particle disorder; ii) it is trivial to build a kernel whose second derivative changes sign on its defined region, possibly changing the sign of the second derivative independently of the behavior of the quantity, among other issues, properly explored by Brookshaw (1985); Monaghan (2005). A more useful approach was proposed by Cleary (1996) and Morris et al. (1997)

$$\nabla^2 A_i = \sum_j A_j V_j \frac{\boldsymbol{r}_{ij} \cdot W(\boldsymbol{r}_{ij}, h)}{||\boldsymbol{r}_{ij}||^2} \tag{3.29}$$

This represents a hybrid combination of a finite difference derivative and a SPH derivative. It has the advantage of bypassing the issues raised by taking a direct second derivative of the kernel function, at the expense of not fully conserving angular momentum (Monaghan, 2006).

3.2   Fluid discretization

This Section presents an attempt at discretizing Equations (2.7) and (2.24). With most particulate Lagrangian methods that is to say that the equations will be written with the corresponding discrete operators, in our case, the ones introduced in Section 3.1.4.

The continuity equation (2.7) is traditionally discretized by employing the notion that $\rho \nabla \cdot \boldsymbol{u} = \nabla \cdot (\rho \boldsymbol{u}) - \boldsymbol{u} \cdot \nabla \rho$, rendering equation (2.7) as

$$\frac{d\rho_i}{dt} = \sum_j m_j \boldsymbol{u}_{ij} \cdot \nabla W(\boldsymbol{r}_{ij}, h) \tag{3.30}$$

This is the equivalent of applying operator (3.27) to approximate the $\nabla \cdot \boldsymbol{u}$ field and taking $\Phi = \rho$. Equation (3.30) produces a zero divergence field for a constant $\boldsymbol{u}$ field.

The approach of Sections 3.1.2 and 3.1.4 was consistent with the designing of interpolation operators that would provide a desired accuracy. In particle methods, however, it becomes trivial and very tempting to interpret any equation in terms of pair-wise interaction between particles. For that purpose, we can agree that

$$\nabla W(\boldsymbol{r}_{ij}, h) = \boldsymbol{r}_{ij} F(\boldsymbol{r}_{ij}, h) \tag{3.31}$$

where $F(\boldsymbol{r}_{ij}, h) \leq 0$ is a function that respects Equation (3.31). The contribution of particle j to the density variation of particle i is then

$$m_j \boldsymbol{u}_{ij} \cdot \boldsymbol{r}_{ij} F(\boldsymbol{r}_{ij}, h) \tag{3.32}$$

This implies that approaching ij particles i.e., for $\boldsymbol{u}_{ij} \cdot \boldsymbol{r}_{ij} \leq 0$, the interaction contributes with a positive density change, as our physical intuition expects. Equation (3.30) describes a medium that allows density changes, i.e., it is compressible. By allowing for *some* compressibility the presented discretization is usually called Weakly Compressible Smooth Particle Hydrodynamics (WCSPH). It has become the traditional SPH way of modeling incompressible flows (Monaghan, 2005; Lee et al., 2010). Implementation is trivial since pressure is obtained from a Equation of State (EOS), written so that the speed of sound is large enough to keep the relative density fluctuations small. Lee et al. (2010) gives good insight into the relative accuracy of the pressure field of both WCSPH and an incompressible approach, with the later being superior in most situations. Forcing incompressibility however, demands the solution of a large and potentially sparse Poisson problem at every time-step, built by defining a boundary at the free surface, that needs to be traced accurately. When dealing with highly distorted flows this is a major computational drawback and undermines the Lagrangian nature of the calculation. More details of the WCSPH formulation are discussed in Section 3.2.2.

The pressure gradient of the Navier-Stokes equation ((2.24)) can be discretized in a number of ways. Gingold and Monaghan (1982) and Violeau (2012) used the discrete approximation of the Lagrangian of a particle system, using operators (3.25) and (3.27). The same operators can be used directly to discretize the term in Equation (2.24), leading to

$$\frac{\boldsymbol{\nabla} p_i}{\rho_i} = \sum_j m_j \left(\frac{p_i}{\rho_i^2} + \frac{p_j}{\rho_j^2} \right) \boldsymbol{\nabla} W(\boldsymbol{r}_{ij}, h), \tag{3.33}$$

a symmetrical, balanced form of the pressure term that respects the action reaction principle. This implies that linear and angular momentum are conserved exactly by (3.33). The second term of the second member in Equation (2.24) refers to the shear stresses, and it involves a second derivative of the velocity. As mentioned in Section 3.1.4, applying the SPH operators directly to the second derivative is avoided since it is too sensitive to particle disorder and limits the choice of the kernel functions.

Three approaches to modeling this term are presented: the artificial viscosity model introduced by Gingold and Monaghan (1982), the laminar viscosity model by introduced by Morris et al. (1997) and the Sub-Particle Stress (SPS) terms, properly presented in Dalrymple and Rogers (2006) and discussed in Section 3.2.1.

Gingold and Monaghan (1982) introduced a momentum dissipating term in the form of a viscosity, designed to treat shock-tube problems. This form of numerical viscosity also mitigates problems due to instabilities arising in the system coming from the unstructured behavior of the particles, as well as accumulation of acoustic energy from integration errors during a simulation without dissipation. It is written as

$$\boldsymbol{\Pi}_i = \sum_j \begin{cases} \dfrac{-\alpha \bar{c}_{ij} \mu_{ij}}{\rho_{ij}} \boldsymbol{\nabla} W(\boldsymbol{r}_{ij}, h) & \text{if } \boldsymbol{u}_{ij} \cdot \boldsymbol{r}_{ij} < 0 \\ \\ 0 & \text{if } \boldsymbol{u}_{ij} \cdot \boldsymbol{r}_{ij} \geqslant 0 \end{cases} \quad \text{with} \quad \mu_{ij} = \frac{(\boldsymbol{u}_{ij} \cdot \boldsymbol{r}_{ij} h)}{r_{ij}^2}, \tag{3.34}$$

where c is the sound celerity and α is a parameter subject to calibration. This expression is traditionally used due to its simple implementation, conservation of linear and angular momentum and because it converges to $\mu \boldsymbol{\nabla}^2 \boldsymbol{u}$ as $h \to 0$ (Issa, 2004). It is however considered dissipative regarding shear and vorticity, and the case-dependent α parameter confirms its empirical nature.

Morris et al. (1997), influenced by the work of Cleary (1996), proposed to model the shear viscosity by

$$\boldsymbol{\Pi}_i = \sum_j m_j \left(\frac{4\nu \boldsymbol{r}_{ij} \cdot \boldsymbol{\nabla} W(\boldsymbol{r}_{ij}, h)}{(\rho_i + \rho_j) r_{ij}^2} \right) \boldsymbol{u}_{ij} \tag{3.35}$$

where ν is the actual kinematic viscosity of the fluid, defined as $\nu = \mu/\rho$. This expression conserves linear momentum but not angular momentum (Colagrossi et al., 2011). Recent ideas over the local consistency of Expression (3.35), particularly in when the kernel is truncated, have been discussed by Colagrossi et al. (2011) and Gonzàlez et al. (2009).

The momentum equation ((2.24)) can now be written as

$$\frac{d\boldsymbol{u}_i}{dt} = -\sum_j m_j \left(\frac{p_i}{\rho_i^2} + \frac{p_j}{\rho_j^2} \right) \boldsymbol{\nabla} W(\boldsymbol{r}_{ij}, h) + \boldsymbol{\Pi}_i + \boldsymbol{g} \tag{3.36}$$

3.2.1 Turbulence modeling

Expressions (3.34) and (3.35) attempt to account for shear stresses developed at the scale of the interparticle interactions, h. Turbulent fluid flow however, may present very small local scales, depending on the Reynolds number, R_e (Batchelor, 2000; Pope, 2000). Attempting to model all of these

3. Numerical Discretization

scales is designated by Direct Numerical Simulation (DNS), where no turbulent closures are needed. This imposes a serious limit on the range of possible R_e, since computational resources are limited. Opposite to this, the Reynolds-averaged Navier-Stokes Equations (RANS) rely on closure models to estimate the stresses that arise even from large, energy-carrying structures. Another approach naturally compatible with our framework is to use Large Eddy Simulation (LES) techniques, that can be understood as a intermediate between DNS and RANS. The idea is that the governing equations are spatially averaged over a length scale of the order of the numerical discretization. The contribution of the large structures to momentum and energy transfer is computed directly and only the effects of the smallest scales of turbulence are modeled. The hope is that, since the small scales tend to be more homogeneous and universal (Pope, 2000), the models can be simpler and require fewer adjustments when applied to different flows than similar models for the RANS.

To obtain the motion equations of the resolved scales, large and small scales must be separated. LES is based on the definition of a filtering operation: a resolved variable is defined as

$$\langle A \rangle \left(\boldsymbol{r} \right) = \int_\Omega A(\boldsymbol{r}')G\left(\boldsymbol{r}, \boldsymbol{r}'; \langle \Delta \rangle \right) d\boldsymbol{r}', \qquad (3.37)$$

where G is the filter function, the $\langle \ \rangle$ operator represents a generic spatial averaging and $\langle \Delta \rangle$ is the filter-width associated with the wavelength of the smallest scale retained by the filtering operation. Thus, the filter function determines the size and structure of the small scales. A special note should be given regarding the idea of the integral interpolant behind SPH (Equation (3.1)) and the filtering operation of LES. Since both SPH and LES share the same mathematical structure, it should come as no surprise that the combination of the methods seems very atractive to modelers.

Gotoh et al. (2001) introduced this type of subgrid scaling for their incompressible Moving Particle Simulation (MPS) method, as did Lo and Shao (2002) for their incompressible SPH method. For a compressible fluid, sub-particle scaling requires the use of special averaging, with Favre-averaging being the typically chosen in the literature. It is written as

$$\langle A \rangle = \frac{\langle \rho A \rangle}{\langle \rho \rangle} \qquad (3.38)$$

By using Favre-averaging, no new terms are introduced in the conservation equations, except for the SPS terms. This means that Equations (3.30) and (3.36) are implicitly in their filtered form, assuming $\langle A \rangle = A^4$. For the momentum Navier-Stokes equation, the application of a flat-top spatial filter yields (Yoshizawa, 1986)

$$\frac{d \langle \boldsymbol{u} \rangle}{dt} = -\frac{1}{\langle \rho \rangle} \boldsymbol{\nabla} \langle p \rangle + \frac{1}{\langle \rho \rangle} \mu \boldsymbol{\nabla}^2 \langle \boldsymbol{u} \rangle + \frac{1}{\langle \rho \rangle} \boldsymbol{\nabla} \cdot \boldsymbol{\tau}^* + \boldsymbol{g}, \qquad (3.39)$$

where $\boldsymbol{\tau}^*$ is the SPS tensor. Several proposals exist for the form of the tensor. Eddy-viscosity models try to reproduce the global exchange of energy between the resolved and unresolved stresses by mimicking the drain of energy associated with the turbulence energy cascade (Batchelor, 2000). Yoshizawa (1986) proposed an eddy-viscosity model for weakly compressible turbulent flows using a multiscale

---

[4]An acceptable abuse of notation since the averaged scale is indeed our working scale, no ambiguity is introduced.

direct-interaction approximation method. The anisotropic part of the SPS is parametrized using the Smagorinsky (1963) model, while the SPS energy is modeled by a separate term

$$\frac{\boldsymbol{\tau}^*}{\langle\rho\rangle} = 2\nu_t\left(\langle\boldsymbol{D}\rangle - \frac{1}{3}\boldsymbol{\delta}\mathrm{tr}\left(\langle\boldsymbol{D}\rangle\right)\right) - \frac{2}{3}C_I\Delta^2\boldsymbol{\delta}|\langle\boldsymbol{D}\rangle|^2, \tag{3.40}$$

where $\nu_t = (C_S\Delta)^2|\langle\boldsymbol{D}\rangle|$ is the eddy viscosity, $C_S = 0.1677$ is the Smagorinsky constant, $C_I = 6.6\times10^{-3}$ and $|\langle\boldsymbol{D}\rangle| = (2\langle\boldsymbol{D}\rangle\langle\boldsymbol{D}\rangle)^{1/2}$ (Martin et al., 2000).

In SPH notation, the SPS term receives the same treatment as the pressure gradient term, in Equation (3.33):

$$\boldsymbol{\Pi}_i^{SPS} = \sum_j m_j\left(\frac{\boldsymbol{\tau}_i^*}{\rho_i^2} + \frac{\boldsymbol{\tau}_j^*}{\rho_j^2}\right)\cdot\boldsymbol{\nabla}W(\boldsymbol{r}_{ij}, h), \tag{3.41}$$

where strain rate tensor is computed directly by approximating the velocity gradients with operator (3.27) ($\Phi = \rho$). The Δ filter-width is typically taken as the distance between particles.

3.2.2 Density and pressure fields

The WCSPH formulation introduced by Equation (3.30) demands the usage of an EOS to link the pressure and density fields. The most commonly employed EOS is called Tait's Equation (Batchelor, 2000), and is usually used to describe barotropic fluids:

$$p_i = \frac{\rho_0 C_s^2}{\gamma}\left[\left(\frac{\rho_i}{\rho_0}\right)^\gamma - 1\right] \tag{3.42}$$

where ρ_0 is a reference density, C_s is the numerical sound celerity and $\gamma = 7$ for a fluid like water. It is used for free-surface flow because it assumes negligible atmospheric, or background, pressure. $C_s = \sqrt{\partial p/\partial\rho}|_{\rho_0}$ (Batchelor, 2000) can be chosen large enough to render relative density fluctuations small, i.e., since

$$\frac{|\delta\rho_i|}{\rho_i} \sim \frac{u_i^2}{C_s^2} \tag{3.43}$$

C_s can be chosen as any percentage of the maximum velocity in the flow to ensure that the maximum density fluctuation is one order of magnitude lower. Typically C_s is taken as $10\max u_i$, guaranteeing that $\max(|\delta\rho_i|/\rho_i) \sim 0.01$. By using the first term of a Taylor expansion of Equation (3.43), a linearized EOS can be written as

$$p_i = C_s^2(\rho_i - \rho_0) \tag{3.44}$$

This is built assuming locally smooth density gradients, and is usually used in the absence of a free-surface.

Equation (3.42) represents a very stiff density field, and together with the natural disordering of the Lagrangian particles, high-frequency low amplitude oscillations are found to populate the density scalar field (Molteni and Colagrossi, 2009). The explored strategy in this work is to use a diffusive term in the continuity equation, now written as

3. Numerical Discretization

$$\frac{d\rho_i}{dt} = \sum_j m_j \boldsymbol{u}_{ij} \cdot \boldsymbol{\nabla} W(\boldsymbol{r}_{ij}, h) + \Phi_i \qquad (3.45)$$

where
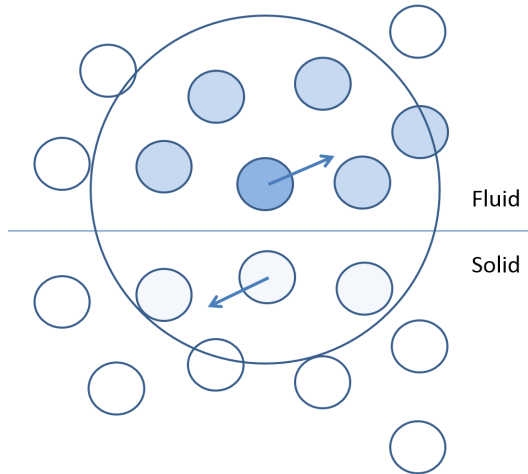
$$\Phi_i = 2\delta_\Phi h C_s \sum_j (\rho_j - \rho_i) \frac{\boldsymbol{r}_{ij} \cdot \boldsymbol{\nabla} W(\boldsymbol{r}_{ij}, h)}{r_{ij}^2} \frac{m_j}{\rho_j}, \qquad (3.46)$$

This represents the original δ-SPH formulation by Molteni and Colagrossi (2009), due to the free parameter δ_Φ, that needs to be attributed a suitable value. It can be explained simply as the addition of the Laplacian of the density field to the continuity equation. Antuono et al. (2012) has presented a careful analysis of the influence of this term in the system, by decomposing the Laplacian operator, observing the converge of the operators and performing linear stability analysis to inspect the influence of the δ_Φ diffusive coefficient. Equation (3.46) represents exactly a diffusive term in the domain bulk. The behavior changes close to open boundaries such as free-surface. Due to truncation of the kernel (there are no particles being sampled outside of an open boundary), the first order contributions of (3.46) are not null (Antuono et al., 2010), resulting in a net force applied to the particles. This effect is not considered relevant for non-hydrostatic situations, where this force is many orders of magnitude inferior to any other force involved. Corrections to this effect were proposed by Antuono et al. (2010), but involve the solution of a renormalization problem for the density gradient, with considerable computational cost.

3.2.3 Boundary Conditions

Boundary conditions must respect the ideas developed in Section 2.1.4, particularly, that continuity of stresses across any interface must be respected. Another apparent advantage of particulate methods is that the condition is inherently satisfied since particles will respect Equations (2.7) and (2.24) via their discrete forms, Equations (3.30) and (3.36). In SPH however, the kernel is truncated near the boundaries and the imposition of a correct stress field at solid interfaces is demanding. The typical attempt at a solution is to complete the kernel on these regions, by introducing a series of boundary particles that may respect a different set of equations. Four major approaches are used for this effect: i)ghost particles, ii)repulsive particles, iii)dynamic particles and iv)boundary integrals.
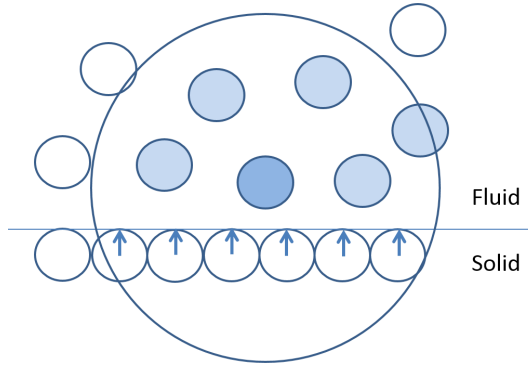
Ghost particles were initially devised by Randles and Libersky (1996) in order to respect a no-slip condition at the same time that the kernel is not truncated. If a fluid particle is close to a solid boundary, for $(r_{ij} < h)$, a new particle is generated as the specular image of the incident one, as the scheme in Figure 3.5.

Figure 3.5: Scheme of ghost particles boundary condition.

Both particles have the same density, but opposite normal and tangential velocities. Two disadvantages arise with this approach: complex geometries are extremely difficult to model (sharp angles, thin plates, hollow boxes) and the number of particles in the system may vary at each time step, a further implementation complication, explored in Section 4.
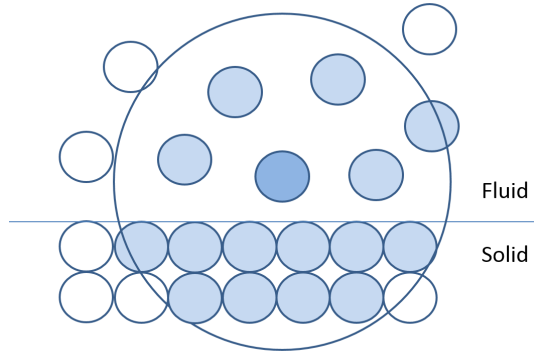
Repulsive particles (Monaghan and Kos, 1999) represent stationary particles that do not respect the conservation equations, but instead apply *ad-hoc* forces to approaching fluid particles. The forces may be based on Lennard-Jones potentials, and a series of interpolation procedures are carried out to assure the continuity of a force field perceived by a fluid particle moving in an arbitrary direction from the boundary, as represented in Figure 3.6.

Figure 3.6: Scheme of repulsive particles boundary condition.

Dynamic particles were introduced by Dalrymple and Knio (2000) and further studied by Crespo et al. (2007), that devised them as fluid particles with an externally imposed motion. The particles respect Equations (3.30) and (3.36) but their position is not given by integrating the velocity in time. A static boundary will have zero velocity (traditional arrangement in Figure 3.7) and a moving boundary will have a prescribed motion.

3. Numerical Discretization

Figure 3.7: Scheme of dynamic particles boundary condition.

A known difficulty of this formulation is the overestimation of the density (Price, 2008; Saitoh and Makino, 2013), resulting from an entropy jump across the fluid/solid interface. This results in an increased distance of fluid-solid particles due to the added force from the pressure gradient, effectively disturbing the viscous forces computed at that interface (Colagrossi and Landrini, 2003).

Boundary integral ideas are being explored in order to complete the kernel around boundaries, namely, analytically summing the missing terms. The boundary integral conditions (Ferrand et al., 2013; Mayrhofer et al., 2015) are promising but still face many challenges related to complex geometries and efficient implementations.

This work will employ dynamic boundary conditions throughout, due to the simplicity and potential of the implementation. The solid body discretization presented in Section 3.3 will also use the same framework.

3.3   Solid discretization: combining SPH and DEM

The purpose of this Section is to devise a framework where the dynamics of solid bodies of arbitrary shape can be discretized in a way that solid-fluid interactions become trivial in the context of the fluid discretization presented in Section 3.2. Section 3.3.1 presents that general framework, where discrete equations for rigid body dynamics are introduced, generalizing the source of accelerations affecting a body.

The DEM model is introduced in Section 3.3.2, where the particular case of solid-solid interaction is explored. Traditional DEM models are analyzed, as well as their numerical properties.

The result of this section is a DCDEM, fully respecting the requirements of an accurate and robust model for the treatment of solid bodies with 6 Degrees of Freedom (DOF) in a multiphase setting.

3.3.1   Rigid body discretization

In the domain frame reference, the equations for a rigid body I can be written as

$$M_I \frac{d\boldsymbol{V}_I}{dt} = \sum_i \boldsymbol{F_i} \tag{3.47}$$

$$\boldsymbol{I}_I \frac{d\boldsymbol{\Omega}_I}{dt} = \sum_i (\boldsymbol{r}_i - \boldsymbol{R}_I) \times \boldsymbol{F_i}, \tag{3.48}$$

where body I possesses a mass M_I, velocity $\boldsymbol{V}_I$, inertial tensor $\boldsymbol{I}_I$, angular velocity $\boldsymbol{\Omega}_I$ and center of gravity $\boldsymbol{R}_I$, and is subjected to an arbitrary number of forces $\boldsymbol{F_i}$, applied at points $\boldsymbol{r_i}$.

In a particulate method it is trivial to idealize sub sets of particles in the domain whose variables are integrated in time with a different set of equations. If one uses Newton's equations for rigid body dynamics, then, that system of particles represents a rigid body. If body I is a collection of particles[5], then the right side of Equations (3.47) and (3.48) can easily be discretized by

$$M_I \frac{d\boldsymbol{V}_I}{dt} = \sum_{k \in I} m_k \frac{d\boldsymbol{u}_k}{dt} \tag{3.49}$$

$$\boldsymbol{I}_I \frac{d\boldsymbol{\Omega}_I}{dt} = \sum_{k \in I} m_k (\boldsymbol{r}_k - \boldsymbol{R}_I) \times \frac{d\boldsymbol{v}_k}{dt} \tag{3.50}$$

$m_k d\boldsymbol{u}_k/dt$ represents the force by unit mass applied to particle k, belonging to body I. This force encompasses body forces (gravity), fluid resultants as well as the result of any rigid contact that might occur. This is inline with the work of Koshizuka et al. (1998), that first applied this idea in the context of MPS.

Expressions (3.49) and (3.50) are obtained directly from applying (3.47) and (3.48) to a system of particles, i.e., they inherently conserve linear and angular momentum, as they are simple conservation laws. This is an advantage of particulate Lagrangian discretizations, since they are an exact representation of particle systems if the closure terms are also exact. For this system, it is simple to write the center of mass $\boldsymbol{R}_I$ and inertia tensor $\boldsymbol{I}_I$

---

[5]In this section I is used for both the index of the rigid body in question and as the set of indexes from the particles that constitute the body. The abuse of notation is employed since in this context, they are semantically coincident.

3. Numerical Discretization

$$R_I = \frac{1}{n_I} \sum_{k \in I} R_k; \qquad I_I = \sum_{k \in I} = m_k [r_k - R_I][r_k - R_I] \tag{3.51}$$

where n_I is them number of particles that constitute body I, $[r_k - R_I]$ is the skew-symmetric matrix built from $r_k - R_I$. Keeping in the domain frame reference implies that these quantities need to be recomputed whenever the system suffers an acceleration.

Forces resulting from solid-fluid interaction are computed with Equation (3.36), where the viscous formulation provides a viscous drag closure. No *ad-hoc* terms are added, since all the dynamics are a result of the fundamental, particle-wise, solution of Equations (3.49) and (3.50).

This formulation can be seen as an extension of the dynamic boundary conditions introduced in Section 3.2.3. As such, it suffers from the same overestimation of the density across the fluid/solid interface Price (2008); Saitoh and Makino (2013), resulting from an entropy jump. The inclusion of the δ-SPH diffusive term in Equation (3.45) allows for an apparently correct density estimation across the interface, as explored in the Results Section. The particles belonging to body I are then moved according to

$$u_k = V_I + \Omega_I \times (r_k - R_I), \tag{3.52}$$

i.e., the velocity given by propagating the rigid body velocities.

3.3.2 Force discretization: the DEM model

Forces $m_k d u_k/dt$ will rise whenever a particle interacts with another. In the particular case of a solid-solid collision, the contact force is decomposed into F_n and F_t, normal and tangential components respectively. Both of these forces will take forms explored in Section 2.2, with the addition of viscous dissipation effects. This is because two colliding bodies undergo a deformation which will be somewhere between perfectly inelastic and perfectly elastic, usually quantified by the normal restitution coefficient

$$e_n = -\frac{v_n|_{t=t^n}}{v_n|_{t=0}}, \quad e \in [0, 1] \tag{3.53}$$
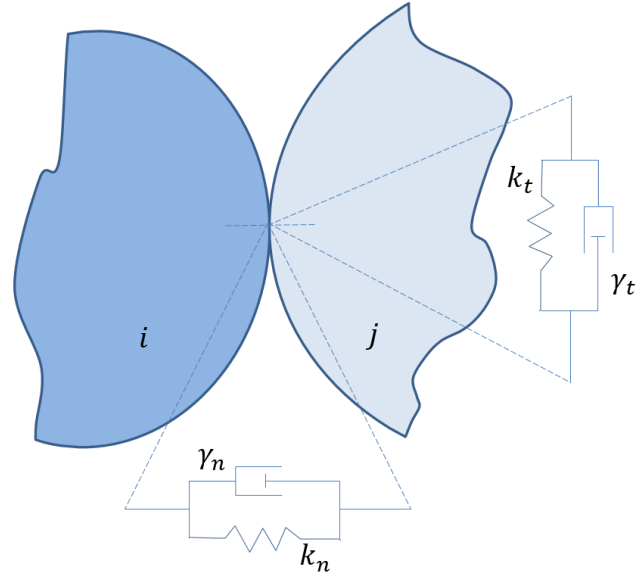
where $t = t^n$ is the instant at the end of collision and $t = 0$ is the instant immediately before.

Forces are further decomposed into a repulsion force, F^r, arising from the elastic deformation of the material, and a damping force, F^d, for the viscous dissipation of energy during the deformation. Other dissipative mechanisms, such as plastic deformation and emission of elastic waves, excited from impact, will not be considered. The elastic waves are always present, but carry very little energy (Shäfer et al., 1996), and are usually disregarded. Plastic deformation is not considered directly as its effects can, to some extent, be included in the viscous dissipation terms.

Figure 3.8 generally illustrates the proposed viscoelastic DEM mechanism between two interacting particles.

Every interaction is conceptualized as a system of springs and dampers. A general expression for the normal force in such viscoelastic model will be

Figure 3.8: Scheme of DEM mechanism.

$$\boldsymbol{F}_{n,ij} = \boldsymbol{F}_n^r + \boldsymbol{F}_n^d = k_{n,ij}\delta_{ij}^{p_1}\boldsymbol{e}_{ij} - \gamma_{n,ij}\delta_{ij}^{p_2}\dot{\delta}_{ij}\boldsymbol{e}_{ij}, \tag{3.54}$$

where $k_{n,ij}$ is the normal stiffness constant of pair ij, $\delta_{ij} = \max(0, (d_i + d_j)/2 - |\boldsymbol{r_{ij}}|)$ is the particle overlap, $\boldsymbol{e}_{ij}$ is the unit vector between the two mass centers and $\gamma_{n,ij}$ is the normal damping constant. For $p_1 = p_2 = 1$, the mechanism is linear, corresponding to a simple damped harmonic resonator. An analytical solution (Shäfer et al., 1996) shows that this leads to a constant normal restitution coefficient, independent of the impact velocity

$$e_{n,ij} = \exp\left(-\frac{\gamma_{n,ij}}{2M^*}t_{c,ij}\right) \tag{3.55}$$

where $M^* = m_i m_j/(m_i + m_j)$ and $t_{c,ij}$ is the contact duration, given by

$$t_{c,ij} = \pi\left(\frac{k_{n,ij}}{M^*} - \left(\frac{\gamma_{n,ij}}{2M^*}\right)^2\right)^{-1/2} \tag{3.56}$$

Experimental studies using pendulum devices indicate that the e_n and t_c should depend on impact velocity however. Figures 3.9 and 3.10 both compiled by Kruggel-Emden et al. (2007), show that dramatic variations of these quantities may be registered.
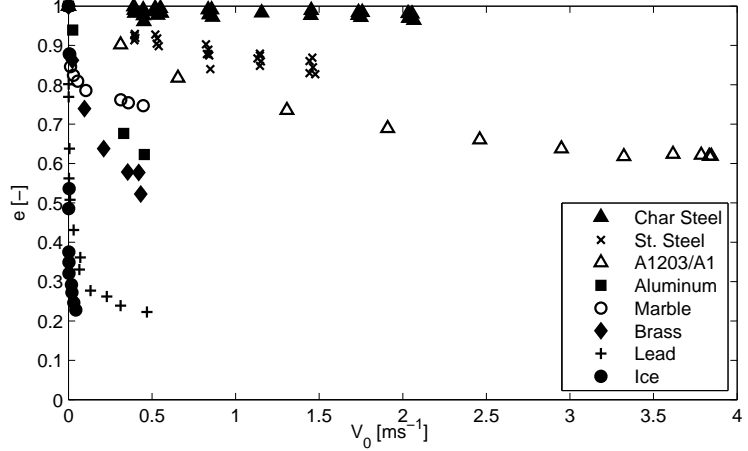
Non-linear models allow to overcome the limitation imposed by a constant restitution coefficient and contact duration. Kuwabara and Kono (1987), Brilliantov et al. (1996) and Brilliantov and Pöschel (2001) proposed a fully non-linear model that reads

$$\boldsymbol{F}_{n,ij} = \boldsymbol{F}_n^r + \boldsymbol{F}_n^d = k_{n,ij}\delta_{ij}^{3/2}\boldsymbol{e}_{ij} - \gamma_{n,ij}\delta_{ij}^{1/2}\dot{\delta}_{ij}\boldsymbol{e}_{ij}, \tag{3.57}$$
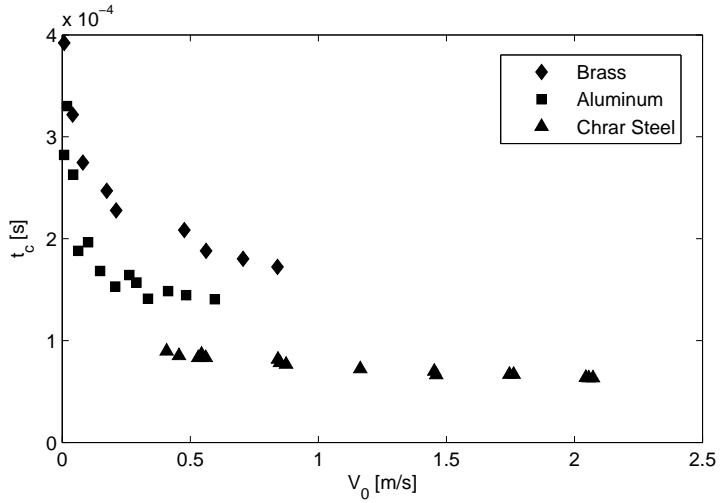
The stiffness, recovering the elastic Hertz model from Section 2.2, is given by a form of Equation (2.31)

$$k_{n,ij} = \frac{4}{3}E^*\sqrt{R^*} \tag{3.58}$$

3. Numerical Discretization

Figure 3.9: Restitution coefficient e as a function of initial normal velocity V_0 (Kruggel-Emden et al., 2007).

Figure 3.10: Duration of contact t_c as a function of the impact normal velocity V_0 (Kruggel-Emden et al., 2007).

Considereing exclusivelly the repulsive part of Equation (3.57), Shäfer et al. (1996) notes that $t_{c,ij}$ is no longer independent from the normal velocity impact $v_{n,ij}$

$$t_{c,ij} = 3.21 \left(-\frac{M^*}{k_{n,ij}} \right)^{2/5} v_{n,ij}^{-1/5} \tag{3.59}$$

implying that there is no longer an intrinsic time scale to collisions, as expected from experimental data.
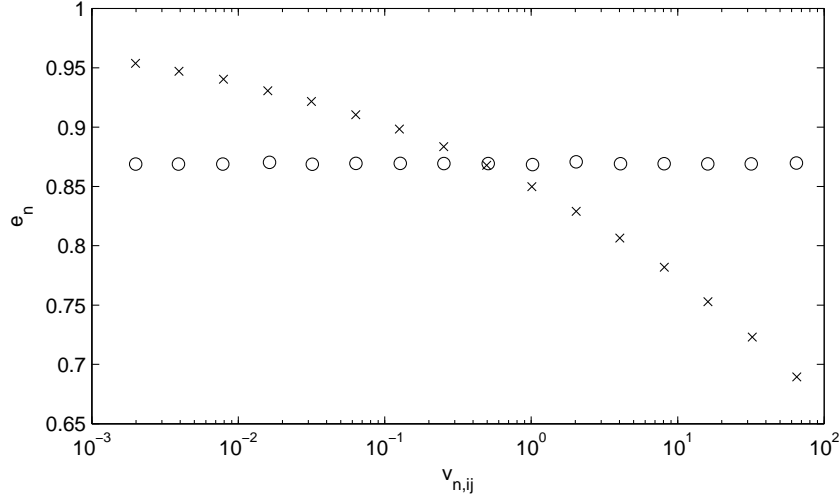
Brilliantov et al. (1996) and Brilliantov and Pöschel (2001) proposed that the viscous damper coefficient $\gamma_{n,ij}$ is a material property, obtainable from the bulk viscosities of the materials in collision and the local curvature at impact point. However, very little studies have been devoted to bulk viscosities and as a consequence $\gamma_{n,ij}$ is traditionally treated as a calibration parameter. Cummins and Cleary (2011) writes an expression for $\gamma_{n,ij}$ depending exclusively on a normal restitution coefficient

$$\gamma_{n,ij} = -\frac{\log e_{n,ij}}{\sqrt{\pi^2 + \log^2 e_{n,ij}}} \tag{3.60}$$

Expression (3.60) used in the context of a non-linear model, is ambiguous. In practice, a constant value for $e_{n,ij}$ will be used to compute $\gamma_{n,ij}$, that will lead to a non-constant, effective $e_{n,ij}$, depending on the impact velocity.

Figure 3.11 shows $e_{n,ij}$ as a function of $v_{n,ij}$, for the linear model and for the non-linear Hertz model (Expression (3.57))

Figure 3.11: Normal restitution coefficient $e_{n,ij}$ as a function of the impact normal velocity $v_{n,ij}$. Linear force ($\circ$), Non-linear Hertz ($\times$)

For the linear case $k_n = 7.32 \times 10^6 \text{ Nm}^{-1}$ and $\gamma_n = 2.06 \text{ kg s}^{-1}$, resulting in $e_n = 0.87$. For the non-linear model, $\gamma_n = 190 \text{ m}^{-1/2}\text{s}^{-1}$, in order to produce comparable e_n in the selected $v_{n,ij}$ range. As expected, the linear model produces a constant e_n. Force (3.57) leads to an inversely proportional $e_{n,ij}$ with $v_{n,ij}$, i.e., $(1 - e_{n,ij}) \sim v_{n,ij}^{1/5}$, in agreement with experimental results (Figure 3.9).

Regarding tangential contacts, friction is modeled using the same model, as indicated in Figure 3.8. The mechanism can be reproduced by a linear dash-pot

$$\boldsymbol{F}_{t,ij} = \boldsymbol{F}_t^r + \boldsymbol{F}_t^d = k_{t,ij}\delta_{ij}^t \boldsymbol{e}_{ij}^t - \gamma_{t,ij}\dot{\delta}_{ij}^t \boldsymbol{e}_{ij}^t \tag{3.61}$$

where the stiffness and damping constants are derived to be

$$k_{t,ij} = 2/7 k_{n,ij}; \quad \gamma_{t,ij} = 2/7 \gamma_{n,ij}, \tag{3.62}$$

as to insure internal consistency of the time scales required for stability (Hoomans, 2000). This mechanism models the static and dynamic friction mechanisms by a penalty method. The body does not statically stick at the point of contact, but is constrained by the spring-damper system. This force must be bounded above by the Coulomb friction law introduced by Equation (2.33). The Coulomb law is modified with a sigmoidal function in order to make it continuous around the origin regarding the tangential velocity (Vetsch, 2011):

$$\boldsymbol{F}_{t,ij} = \min(\mu_{fIJ}\boldsymbol{F}_{n,ij}\tanh(8\dot{\delta}_{ij}^t)\boldsymbol{e}_{ij}^t; \quad \boldsymbol{F}_{t,ij}), \tag{3.63}$$

where μ_{fIJ} is the friction coefficient at the contact of I and J and is simply taken as the average of the two friction coefficients of the distinct materials.

3.4   Time Integration and Stability Region

The ordinary differential equations described in Sections 3.2 and 3.3 may be integrated in time using a stable method. Traditionally Symplectic schemes are preferred in Hamiltonian systems due to the time-reversibility in the absence of dissipative terms, as well as implicit conservation properties (Monaghan, 2005), leading to a lesser energy drift in long computations. Both SPH and DEM methods use the Symplectic scheme due to these characteristics. An explicit second-order with time accuracy of $O(dt^2)$ Symplectic integrator is used, using two half-steps with a predictor-corrector strategy:

$$Q_i^{n+1/2} = Q_i^n + \frac{1}{2}\Delta t \frac{dQ_i^n}{dt} \tag{3.64}$$

where Q takes the form of ρ, $\boldsymbol{r}$ or $\boldsymbol{u}$, to integrate for density, position and velocity, respectively. For the corrector step

$$Q_i^{n+1} = Q_i^{n+1/2} + \frac{1}{2}\Delta t \frac{dQ_i^{n+1/2}}{dt} \tag{3.65}$$

where the corrected velocity $\boldsymbol{u}_i^{n+1}$ is used to update the corrected position $\boldsymbol{r}_i^{n+1}$ and both are used to compute the corrected density ρ_i^{n+1}.

The stability region of numerical schemes is traditionally assessed with a Courant-Friedrichs-Lewy (CFL) condition. This condition relates the length of the time step to a function of the spatial discretization and the maximum speed with which information can travel in the physical space. In the WCSPH scheme, this translates to

$$\Delta t_1 = C \min_i \left(\frac{h}{C_s} \right) \tag{3.66}$$

where C is the CFL parameter. For traditional explicit schemes $C \in [0;1]$. Monaghan (1989) recognized the diffusive nature of the artificial viscosity formulation (Equation 3.34) and added the diffusive signal to the velocity signal, resulting in

$$\Delta t_1 = C \min_i \left(\frac{h}{C_s + \max_j |\mu_{ij}|} \right) \tag{3.67}$$

Another CFL criterion can be derived by using particle accelerations (Monaghan, 1992), ensuring that no particle penetration occurs:

$$\Delta t_2 = C \min_i \left(\frac{h}{|d\boldsymbol{u}_i/dt|} \right)^{1/2} \tag{3.68}$$

The stability region must also include the restrictions from the DEM computations between two interacting solid particles, belonging to two different solids. Expression (3.59) provides an estimate for the contact duration. Lemieux et al. (2008), Campbell and Brennen (1985) and Brilliantov and Pöschel

(2001) propose that fifty time steps is enough to resolve a contact without introducing significant errors in the force computation. As such, the DEM criteria reads

$$\Delta t_3 = \frac{t_{c,ij}}{50} = \frac{3.21}{50} \left(\frac{M^*}{k_{n,ij}} \right)^{2/5} v_{n,ij}^{-1/5} \tag{3.69}$$

where M^* is taken as the reduced mass of the rigid bodies, composed of several particles. The global time step can now be chosen as

$$\Delta t_\leq C \min_i \left(\Delta t_1; \Delta t_2; \frac{\Delta t_3}{C} \right) \tag{3.70}$$

3. Numerical Discretization

4

HPC Implementation

Contents

This chapter briefly introduces the implementation techniques used to ensure maximum performance. Differences for the two computational architectures are discussed and consequences on the code are discussed.

4.1 CPU-GPU Implementation

The DualSPHysics code is the result of a state-of-the-art, highly optimized CPU and GPU implementation. The code represents the attempts to implement the best approaches for CPU and GPU, resulting in high accuracy, robustness and reliability.

Preprocessing is done using GenCase (Domínguez et al., 2011), a robust and efficient code to manage the import of geometry files, definition of basic shapes and possible combinations, specific simulation requirements (boundary movement, different physical properties of physical entities, etc). The initial conditions represent the discretization of the defined physical entities by the intersection of these volumes with a regular Cartesian grid of spacing Dp, encompassing all of the domain. At every valid node a particle is created and marked according to its nature. This strategy represents the simplest but also the most robust initial condition generator available, designed for truly arbitrary scenarios, as explored in Crespo et al. (2015). It is possible to generate particles at given positions for further fine-tunning. Post-processing is done mostly employing Paraview (Ayachit, 2015), allowing for the usage of the comprehensive filter selections and scripting capabilities for the creation of complex analysis of extensive data sets.
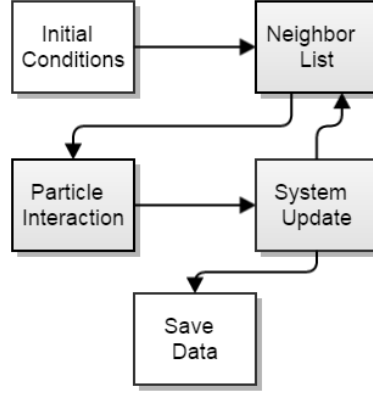
The simulations can be executed either on the CPU or on the GPU since all computations have been implemented both in C++ for CPU and in Compute Unified Device Architecture (CUDA) for the GPU. The philosophy underlying the development of DualSPHysics is that most of the source code is common to CPU and GPU which makes debugging, code maintenance and the addition of new extensions straightforward. This allows the code to be run on workstations without a CUDA-enabled GPU, using only the CPU implementation. On the other hand, the solver is implemented differently since code developers have considered efficient approaches for every processing unit architecture. The same programming strategy can be efficient on a CPU but inefficient on a GPU (or vice versa).

Algorithmically, both CPU and GPU simulations can be split into three main steps; i) generation of the neighbor list, ii) computation of the interactions between particles solving the system equations and iii) the update of physical quantities at the next time step using the chosen integration scheme. These three steps are repeated iteratively through the simulation.

4.1.1 CPU Implementation

The CPU implementation is shown in Figure 4.1.

During the first step the neighbor list is generated. A cell-linked list (Domínguez et al., 2011) is generated. This process can be divided into different operations: i) domain division into square cells of side ϵh, ii) determining the cell to which each particle belongs, iii) reordering the particles according to the cells, iv) ordering all arrays with data associated to each particle and, finally, v) generating an array with the position index of the first particle of each cell. Such procedure ensures that for a

Figure 4.1: Flowchart of CPU implementation.

particle located inside a cell, only the interactions with the particles of neighboring cells need to be considered. The number of calculations per time step is reduced from N^2 operations (for N particles) to approximately $N \log N$.
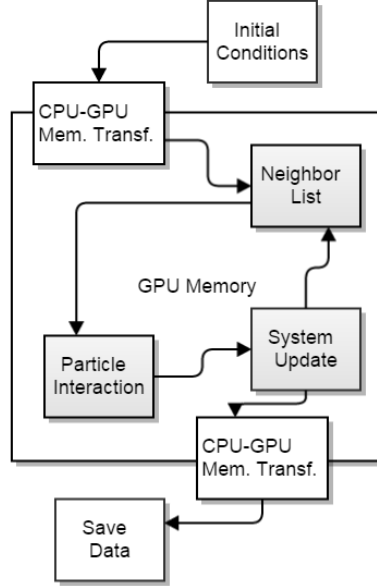
Secondly, the force computation is performed so that all particle interactions are solved according to the SPH equations. Each particle interacts with all neighboring particles located at a distance less than ϵh. Only particles inside the same cell and adjacent cells are candidates to be neighbors. Kernel symmetry, and hence kernel gradient asymmetry, avoids unnecessary repetition of particle interactions leading to a minor improvement in performance. When the force interaction of one particle with a neighbor is calculated, the force of the neighboring particle on the first one is known since they have the same magnitude but opposite direction. Thus, the number of adjacent cells to search for neighbors can be reduced if symmetry in the particle interaction is explored. Finally, the time step is computed and the quantities at step $n+1$ are calculated from the quantities that are already known at step n. The implementation is done using OpenMP in order to use every core of a multicore processor, and several optimizations have been implemented to ensure high performance.

4.1.2 GPU Implementation

GPUs constitute a suitable hardware for tasks where simple calculations are carried out across large sets of data. The work presented in Crespo et al. (2009) introduced the framework to implement SPH codes using optimal techniques regarding performance on GPU. That work focused on identifying suitable algorithms for efficient parallelization, since a proper and full use of all the capabilities of the GPU architecture is not straightforward. As an initial step, the implementation focused on solving the particle interactions on a GPU using CUDA and the next step was the implementation of the neighbor list and the time integration in order to develop an entire GPU-SPH implementation Crespo et al. (2011). Only output data requires transfer from GPU to CPU. This process, although representing a serious bottleneck due to available memory bandwidth, is rarely carried out for most applications (one out of one hundred time steps at most), representing a low percentage of the total runtime. Figure 4.2 represents the single GPU implementation.

Initially, data is allocated on CPU, so there is a single memory transfer (from CPU to GPU).

4. HPC Implementation

Figure 4.2: Flowchart of GPU implementation.

In all subsequent calculations, the three main steps are then performed on the GPU device. All the sequential tasks and operations that involve a loop over all particles are performed using the parallel architecture of the GPU cores. To save (or output) data, a new memory transfer is needed (from GPU to CPU). If saving data is not required all particle information remains on the GPU memory.

The neighbor list creation follows the procedure used on a CPU, but with important adaptations. Reordering the particles according to the cells they belong is computed using the optimized *radixsort* algorithm provided by CUDA (Domínguez et al., 2011). Figure 4.3 shows a simplified schematic diagram of the method used to generate an array of particle labels ordered according to cells and an array with the position index of the first and last particle in each cell.

Four separate arrays are used: *Id, Cell, IdSort* and *CellBegin* with a superscript * denoting sorted arrays. The array *Id* (array of particle labels) is the starting point with particles randomly located in the domain, where the order of this array corresponds to the list of particles inherited from the previous timestep. The neighbor list is created according to the following steps:

1. Particles are stored according to the cells, so the array *IdSort* is created;

2. The array *Cell* is also created where an entry gives the cell to which the particle of the same index in *Id* belongs, e.g. *Id(2) = 3* which is located in *Cell 6* hence *Cell(2)=6*. Cell labels are depicted in green color in Figure 4.3.

3. Using *radixsort*, array *Cell* is reordered following the order of the six cells and *Cell** (reordered *Cell*) is used to reorder *IdSort* according to the cells the particles belong.

4. Once *IdSort** is generated, all the arrays with particle information (*Id, Position, Velocity, Density...*) are ordered giving rise to the new arrays (*Id_new, Pos_new, Vel_new, Dens_new...*) considering that $Id\_new[i] = Id[IdSort^*[i]]$. For example, $Id\_new[2] = Id[IdSort^*[2]] = Id[7] = 4$, in
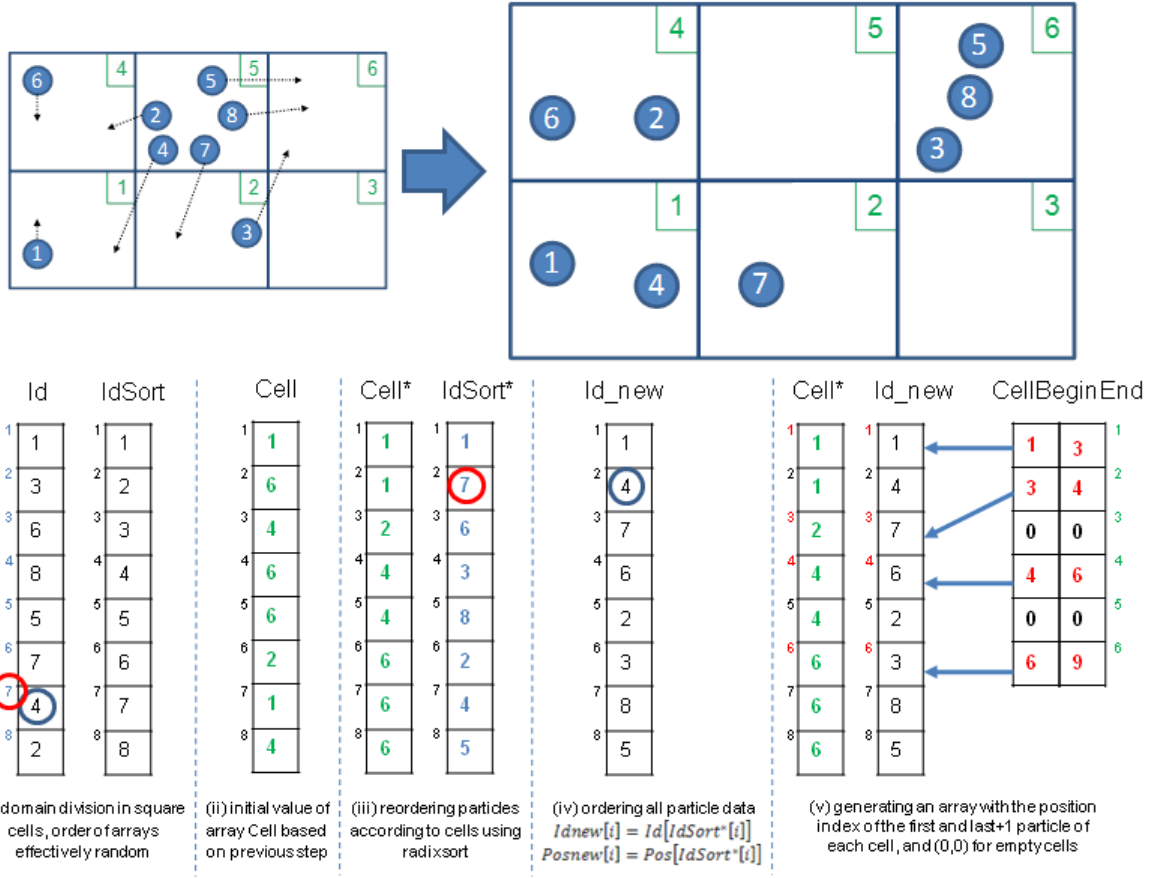
Figure 4.3: Example of the Neighbor list procedure (Crespo et al., 2011)

Figure 2 a blue circle marks the particle 4 and a red circle marks the 7th position.

5. Finally, *CellBeginEnd* is created with the indexes (position in data arrays) of the first and last+1 particles of each cell. Indexes have been written in red color in Figure 4.3. For example the first particle of the cell number 2 is the particle 7, whose position index is 3 in all particle property arrays, so the second value of *CellBeginEnd*, which corresponds to cell number 2, will be 3 and 4 (3+1). In this way, the amount of particles in the cell k will be *CellBeginEnd*[k].y − *CellBeginEnd*[k].x.

Particle interactions for the computation of the forces, from equation (3.36), are a key process that must be implemented in parallel. The use of the shared memory of the GPU was analyzed to reduce the access to the global memory. However, when the SPH code is implemented entirely on the GPU, this technique is not viable for current devices. For example, when the number of particles is large, the size of shared memory is not enough to allocate the properties of all the particles belonging to the same cell.

Particle interactions were implemented on the GPU using one execution thread per particle, to compute the force resulting from the interaction with all its neighbors. At first, this implementation seems to present some performance limitations. The workload of threads inside one block is not balanced since particles can have different numbers of neighbors. Code divergence is also a concern in

this context, since the possible neighbors of a particle include both particles inside the kernel compact support ($r_{ij} < \epsilon h$) and outside ($r_{ij} > \epsilon h$), leading to an imbalance on the work of the threads. These limitations are made less relevant by careful usage of shared memory, function inlining and other techniques, rendering the approach the most flexible and performant option available.

An important difference from the CPU part of the DualSPHysics code is that the symmetry of the particle interaction cannot be applied on a GPU implementation, since each thread is responsible for the interaction between a target particle and its neighbors. Thus, each thread must be the only one that computes the forces exerted on a given particle. The access to the global memory of the device is irregular because there is no way to organize the data to get a coalesced access for all the particles.

4.1.3 Multi-GPU Message Passing Interface (MPI) Implementation
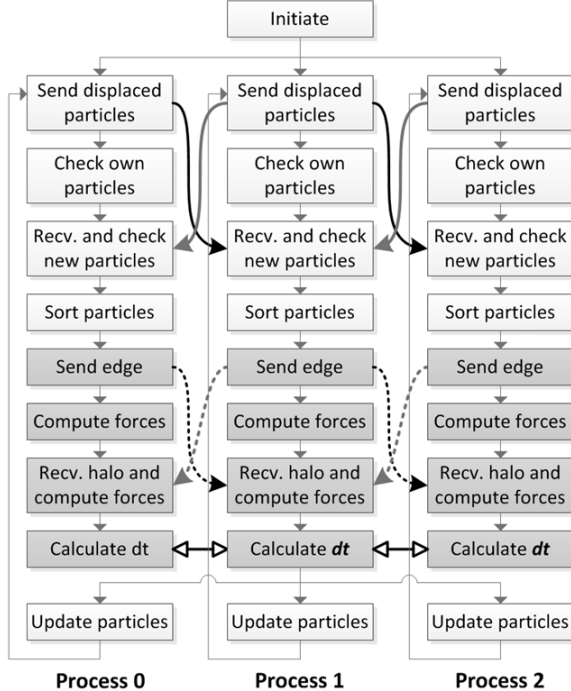
The physical domain of the simulation may be divided into subdomains, distributed among different MPI processes. Each process only needs to assign resources to manage a subset of the total amount of particles for each subdomain. Thus, the size of the simulation scales with the number of machines.

The division can be performed in any direction (X, Y or Z) according to the nature of the simulation case. The employed topology can result on two neighboring subdomains, by slicing the domain along the main direction of the problem, or in blocks, for more general cases. Each MPI process needs to obtain, at every time step, the data of neighboring particles from the surrounding processes within the interaction distance (ϵh), in order to compute forces. This region is called the halo of the process (or subdomain). The details of the approach are further explained in Domínguez et al. (2013).

Reducing time dedicated for exchanging data among MPI processes is essential to increase the number of processes without decreasing efficiency. One method to achieve this is by overlapping the communication with the computation using asynchronous communications. One process can send (or receive) information to another while carrying out other tasks without waiting for the end of the transfer.

Figure 4.4 shows the data exchanges that take place at each time step when using MPI. At the beginning of each time step, during the neighbor list creation, each process looks for the particles that move from one subdomain to another and these displaced particles are sent to the corresponding process. While data of displaced particles are sent (solid arrows in Fig. 4.4), the neighbor list of the particles in the interior of the domain (particles not in an edge) is processed. Finally, the new particles that entered the domain are received for each process and all particles are sorted. At this stage, the computation time that is overlapped with the transfer of particles is reduced, but this is not a problem because the number of particles that change from one domain to another at each step of the simulation is typically much smaller than the number of particles in a given sub-domain.

During the force computation, each process sends its edges to the surrounding processes (dashed arrows in Fig. 4.4). While edges are being sent and the halo is received, computation of the force on the interior particles is performed. Once this is finished, the process waits for the reception of the first halo and computes forces of one edge with this halo. After that, the process waits to receive the second halo and computes the forces of the other edge. Thus the most expensive halo-edge data transfers are

Figure 4.4: Example of the communications among 3 MPI processes (Domínguez et al., 2013)

overlapped by calculating the forces between particles. As all particle data are allocated in the GPU memory, data transfer is also needed between CPU and GPU memory. However, it should be noted that the cost is negligible since the volume of information is low and one of the advantages of the method proposed here is that the data to be transferred are stored in contiguous memory locations, accelerating the process.

Particles move through space during the simulation so the number of particles must be redistributed after some time steps to maintain a balanced work load among the processes and minimize the synchronization time. Most of the total execution time is spent on force computation, and this time depends mainly on the number of fluid particles. For an equal load per processor, the domain must be divided into subdomains with the same number of fluid particles (including particles of the halos) or with the number of particles appropriate to the computing power of the device assigned to it. Hence two different dynamic load balancing algorithms are used. The first one assigns the same number of particles to each computing device, and is suitable when the simulation is executed on machines that present the same performance. The second load balancing algorithm is used when hardware of different specifications and features are combined, such as different models of GPU. This second approach takes into account the execution time on each device. In particular, a weighted average of the computing time per integration step over several steps is used, with a higher weight to the most recent steps. An average over many time steps is chosen because a single time step may present large fluctuations. This average time is used to distribute the number of particles so that the fastest devices can compute subdomains with more particles than the slower ones.

4. HPC Implementation

4.1.3.A   Rigid Body MPI Chalenges

Standard SPH is attractive for MPI paralelization since only three sets of data from the process halos need to be exchanged: position, velocity and density, and the communication events per time step are limited. Adding rigid bodies adds a layer of complexity since relational information must be considered. The particles of the rigid bodies must be identified and treated in a separated cycle after the main interaction. Just by identifying the corresponding body, using a 2 byte array, an increase in the communicated data between processes of over 7% is expected, considering only interaction.

The movement update of the rigid bodies requires the summation of quantities from all its particles, as expressed in equations (3.49) and (3.50). As a body may be in more than one process at the same time, it is necessary to compute the partial summations on every GPU and share those values to obtain the final configuration in all of them. In this manner, each GPU can update its corresponding part of the rigid bodies independently. Clearly the ideal solution would be that communications were restricted between machines that shared an object, but such option forces a synchronization so that each process knew which other processes had particles from each rigid body. The best and simplest option seems to be the partial computation of the body quantities and a collective communication taking place subsequently.

5

Validations and Tests

5. Validations and Tests

This chapter attempts at quantifying the quality of the numerical solutions achieved with the methods introduced in Chapter 3. Theoretical considerations and analytical solutions are taken into account when available, providing important comparison points. Experimental data is complied from literature and derived from measurements, allowing for a more comprehensive study of the numerical model when faced with complex scenarios.

Unless otherwise stated, all simulations are performed with Equations (3.30), (3.36) with viscous terms from the laminar (Equation 3.35) and SPS formulations (Equation 3.41), EOS (Equation 3.42) and the non-linear contact mechanics models explored in Section 3.3.2.

5.1 Fluid Flow

Two cases with no free surface are considered in Sections 5.1.1 and 5.1.2. These are, in contrast to free surface tests, relatively unused validation cases for fluid flow in the hydraulics community. In recent years SPH has matured rapidly as a method and current machines allow for large cases to be tested. Traditional dam-break flow, explored in Crespo et al. (2007), Violeau and Issa (2007) and Gómez-Gesteira et al. (2010), among others, were extensively validated, considering velocity of the wave front, free surface deformation and forces on static obstacles. For this reason, a less traditional approach is taken in Section 5.1.3: experimental velocity fields from a downward gate set-up are compared with the numerical solution.
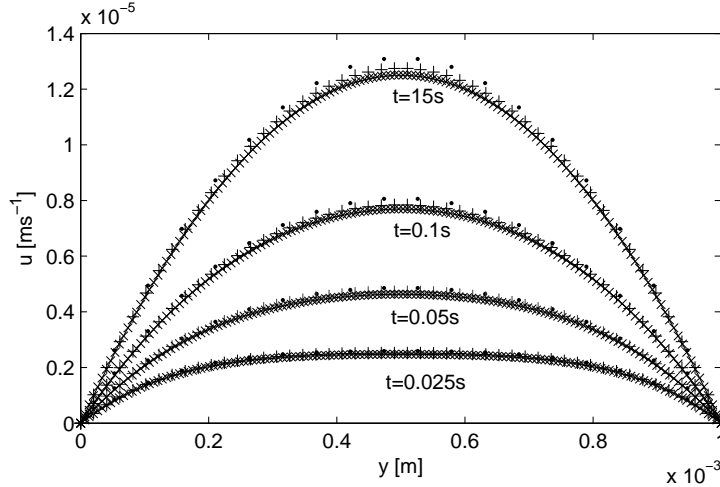
5.1.1 Hagen-Poiseuille Flow

The first solution of the Navier-Stokes that will be explored is the Hagen-Poiseuille flow. The problem was first explored experimentally by Gotthilf Heinrich Ludwig Hagen in 1839 and Jean Léonard Marie Poiseuille in 1838, and published by Poiseuille in 1840 and 1846. The conditions are simple: the flow is laminar through a pipe of constant circular cross-section that is substantially longer than its diameter. The original experiments did not account for acceleration of fluid. For velocities and pipe diameters above a threshold, the fluid flow becomes turbulent, leading to larger pressure drops than calculated by the Hagen-Poiseuille equation.

Admitting conditions for a laminar Hagen-Poiseuille flow, the Navier-Stokes equations allow analytical solutions. A transient solution can be derived using Fourier series (Drazin and Riley, 2006) and Morris et al. (1997) used the solution to test the laminar viscous term in Equation (3.35). Since the discretization of the momentum equation is not exactly the same, SPS terms are introduced and the solid boundary conditions are very different, the same exercise is reproduced here. Of special concern are the SPS terms, since the simple Smagorinsky model is known to introduce non-zero tensions in a laminar flow (Batchelor, 2000). For a fluid initially at rest between stationary infinite plates at $y = 0$ and $y = L$, with an applied body force $\boldsymbol{F}$, acting parallel to the axis of the channel, the series solution for the velocity u along the channel cross-section is given by

$$u(y,t) = -\frac{|\boldsymbol{F}|}{2\nu}y(y-L) - \sum_{n=0}^{\infty} \frac{4|\boldsymbol{F}|L^2}{\nu\pi^3(2n+1)^3} \sin\left(\frac{\pi y}{L}(2n+1)\right) \exp\left(-\frac{(2n+1)^2\pi^2\nu}{L^2}t\right) \qquad (5.1)$$

Employing $\nu = 10^{-6}$ m^{2}s^{-1}, $L = 10^{-3}$ m, $|\boldsymbol{F}| = 10^{-4}$ ms^{-2}, the maximum velocity, taken from the first term of Equation (5.1) (or $t = \infty$) is $u_{max} = 1.25 \times 10^{-5}$ ms^{-1}, resulting in $R_e = u_{max}L/\nu = 1.25 \times 10^{-2}$. The 2D simulations were carried out with an initial particle spacing of $L/Dp = 20$, $L/Dp = 50$ and $L/Dp = 150$ and a smoothing length defined as $h = \sqrt{2Dp^2}$, resulting in numerical solutions that can be compared with expression (5.1) at chosen time instants. The domain is 5×10^{-3} m long and periodic conditions are applied in the longitudinal direction. Figure 5.1 shows the numerical and time series solutions.

Figure 5.1: Series solution (–) and SPH solution $L/Dp = 20$ ($\cdot$), $L/Dp = 50$ (+), $L/Dp = 150$ ($\times$) for $R_e = 1.25 \times 10^{-2}$, at several instants.

The results show that the transient nature of the flow is well captured at all resolutions and relative errors, although larger for the less resolved $L/Dp = 20$ case, is limited to 5%, with the maximum of 0.1% for the $L/Dp = 150$ case. These results are compatible with the reported by Morris et al. (1997), indicating that the introduction of the SPS terms does not appear to corrupt the laminar solution. Computing the Root Mean Square Error (RMSE) of the solution for $t = 15$ s, we can obtain some insight into the convergence rate of the solution, as presented in Figure 5.2.
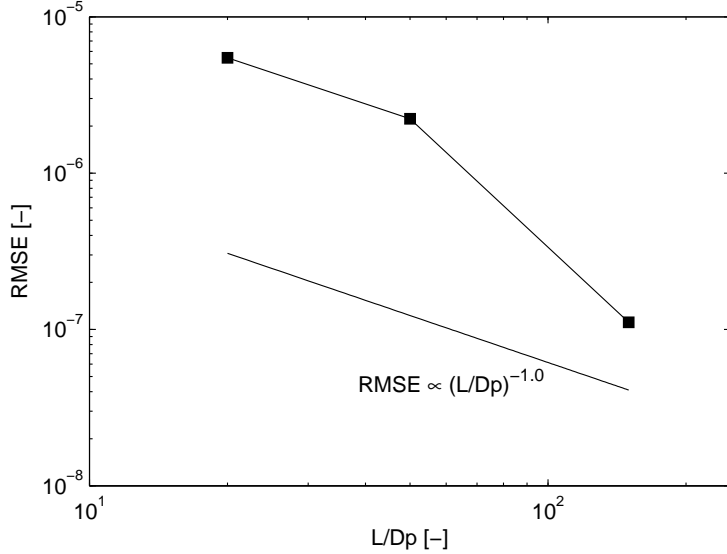
The convergence rate for increasing resolution seems to be supra linear in this case. A more complete convergence test would include changing the smoothing length h, as presented in Dehnen and Aly (2012).

5.1.2 Couette Flow

Couette flow is, similarly to the Poiseuille flow explored in the previous section, developed between two infinite plates. For the transient flow, the system is introduced at rest. For $t = 0$ s, the upper plate starts to move parallel to the longitudinal direction, at a constant velocity V_0. This introduces a shear stress that promotes the flow. Drazin and Riley (2006) introduced the series solution amending the analytical solution
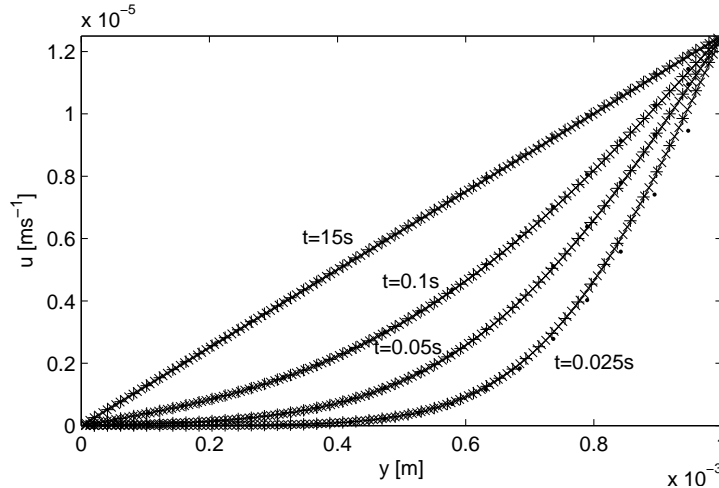
$$u(y,t) = \frac{V_0}{L}y + \sum_{n=1}^{\infty} \frac{2V_0}{n\pi}(-1)^n \sin\left(\frac{n\pi}{L}y\right) \exp\left(-\frac{n^2\pi^2}{L^2}\nu t\right) \tag{5.2}$$

5. Validations and Tests

Figure 5.2: RMSE with increasing resolution. Linear convergence slope for comparison.
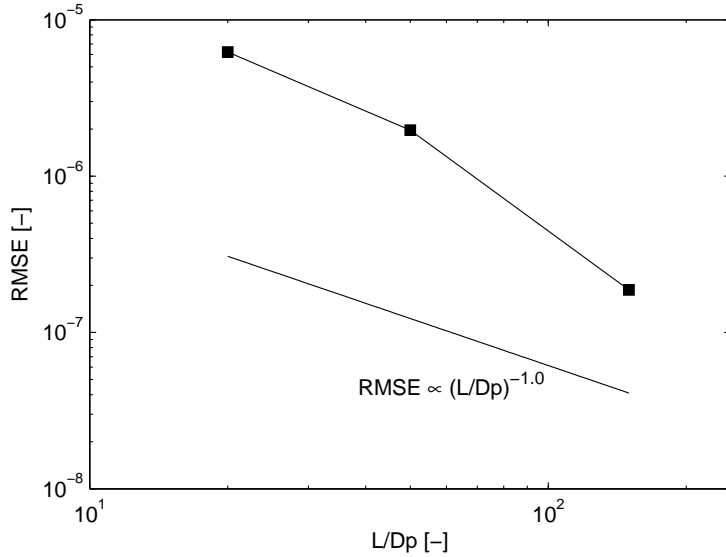
The flow was modeled using $\nu = 10^{-6}$ m^{2}s^{-1}, $L = 10^{-3}$ m and $V_0 = 1.25 \times 10^{-5}$ ms^{-1}, with initial particle spacing of $L/Dp = 20$, $L/Dp = 50$ and $L/Dp = 150$ and the same scheme constants as in last Section. The Reynolds number is also the same, $R_e = 1.25 \times 10^{-2}$. The domain is 5×10^{-3} m long and periodic conditions are applied in the longitudinal direction. Figure 5.3 shows the numerical and time series solutions.


Figure 5.3: Series solution (–) and SPH solution $L/Dp = 20$ (·), $L/Dp = 50$ (+), $L/Dp = 150$ (×) for $R_e = 1.25 \times 10^{-2}$, at several instants.

The numerical solution presents a good agreement. In the initial instant, the $L/Dp = 20$ solution presents a deviation to the analytical velocity profile, with 5.8% relative error in the vicinity of the mobile boundary. By the second instant however, the velocity profile is now coincident, with less than 0.7% maximum error. Again, computing the RMSE of the solution for $t = 15$ s, in Figure 5.4, the convergence rate for the tested resolution range can be estimated.

The convergence rate for the Couette case seems to be supra linear also, with the error distribution taking a similar form to the Haggen-Poiseuille case.
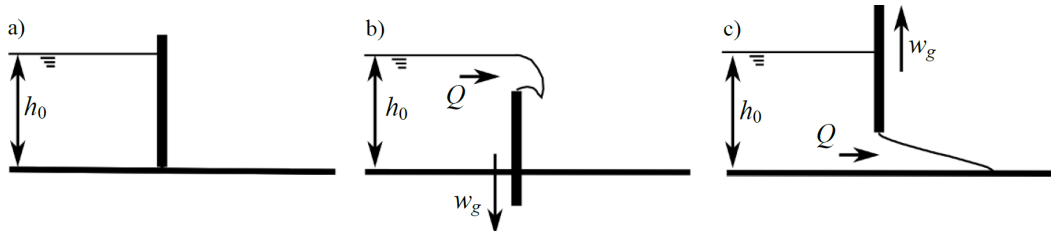
Figure 5.4: RMSE with increasing resolution. Linear convergence slope for comparison.

5.1.3 Dam Break Flow

Advances in imaging techniques and processing power allow for the measure not only of the wave celerity and water level time series, but also the point-wise velocity field (Aleixo et al., 2011; Oertel and Bung, 2012). This represents an interesting validation test for resolved models, since it allows to quantify not only global or average dynamics, but also local and time dependent quantities. The traditional dam break data used for validation (Violeau and Issa, 2007; Gómez-Gesteira et al., 2010) relies on free surface deformation tracking and wave front velocity, but it is uncommon for experimental velocity profiles to be measured and numerical solutions to attempt comparisons.

An instantaneous dam break may be represented mathematically by an Initial Value Problem (IVP), simply as a discontinuity in the quantities. Due to the mathematical properties, most numerical studies are focused in this particular dam break. Different strategies can be found in the literature in order to experimentally simulate an instantaneous dam break, with the most used relying on the fast vertical displacement of a gate. This vertical displacement can be downward or upward as represented in Figure 1 b) and c) respectively. Upward moving gates are the traditional mechanism to study dam breaks. They present interesting qualities but introduce inevitable artificial sediment entrainment if the bed is covered with mobile sediment. Downward moving gates attempt to correct that effect, and have been used by Spinewine and Zech (2007) and Aleixo (2013).

Figure 5.5: a) Scheme of a dam with initial height, h_0; b) downward moving gate; c) upward moving gate. Q denotes the flow rate after the gate opening and w_g the gate vertical velocity.
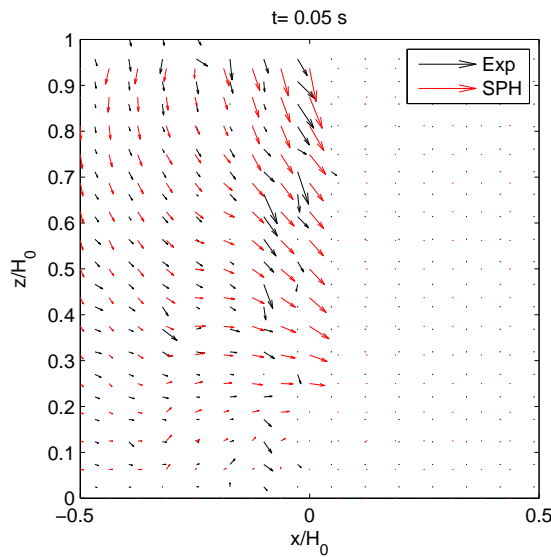
5. Validations and Tests

The measurements were carried in the dam-break channel of the Institute for Mechanics Materials and Civil Engineering, Universite Catholique de Louvain, Belgium. This channel is characterized by a width of 0.25 m, 0.50 m height and a 6 m length. Glass windows allow optical access to the flow. At half of its length a 0.0025 m thick aluminum gate was placed in order to simulate the dam-break flow. The gate separates the channel in two sections and is centered on the area of interest. This gate is connected to a pneumatic jack that drives the gate downward. The bottom of the reservoir section is made of impervious polished wood whereas the bottom of the test section is made of glass.

To analyze flow a DALSA 1M150 fast camera was used. It has a maximum resolution of 1 Mpixel and an adjustable acquisition frequency of 150 Hz; in the present case however the acquisition frequency was set at 100 frames per second and an 8 mm lens was used. In order to measure the flow velocity the water of the reservoirs was seeded with High Density Polystyrene particles ($\rho/\rho_w = 0.94$), with a diameter of 2 mm. To improve the light reflection from the particles these were coated with a white paint. Combination of the particle density and the denser white coating made the resulting particles roughly neutrally buoyant (Aleixo et al., 2011). To track the particles motion a Voronoï-based particle tracking algorithm (Capart et al., 2002) was used.
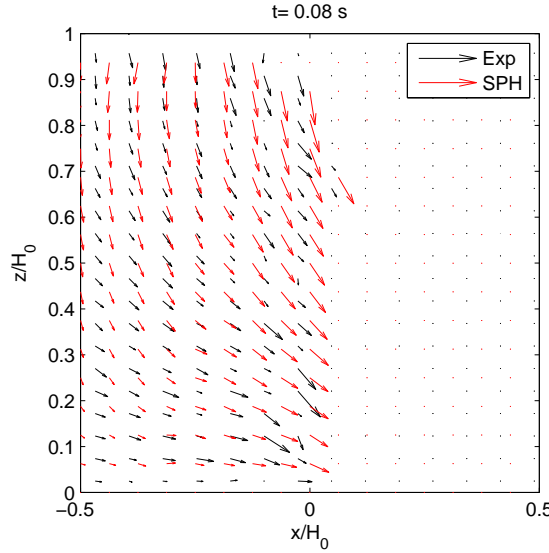
Aleixo (2013) demonstrated that for a depth of $h_0 = 0.325$ m, the gate is removed in under 70 ms. This corresponds to an instantaneous removal, using the criteria from Lauber and Hager (1998): $t_o(h_0 = 0.325) = \sqrt{2h_0/g} \approx 0.26$ s.

A 2D SPH simulation was prepared with $Dp = 0.001$ m, where the gate motion was imposed with the corresponding velocity. The smoothing length was $h = \sqrt{2Dp^2}$, the C parameter from the stability region condition, Equation ((3.70)), was set at 0.20 and the kinematic viscosity is that of water at $20°$ C temperature, $\nu = 10^{-6}$ m^{2}s^{-1}. The velocity fields in Figures 5.6 to 5.9 represent the overlap of experimental and numerical data, interpolated to similar regular grids over the domain, over time.
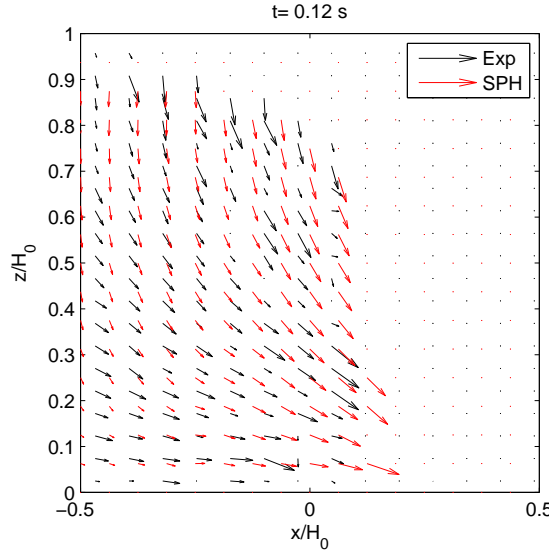

Figure 5.6: Velocity fields, experimental and SPH solution. $t = 0.05$ s.

The velocity fields are quite similar in direction and the evolution on time of the SPH solution

Figure 5.7: Velocity fields, experimental and SPH solution. $t = 0.08$ s.
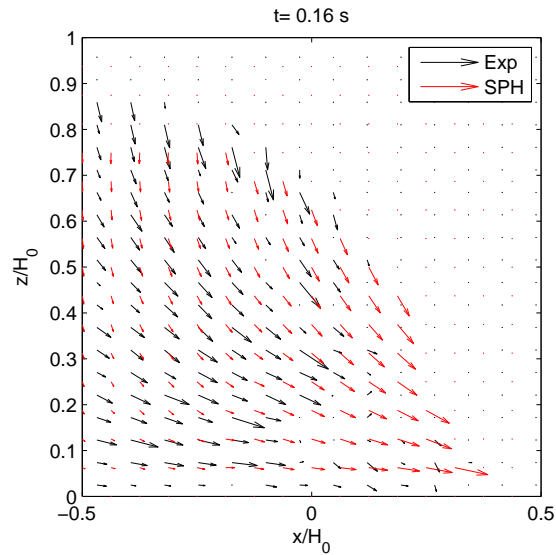
Figure 5.8: Velocity fields, experimental and SPH solution. $t = 0.12$ s.

seems consistent with the experimental data. To further quantify the differences, vertical profiles were derived, in Figures 5.10 to 5.12, using a dimensionless velocity defined as
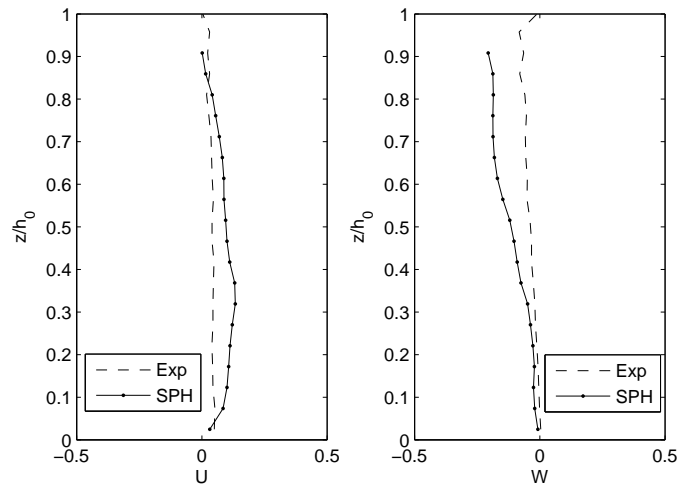
$$U = \frac{u_1}{\sqrt{gh_0}}; \quad W = \frac{u_2}{\sqrt{gh_0}}, \tag{5.3}$$

where u_1 and u_2 correspond to the horizontal and vertical velocity components, respectively.
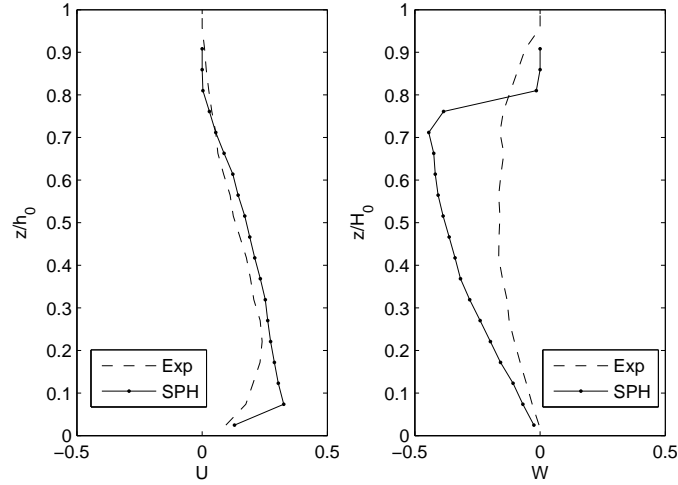
5. Validations and Tests
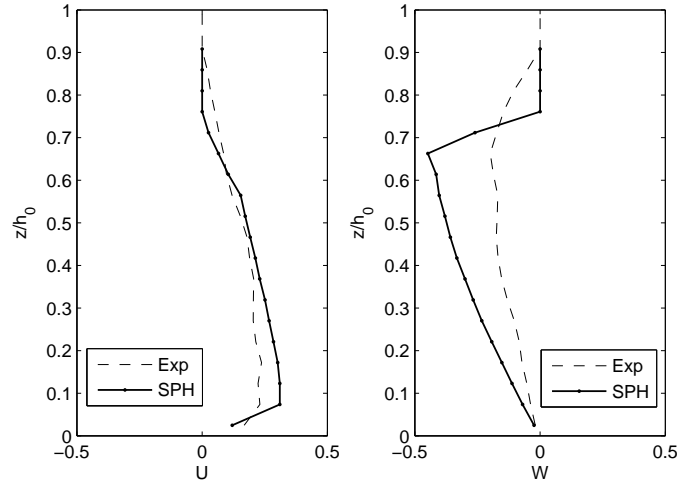
Figure 5.9: Velocity fields, experimental and SPH solution. $t = 0.16$ s.

Figure 5.10: Velocity profiles, experimental and SPH solution. $t = 0.07$ s.

Figure 5.11: Velocity profiles, experimental and SPH solution. $t = 0.16$ s.


Figure 5.12: Velocity profiles, experimental and SPH solution. $t = 0.19$ s.

The profiles show that the longitudinal velocity u_1 is well represented, showing the same tendencies as the experimental data. The vertical velocity u_2 seems to be larger on the numerical solution. The larger deviations may stem from experimental difficulties, as the tracer particles may suffer from a small upwards buoyant force. Experimental data was also interpolated and further smoothed to trace the profiles, as can be checked since the free surface does not seem to be well defined, also partly explaining the differences on the upper section of the flow, relative to the vertical velocity component, in Figures 5.11 and 5.12. Note that the SPH profile is interpolated in points coinciding with the experimental measures, thus generating the visible gradient at the free surface area.
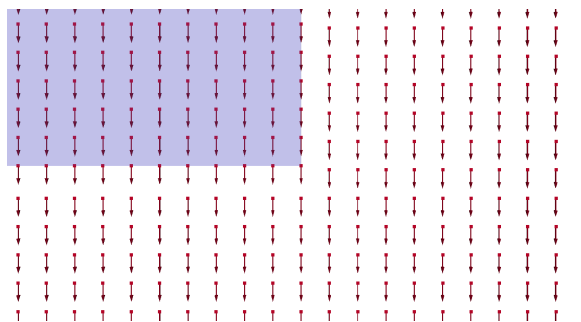
5.2   Rigid Bodies: Fluid-Structure Interaction

Section 5.1 introduced some validations of the proposed SPH method, exclusively dealing with fixed, or with otherwise imposed motion, solid boundaries. In this Section, boundaries with DOFs are studied. As described in Chapter 1, the fluid and rigid body problem within SPH discretizations has been treated previously and validations have been presented. The next Sections focus on the comparison of buoyancy and fluid-structure interaction with available solutions. Numerical stability and qualities of the implementation are also addressed in idealized cases.

Due to insufficient solutions and data on complex, multi-body free surface fluid-structure inter-actions, an extensive experimental campaign was designed and carried out, as explored in Section 5.2.4.

5.2.1   Free stream consistency

A simple property of a discretization method should be free stream compliance. For a given velocity of the fluid and the rigid body, given that initial relative velocities are zero, they should remain zero as time evolves and the equations are integrated, showing that there are no errors in the integrators and that these are robust regarding truncation errors. The first case consists of a $6 \times 6 \times 6$ m patch of fluid and a $2 \times 2 \times 2$ m rigid square in the center of the fluid, with a $Dp = 0.05$ m initial inter particle spacing, equal in all three dimensions. Both are given a $u = 1$ ms^{-1} initial velocity, gravity acceleration is zero and there are no other solid boundaries. Figure 5.13 shows a bidimensional slice of the velocity field, around the lower right corner of the rigid square.
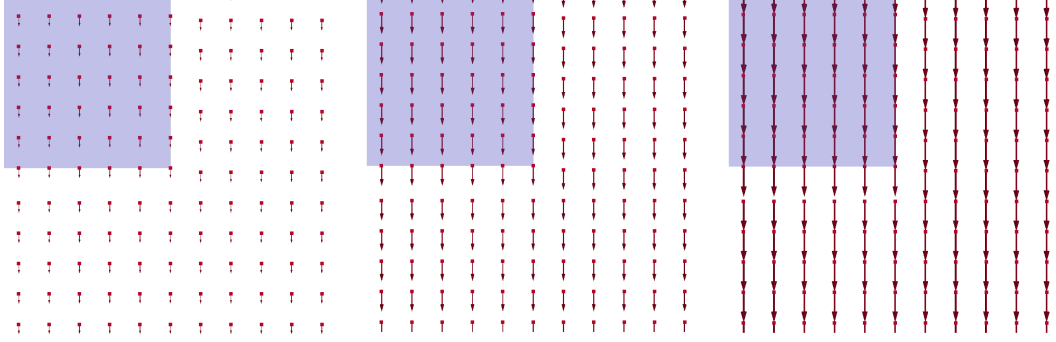
Figure 5.13: Velocity field detail for a corner of the square at any time step.

The field is constant in time, no deviations along the solid-fluid interface were introduced during the 30 s of simulation.

A more demanding case is to consider a non-zero acceleration, since numerical errors arising from the usage of two sets of equations (for fluid and rigid bodies) should be more noticeable. The same geometry as for the previous example is set up, but with zero initial velocity and non-zero constant acceleration. Figure 5.14 shows a slice of the velocity fields at three separate instants.

The error of the object velocity comparing to the overall field is neglectable in the first two snapshots and reaches 0.13% for third one. The same conclusions as for the first case can be drawn: the velocity field evolves without irregularities being developed at the fluid-solid interface, streamlines are virtually not disturbed by numerical errors.

Figure 5.14: Velocity field detail for a corner of the square at $t = 5s$, $t = 10s$ and $t = 15s$.

5.2.2   Buoyancy and Fluid/Solid Interfaces

5.2.2.A   Fluid/Solid Interfaces
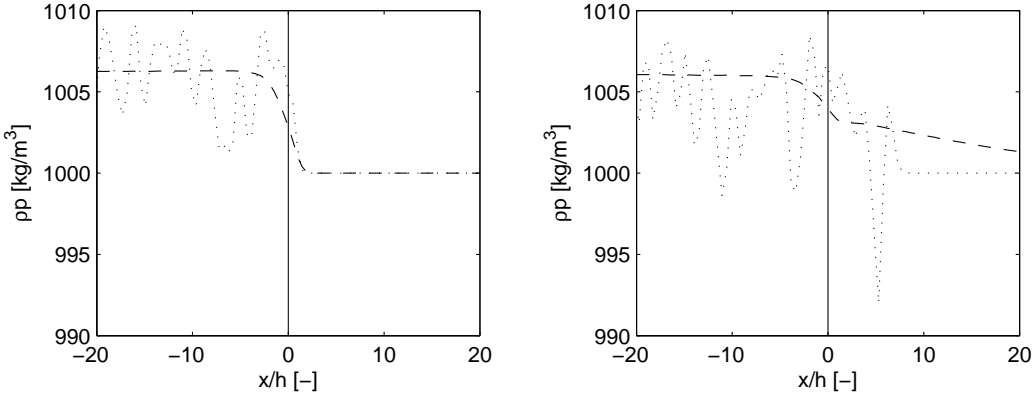
The interface between fluid and solid particles is subjected to similar deficiencies as described for large density ratio cases Colagrossi and Landrini (2003), in this case generated by forcing the relative position of the solid phase particles. An overestimation of the density on the solid particles occurs, producing a hydrophobic effect that results in a reorganization of the fluid particle positions. This happens in order to cope with the increased density gradient at the interface and the entropy jump that occurs, considering that the solid particles are ordered strictly, not necessarily generating a constant equilibrium distance for a fluid particle across the interface. The δ-SPH term prescribed in expressions (3.45) and (3.46) effectively curb these cascade behaviors by not allowing an erroneous density field to be computed at the interface locus. Figure 5.15 illustrates the difference in particle distribution with and without the δ-SPH term across a fluid-solid interface of a cylinder with $r = 1$ m.

Figure 5.15: Fluid-solid interface. Left $\delta = 0$, right $\delta = 0.1$

Figure 5.16 shows the density profiles in a normal direction to the interface. The profiles show the density fluctuations around the interface for a static and a moving boundary. The moving boundary was created by moving the cylinder at $v = 0.1$ m/s. On the fluid region one can see a large density overestimation in both cases, causing the particles to rearrange as in figure 5.15, in accordance with the findings of Saitoh and Makino (2013). With a non-zero δ the density profile is smooth and no fluctuations are detected, enabling the fluid particles to remain at similar distance from the solid and other fluid particles. The kernel should now present a more uniform stencil, providing more accurate interpolations.

5. Validations and Tests

Figure 5.16: Density profiles for $t = 10$ s. Left, non-mobile boundary, right, mobile boundary. Interface position (—), δ=0 ($\cdots$), δ=0.1 ($---$)

5.2.2.B Buoyancy: analytical and numerical solutions

Since the interface description seems to perform as expected, the traditional way to verify the integrity of the terms is by analyzing the buoyancy driven motion of bodies in a fluid. The used configuration consists of a cylinder, whose density is different from that of the fluid, initially placed at a specific depth in a viscous fluid. Both fluid and solid body are initially at rest. Once the motion is initiated, the rate of change of cylinder momentum is, for large values of cylinder Reynolds number (Re_p), essentially a function of: i) the body forces associated to the virtual added mass, ii) the Basset history[1], iii) the buoyancy, iv) the surface forces associated to the gradient of hydrodynamic variables, of which the pressure gradient (buoyancy not included) is the dominant term, and v) viscous drag Crowe et al. (1998). The latter, for large Re_p depends on the square of the relative velocity and on a drag coefficient which is approximately 1 in the range $Re_p = 1 \times 10^4$ to 3×10^5.

Moyo and Greenhow (2000) studied this problem using an inviscid flow model that included only the effects of buoyancy, of the virtual added mass and the pressure gradient. Fekken (2004) later compared these results with those of another inviscid solution including only added mass and buoyancy and with those of a numerical model based on a VOF discretization technique. The latter provides the most relevant comparison, since viscous stresses for the fluid and drag forces on the cylinder are considered and the VOF method explicitly tracks free surface geometry changes without any special treatment, unlike the solution of Moyo and Greenhow (2000).
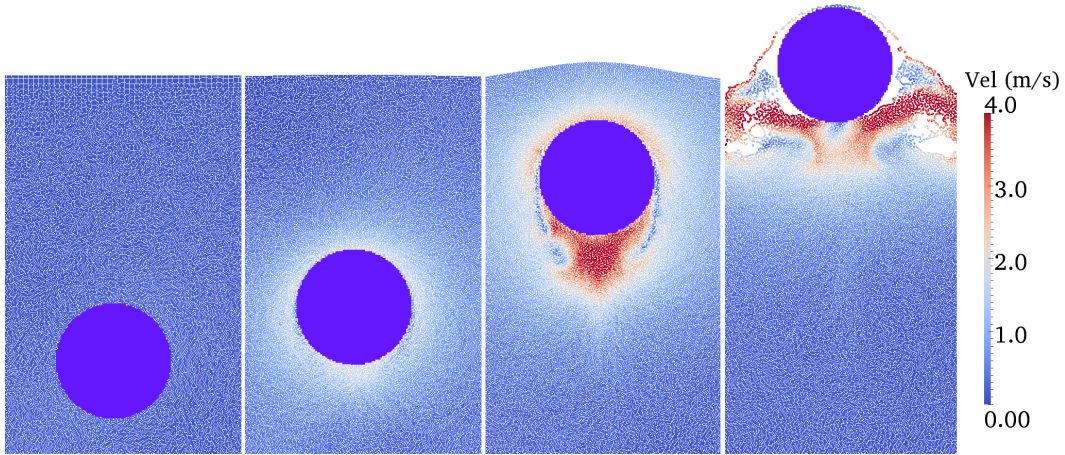
The simulations reproduce the conditions described in Fekken (2004): cylinders with a $r = 1m$ radius and densities $\rho = 0.6\rho_w$ and $\rho = 0.9\rho_w$ are placed at a depth of $D = 5$ m, measured from the free-surface to the centroid of the cylinder. The 2D simulation has a domain of an $8m$ long periodic box with a fluid depth of $7m$ and a rigid boundary at the bottom. The initial inter particle spacing are $D/Dp = 66$, $D/Dp = 100$ and $D/Dp = 150$. Cylinder velocities are computed at the centroid of the cylinder and are non-dimensionalised as $V = u/\sqrt{gr}$, were u is the velocity and g is the acceleration of gravity. Time is made non-dimensional as $T = t\sqrt{g/r}$.

Figure 5.17 shows the system for the case $\rho = 0.6\rho_w$ at four instants and Figure 5.18 shows the

---
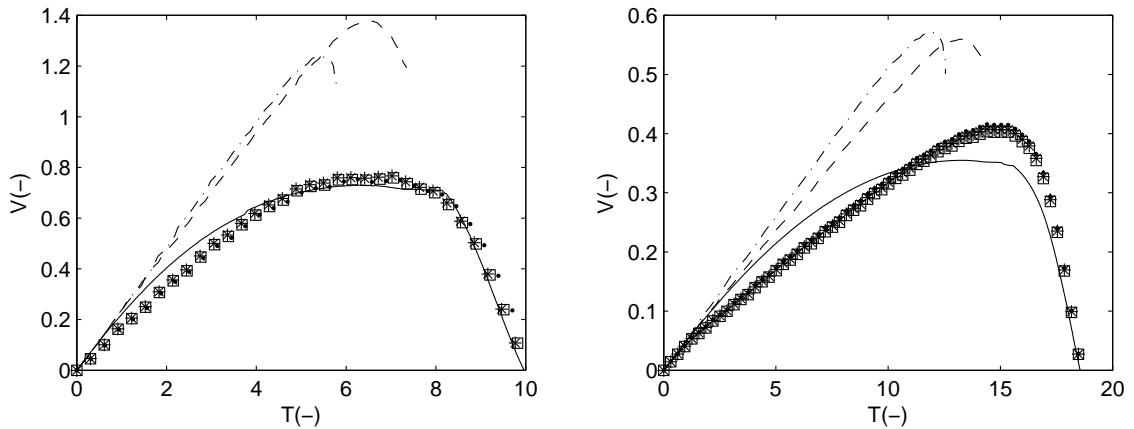
[1]Many times neglected, this term represents the temporal delay in boundary layer development as the relative velocity changes with time (Crowe et al., 1998).

velocity of the cylinders for both cases.

Figure 5.17: Rising cylinder with $\rho = 0.6\rho_w$. $T = 0$; $T = 3.13$; $T = 6.26$; $T = 9.40$.

**Figure 5.18:** Non-dimensional vertical velocity for a cylinder. Left - $\rho = 0.6\rho_w$; Right - $\rho = 0.9\rho_w$. Added mass model(analytical)Fekken (2004)$(-\cdot-)$; Moyo & Greenhow(analytical)Moyo and Greenhow (2000)$(---)$; Fekken(VOF)Fekken (2004)$(-)$; DualSPHysics $D/Dp = 66(\bullet)$, $D/Dp = 100(*)$ and $D/Dp = 150(\square)$.

The value Re_p is larger than 1×10^4 for cylinder velocities larger than 1 cms^{-1}, which is equivalent to $V > 0.003$. Also, $Re_p = 3 \times 10^5$ is attained at $V = 0.096$. Phenomenologically, and in what concerns the drag force, it is expected that between $V = 0.003$ and $V = 0.096$ the separation point of the laminar boundary layer attached to the cylinder remains stable and, as a consequence, Re_p effects are negligible, with the value of the drag coefficient remaining close to 1. At approximately $V = 0.096$ the boundary layer becomes turbulent, the separation point progresses considerably and the drag coefficient is reduced. From this point onwards the drag coefficient becomes a mild increasing function of Re_p. Basset forces should become relevant only near the free-surface, when the cylinder decelerates. Near the free-surface virtual added mass and pressure gradients vary non-linearly with the overall effect of reduction the cylinder acceleration to the point of becoming negative (Frank, 1967).

Observing the results shown in Figure 5.18 one notes that the inviscid models of Moyo and Greenhow (2000) and Fekken (2004) show a linear evolution of the velocity while the cylinder is far from the free-surface which, given that viscous terms are absent, indicates that both added mass and pressure

5. Validations and Tests
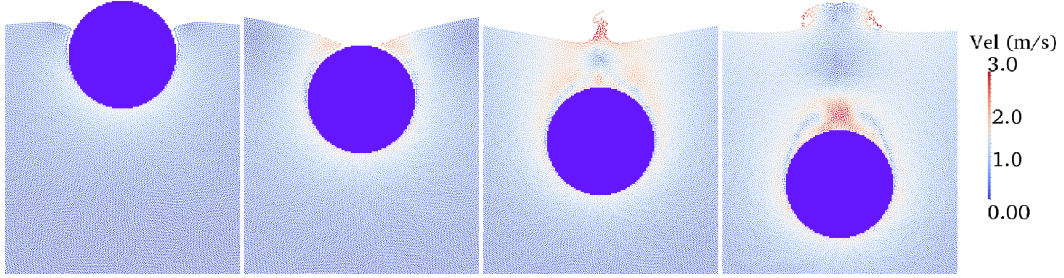
gradients remain approximately constant in this reach. Closer to the free-surface, their models feature the expected reduction of cylinder acceleration. The VOF model of Fekken (2004) agrees with the inviscid models in what concerns the initial acceleration and initial velocity (up to $V = 0.18$ in the $\rho = 0.6\rho_w$ case and up to $V = 0.1$ in the $\rho = 0.9\rho_w$ case). The present solutions feature a smaller acceleration, relatively to the inviscid solutions, for $V > 0$, in the case of $\rho = 0.6\rho_w$, and for $V > 0.05$, in the case of $\rho = 0.9\rho_w$. The fact that both VOF model of Fekken (2004) and the present solutions disagree with the inviscid solutions for most of the simulation reach can be attributed to the existence of viscous forces in the former models. The slightly lower velocities observed in the present simulations relatively to the VOF solution (for $T < 4$ in the $\rho = 0.6\rho_w$ case and $T < 10$ in the $\rho = 0.9\rho_w$ case) can be due to the different discretization techniques and numerical approaches for fluid-solid interaction.

The effects of the changes in the nature of the cylinder boundary layer are not immediately visible in the VOF solution of Fekken (2004) and in the present solutions. Indeed, Figure 5.18 shows that there are no apparent discontinuities in the slope of the VOF solutions. The present simulations do show a change in acceleration at $V = 0.1$, for the $\rho = 0.6\rho_w$ case, and at $V = 0.07$, for the $\rho = 0.9\rho_w$ case. However, it is not obvious if this is related to the breakdown of the laminar boundary layer (that should occur at $V = 0.096$) since, in both cases, there is a local reduction of acceleration while the change of boundary layer nature produces a sharp reduction of the drag coefficient. One hints that both the VOF solution of Fekken (2004) and the present solutions feature an insufficient resolution of the boundary layer. A detailed investigation of the behavior of cylinder boundary layer was not presented by Fekken (2004) and, in the case of the present simulations, is out of the scope of this work. Present solutions and VOF solution of Fekken (2004) differ also in the value of the acceleration in the intermediate reaches. This is most visible in the case of $\rho = 0.9\rho_w$ between $T = 2.5$ and $T = 10$ (Figure 5.18) where the present solution features an approximately constant acceleration. The present solutions thus feature an articulation of surface and body forces that render virtually constant the total external force. This is not the case in the VOF solution, where the acceleration always decreases. The reasons for this difference are likely to be related to numerical issues, including the treatment of fluid-solid interactions. Differences between the VOF and present solutions are also observed when the cylinder approaches the free-surface, but only in the slower case of $\rho = 0.9\rho_w$: present solutions feature a much faster process of inversion of acceleration signal. As Basset forces may become important when the cylinder approaches the free-surface, one may speculate that fluid-particle interaction may be at the root of the observed differences. Since these differences do not occur in the (faster) $\rho = 0.6\rho_w$ case, one may also suspect that differences in the treatment of the free-surface between VOF-based and SPH techniques may be an important component. If that is the case, the faster the approach and thrust through the free-surface, the smaller the differences between both models.
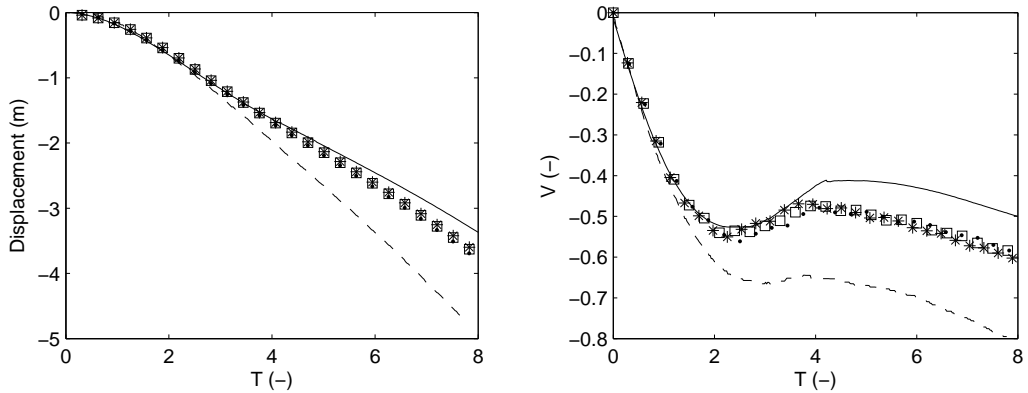
Figure 5.18 also allows to assess the sensitivity of current simulations to numerical resolution. A remarkable aspect of the presented model is that, for both cases, tripling the resolution renders very similar solutions, with slight differences only when the cylinder has already pierced the free-surface.

For a case of engulfment, a cylinder with $\rho = 1.2\rho_w$ at $D = 0$ m (half submerged) is set. Figure 5.19 shows the state of the system at four instants and Figure 5.20 plots the vertical displacement and

velocity of the cylinder.

Figure 5.19: Sinking cylinder with $\rho = 1.2\rho_w$. $T = 1.57$; $T = 3.13$; $T = 4.70$; $T = 6.27$.

Figure 5.20: Left - Displacement of cylinder; Right - Non-dimensional vertical velocity for a cylinder of $\rho = 1.2\rho_w$. Moyo & Greenhow(analytical)Moyo and Greenhow (2000)$(---)$; Fekken(VOF)Fekken (2004)$(-)$; DualSPHysics $D/Dp = 66(\bullet)$, $D/Dp = 100(*)$ and $D/Dp = 150(\square)$.

Again, one can see how the SPH results are close to the VOF solution, particularly in the initial instants. The inflections on the velocity plots are a result of kinetic energy transfer from the body to the fluid, in order to accommodate the free surface deformations that occurred. At around four time units and for $V \approx -0.5$, the trajectory of the body diverges between the VOF and SPH solutions. The more resolved tests marginally change the settling velocity on the SPH solution.
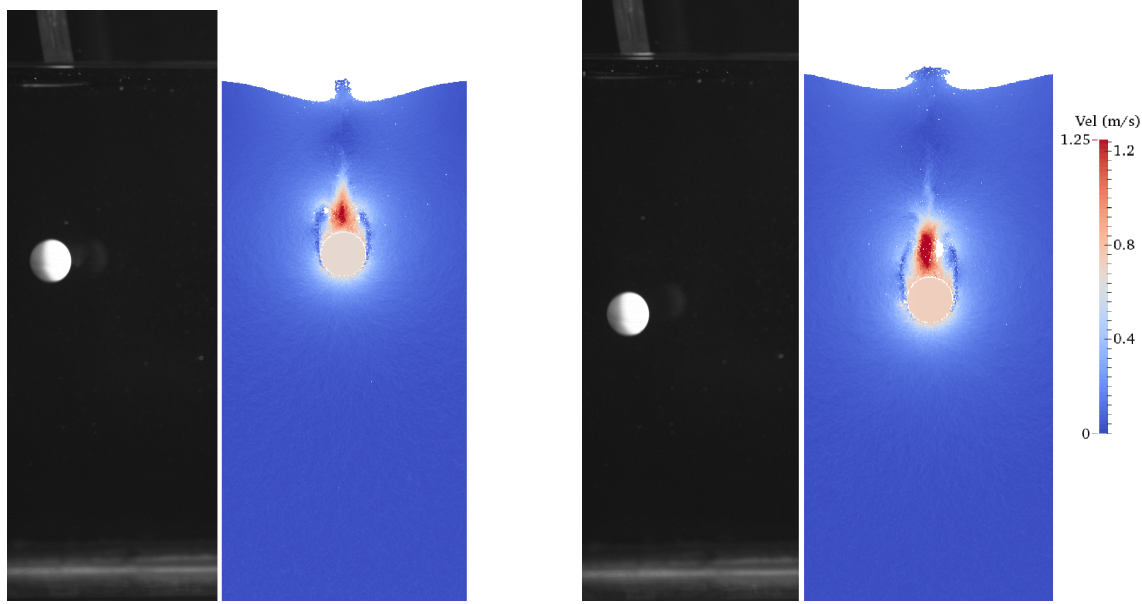
5.2.2.C Buoyancy: experimental solutions

Section 5.2.2.B introduced analytical upper limits to the velocity evolution of a buoyant sphere and data from numerical experiments from a VOF state-of-the-art solution, pointing out some differences to the SPH solution. A simple experimental procedure was designed to collect more data and provide yet another comparison point.

Measurements were performed on a glass sphere with $D = 0.012$ m, placed over a 0.20 m water column, half submerged. The sphere is kept in place by a suction device and upon its release, an 8-bit 1600×1200 px^2 CCD camera with a 500 Hz acquisition frame rate records its position until it touches the bottom of the reservoir. The experiment was repeated 3 times in order to provide a notion of repeatability of the apparatus. Three tracking algorithms were employed on each run, based on three image processing routines: edge detection, frame differencing and background subtraction.
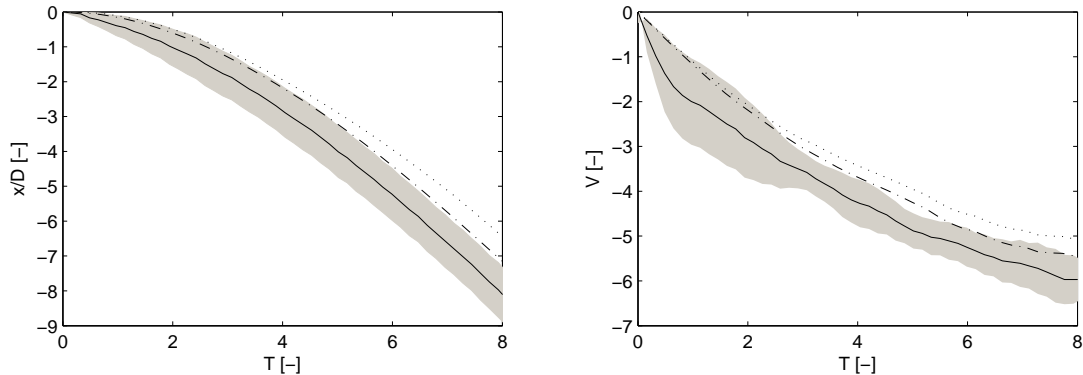
5. Validations and Tests

Three dimensional numerical solutions were performed with $5D$ periodic domain and a rigid bottom. The sphere has $\rho = 2.54\rho_w$ and two resolutions were tested, $D/Dp = 20$ and $D/Dp = 50$, resulting in over 50×10^6 particles for the more resolved case. Figure 5.21 offers a comparison between the raw experimental data and the $D/Dp = 50$ solution, plotted with the velocity field.

Figure 5.21: Sinking sphere with $\rho = 2.54\rho_w$. Experimental and DualSPHysics results. Left $T = 6.905$, right $T = 8.20$.

The clearest difference seems to be on the free surface deformation. Although some deformation occurs, the numerical solution greatly over-predicts its magnitude. It is hypothesized that missing surface tension terms in the SPH solution are responsible, since at this scale the energy associated with these deformations may be dissipated by these terms. This might be one of the reasons why a slight delay in the sphere movement is visible. As in the cases studied in the previous Section, momentum transfers from the body are required to accommodate the free surface deformation. Figure 5.22 details the evolution of the position and velocities of the sphere.
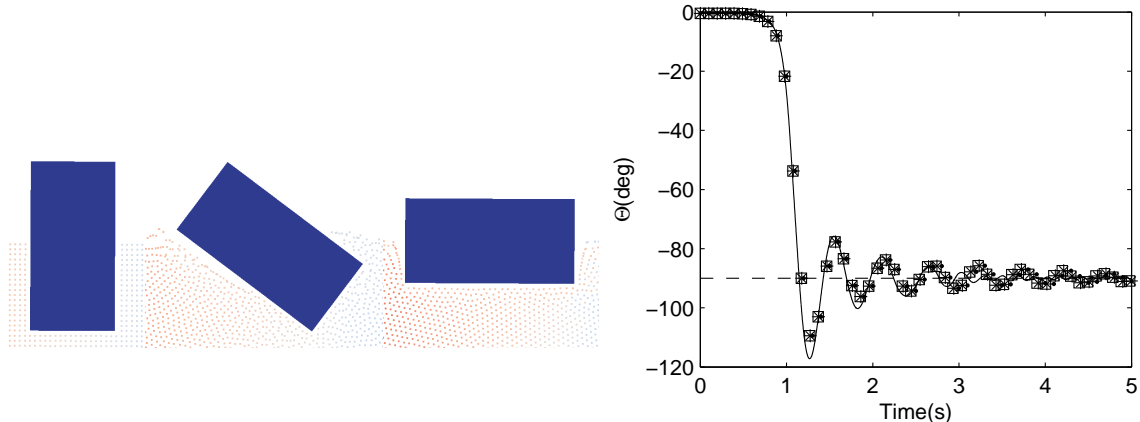

Figure 5.22: Sinking sphere with $\rho = 2.54\rho_w$. Experimental(-), experimental error region (shaded gray), DualSPHysics $D/Dp = 20$ ($\cdots$) $D/Dp = 50$ ($- \cdot -$)

One can see that the more resolved case closely follows the experimental data regarding displace-

ment and shows a good agreement in velocity. The solution seems to converge and with increasing resolution and with the multi-GPU parallelization better results are expected with higher D/Dp ratios. The periodic conditions at $5D$ distance are also not ideal and may contribute negatively to the solution. Advances on variable resolution schemes with arbitrary 3-D geometries (Vacondio et al., 2013) are also expected to allow for a much more detailed characterization of the flow structures around the object, namely the boundary layer and turbulent wake. For such detailed comparisons with small scale experiments, terms that gain relevance need to be included in the discretization, namely surface tension, as to alleviate the effects in the free surface seen in Figure 5.21.

5.2.2.D Equilibrium position of floating bodies

An important scenario is equilibrium position retrieval of floating bodies. It is demanding for a numerical discretization since the system is set in an unstable equilibrium position and is then allowed to evolve until it reaches a stable equilibrium. Fekken (2004) introduces numerical results for a 0.10×0.05 m rectangle, vertically placed in a tank, half submerged, with $\rho = 0.5\rho_w$. The 2D SPH simulations were set with $L/Dp = 15$, $L/Dp = 30$ and $L/Dp = 50$, where L is taken as the smallest side of the rectangle. Figure 5.23 shows the evolution of the system and the angle of the object with the horizontal (Θ) along time, comparing with the data from Fekken.

Figure 5.23: Left - Displacement of rectangle at $t = 0.0s$, $t = 1.1s$ and $t = 5.0s$; Right - Angle history of the rectangle. Equilibrium$(- - -)$; Fekken(VOF)Fekken (2004)$(-)$; DualSPHysics $L/Dp = 15(\bullet)$, $L/Dp = 30(*)$ and $L/Dp = 50(\square)$.

The cylinder correctly finds the stable equilibrium position, at $\Theta = -90$ degrees and the damped oscillatory rotation around that point closely matches the VOF results. The more resolved solutions show a marginally better phase matching with the VOF results. This result is particularly important since it shows that the system avoids unstable positions, correctly reproduces the dynamics of the event and is robust even with low resolution simulations. Unlike on the VOF simulations, no acceleration was imposed in the first instants of the simulation in order to force the system to diverge from the initial position: the SPH solution instabilizes by itself. This appears to be a result of the large amount of interactions involved in every time-step and the initial cubic lattice used for particle positioning. Small errors owing to machine precision and non-repeatability of the thread order of the parallel

5. Validations and Tests

implementation (Domínguez et al., 2013) causes very small numerical unbalances, that would otherwise be diffused, to be amplified by the physically unstable configuration of the system.

5.2.3 Normal Dry Collisions
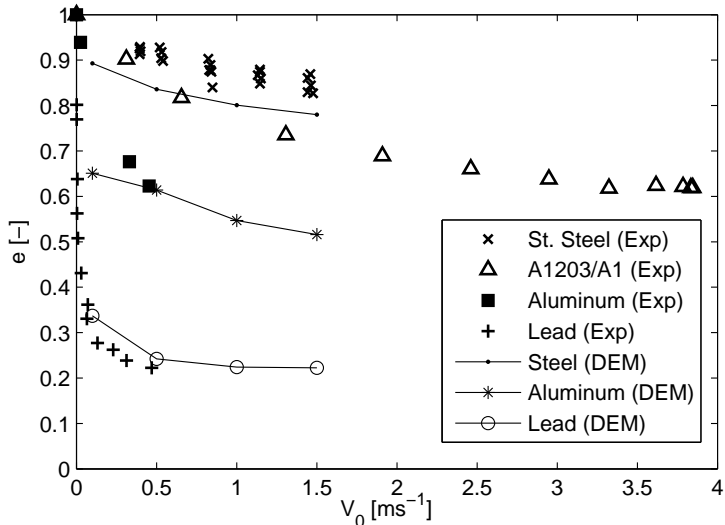
The results compiled by Kruggel-Emden et al. (2007) show the dependency of the restitution coefficient with velocity to be in line with $(1 - e_n) \sim v_n^{1/5}$. The used non-linear Hertzian model described by Equations (3.57) to (3.60) was derived in the prospect of complying with experimental data. Qualitatively, Figure 3.11 shows a dependency with the correct tendencies, but the model parameters may influence the accuracy of the force computation, depending on the materials in question. Furthermore, forces are used to update the dynamics of the rigid bodies with Equations (3.49) and (3.50), that are then integrated in time.

Data was collected using 3D simulations, where a sphere, with diameter D, hits a wall made of the same material, in the normal direction, with a given launch velocity V_0. Zero body forces imply that the only forces acting on the dynamics of the system are the normal contact forces, correctly replicating the pendulum conditions of the experimental work. Three materials are tested: steel, aluminum and lead. Table 5.1 condenses the parameters used in the simulations.

	$E\ [Nm^{-2}]$	$\nu_p\ [-]$	$e\ [-]$
Steel	200×10^9	0.30	0.85
Aluminum	65×10^9	0.33	0.75
Lead	16×10^9	0.42	0.40

Table 5.1: Young modulus, Poisson coefficient and restitution coefficient used in the simulations.

Of special notice should be the restitution coefficient, e, used to define the viscous damper coefficient in Equation (3.60). It should be understood, in the context of our non-linear model, as a tuning parameter, with a purely numerical meaning. By varying the initial velocity V_0 and measuring the velocity after the impact, e_n was measured, as given by Equation (3.53), resulting in Figure 5.24.

Figure 5.24: Restitution coefficient e as a function of initial normal velocity V_0. Experimental data (Kruggel-Emden et al., 2007) and numerical solution.

There seems to be good agreement in the range of values obtained, as well as the tendency inverse relation between e_n and the impact velocity. The results are independent from resolution, and were tested with $D/Dp = 10$, $D/Dp = 50$ and $D/Dp = 150$, with variations of less than 1% in e_n. As V_0 tends to zero, the numerical e_n does not converge so rapidly to 1 as in the experimental data. Both shortcomings in the adopted model and the difficulty of accurately measuring very small velocities in an experimental context lead to a difficult debate on the origin of the differences.

5.2.4 Experimental Validation: Dam-break with moving obstacles

The Wave Channel of the Hydraulics laboratory (LHIST) of the Civil Engineering Department at Instituto Superior Técnico, Lisbon, Portugal, was adapted to perform dam break tests. The flume was sectioned at 8.0 m long and is 0.70 m wide, with glass side walls in order to grant optical access to the flow. The flume material can be considered very smooth both in the walls and the bed. A gate was installed, as seen in Figure 5.25.

Figure 5.25: Upstream perspective of the channel and the open gate.

Together with a lock lever and a monolithic weight, the pulley system allowed for opening action that was easily repeated and provided an 'instantaneous' removal for the dam-break. The measured opening time was 0.21 s, lesser than the required theoretical limit for a dam break $t_o(h_0 = 0.40) = \sqrt{2h_0/g} \approx 0.29$ s (Lauber and Hager, 1998).

A series of PVC cubes with a $L = 0.15$ m side, filled with a material that resulted in a final density of 800 kgm^{-3}, were built. These were sealed to ensure that the content of the cubes remained dry, with regular mass measures performed during the experiments.

Three synchronized video cameras pointing from the upstream, top and downstream directions provide means to track the cubes as the flow progresses. A Direct Linear Transform (DTL) imple-

5. Validations and Tests

mentation (Capel, Fitzgibbon, Kovesi, Werner, Wexler, and Zisserman, Capel et al.) was adapted, providing inverse homography and error quantities. Since only two images are needed to estimate the objects coordinates and three are provided, the error measure is taken as the deviation from the results from the tree possible pairs. Targets are observable in Figure 5.25. These are placed on flume bed and walls at known positions, providing means for camera calibration and reference points for the reconstruction algorithm. A flash triggered with the release of the gate marked the synchronization time for the several cameras.

Several configurations of the stacked cubes were tested, as indicated in Figure 5.26.

Figure 5.26: Three cube configurations, Left - I, Center - II, Right - III

The origin of the reference system was chosen as the right bottom at the gate section. The x axis extends along the flume in the downstream direction, z axis points upward and the y axis points right.

Each configuration was measured twice in order to establish a measure of the repeatability of the experiments. With both measurements and considering that each run can be tracked with three pairs of images six virtual runs by configuration can be measured.

Using configuration I, PIV measurements were performed on the locus of the impact of the wave with the objects, allowing for a visualization of the velocity field, presented in Section 5.2.5.

5.2.4.A Configuration I

Case I presents a single cube in the center of the flume, with a face directly aligned with the flow direction. The numerical solution must be able to generate a correct equilibrium position for the cube, balancing the gravity force by producing a contact force. Initial conditions do not include contact forces, as they are computed at the expense of small displacements (DEM with soft-body approach) of the particles that make up the rigid body.
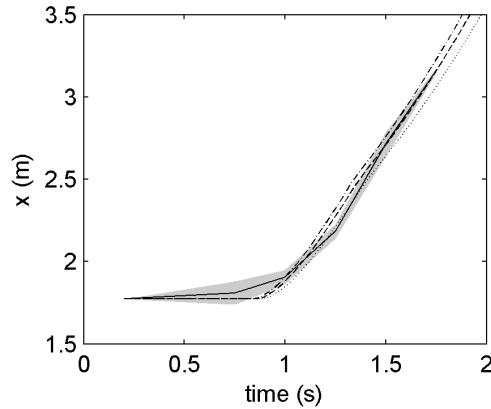
Parameters in Equations (3.57) to (3.63) were set to represent the various materials in the simulation, as described in Table 5.2.

	Material	$E\ [Nm^{-2}]$	$\nu_p\ [-]$	$e\ [-]$	$\mu_f\ [-]$
Flume bottom	Steel	200×10^9	0.30	0.85	0.35
Walls	Glass	65×10^9	0.23	0.80	0.40
Cubes	PVC	3×10^9	0.30	0.40	0.45

Table 5.2: Young modulus, Poisson coefficient, restitution coefficient and friction coefficient used in the simulations.

For all simulations the smoothing length was $h = 1.2\sqrt{3Dp^2}$, the C parameter from the stability region condition, Equation ((3.70)), was set at 0.20 for all simulations and the kinematic viscosity is that of water at $20°$ C temperature, $\nu = 10^{-6}$ m^{2}s^{-1}.

The cube positions along the longitudinal dimension from the numerical solution are plotted against the experimental measures in Figure 5.27.
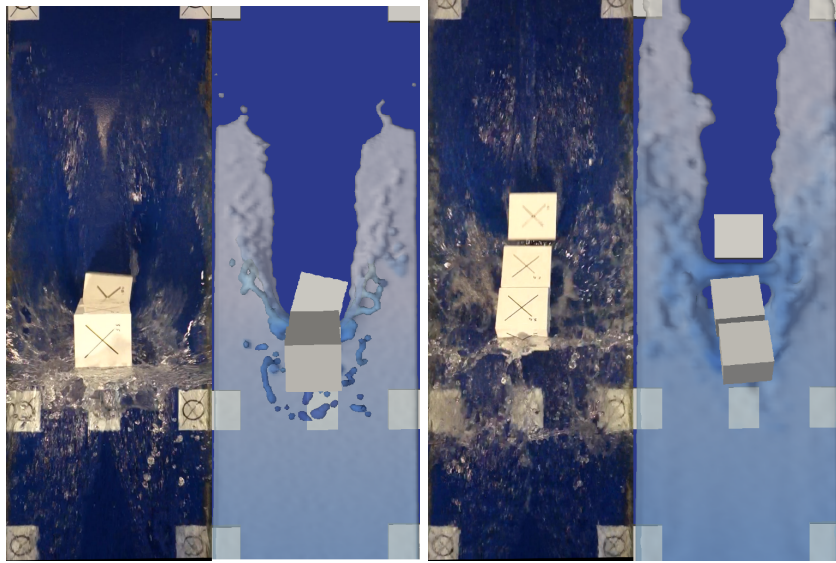

Figure 5.27: x coordinates in time. Experimental (-), DualSPHysics $L/Dp = 10(- \cdot -)$, $L/Dp = 15(--)$, $L/Dp = 45(\cdots)$.

The shadowed area represents the symmetrical error region obtained by considering the variation obtained between the two consecutive experimental runs, plus the variation between measurements in the same run. The comparison shows good agreement between experimental and numerical data, implying that both normal and frictional forces are accurately computed. The frictional mechanism seems to correctly predict the transition from static to dynamic situations, showing that the Coulomb limit is applicable. Increasing the resolution from $L/Dp = 10$ to $L/Dp = 45$ renders small variations on the results, maintaining the positive agreement with the experimental data.

5.2.4.B Configuration II
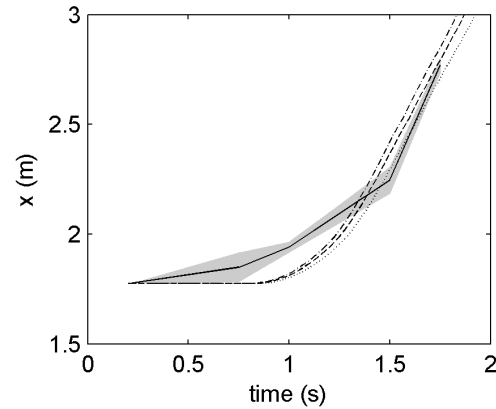
Configuration II presented three stacked cubes directly aligned with the flow direction. This configuration attests to the capability of the model to respect static equilibrium positions of stacked objects. No kinematic restrictions are applied, forces are computed dynamically but their resultant is equal to the gravity force and other forces applied. Again, initial position adjustments are minimal since the springs in Equation (3.57) are very rigid. No vibrations due to over-shoot and under-shoot cycles are detected due to the effectiveness of the viscous damping term. Figure 5.28 shows a frame from the experiment aligned with the numerical solution in the same instants. Note that for visualization convenience an isosurface derived from the SPH solution is plotted.

5. Validations and Tests
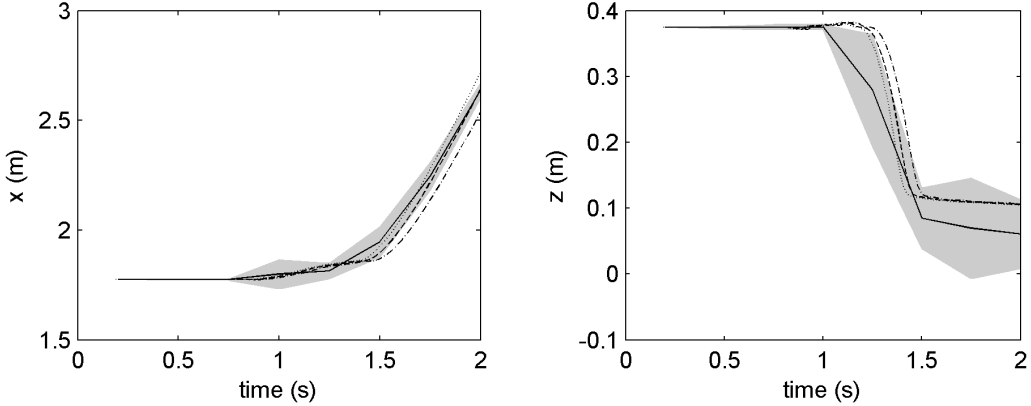
Figure 5.28: Configuration II. Experimental *vs* numerical rendering of solution. Left $t = 0.98s$, right $t = 1.28s$.

The bottom cube presents as main direction of movement the longitudinal axis, much as the cube of Configuration I, but here more complex phenomena are present. The involved forces must now also account for the weight of the top cubes, multiplying the order of magnitude of the frictional components in the beginning of the movement. Figure 5.29 shows the evolution of the cube coordinates, where once again the shadowed area represents the experimental variability.

Figure 5.29: Bottom cube. x coordinates in time. Experimental (-), DualSPHysics $L/Dp = 10(- \cdot -)$, $L/Dp = 15(--)$, $L/Dp = 45(\cdots)$.

The agreement is positive, while the initial instants of motion are not fully recovered. Frictional force on the bottom and upper faces seems to be over predicted, resulting in a delay of around $0.5s$ before static friction, given by the spring-damper mechanism (Equation (3.61)), is limited by the Coulomb force (Equation (3.63)). Once in motion, as in Configuration I, the velocity is in good agreement with the measurements, again indicating that kinematic friction is well accounted for. Increasing resolution does not improve the behavior of the initial instants. The top cube provides two characteristic motion directions, along the x and z axis, as the cube falls after the stack looses integrity. Figure 5.30 quantifies the motion along these axis.

Figure 5.30: Top cube. Left - x coordinates, Right - z coordinates. Experimental (-), DualSPHysics $L/Dp = 10(-\cdot-)$, $L/Dp = 15(--)$, $L/Dp = 45(\cdots)$.

Motion along the x axis is very well predicted, with initiation of motion, initial velocity given by the momentum imprinted by friction from the middle cube and velocity once dragging starts being well represented. A small delay in the initiation of the dragging is noticed, but a correct velocity seems to be recovered. The increased resolution seems to effectively correct the delay and further improve the final velocity. Along the z axis, the bulk of the motion is well predicted, but the initiation of the fall is delayed due to a vertical component of momentum being transferred to the cube, effectively sustaining it at the initial position for longer. Such behavior seems to be the result of high frequency oscillations in the force chain of the rigid cubes, leading to an accumulation of energy that the contact dampers are not able to dissipate. Similar phenomena were reported by Cummins and Cleary (2011), that concluded that it is a direct consequence of considering rigid bodies with no internal dissipation mechanisms.
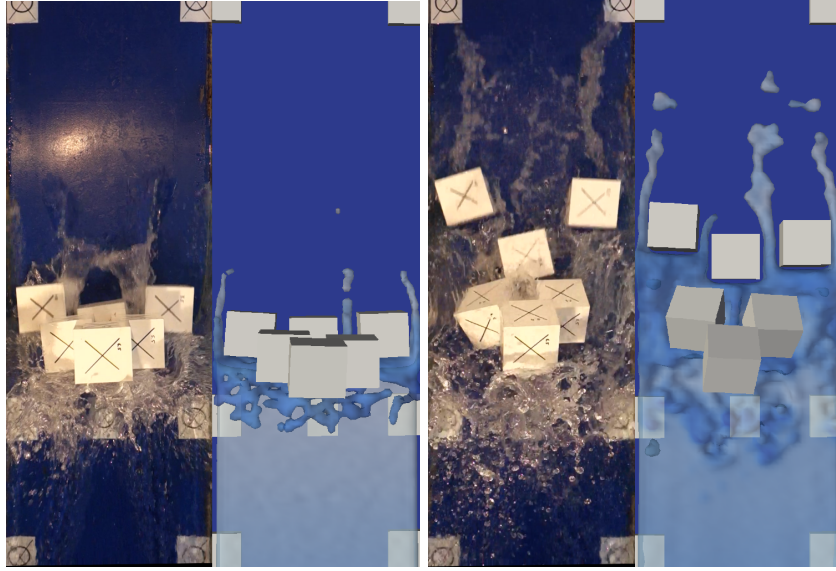
5.2.4.C Configuration III

Configuration III represents a highly complex geometry, with a pyramid of cubes forming a wide obstacle on the flume. Gaps between the cubes further complicate the case, by allowing fluid to exert forces not only frontally but also laterally, between cubes. Figure 5.31 shows two frames from the experimental runs and the equivalent numerical solutions.
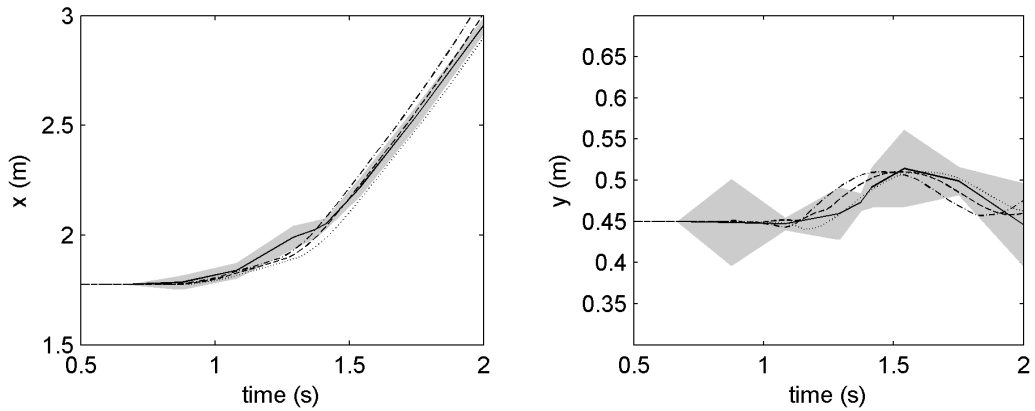
The tracked cubes consist of the uppermost cube and the top left cube (observing from the perspective in Figure 5.26). Figures 5.32 and 5.33 show the results for the latter.

The longitudinal component shows a very good agreement between experimental data and the numerical solution. Every stage of the motion along the x direction seems to be correctly characterized. The cube has two contacts from the bottom cubes and one contact from the top cube, in an asymmetric configuration. This configuration, along with the fact that the cube is not centered in the flume, justifies analyzing the motion along the y direction. One can see a deviation on y position of around 30% of the cube dimension. Such deviation seems to be recovered in the numerical solution with the correct magnitude, although out of phase in the lesser resolved cases. A good result seems to be achieved for the $L/Dp = 45$ resolution. The vertical component of the motion is characterized is Figure 5.33, showing a
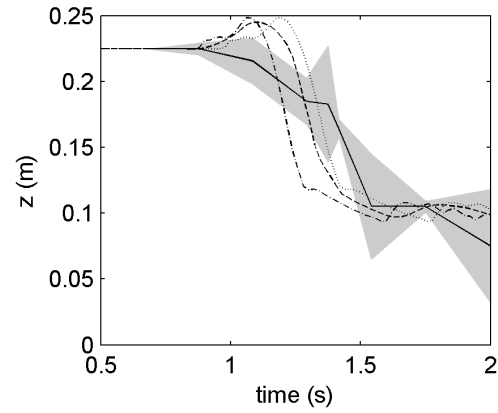
5. Validations and Tests

Figure 5.31: Configuration III. Experimental *vs* numerical rendering of solution. Left $t = 0.95s$, right $t = 1.15s$.
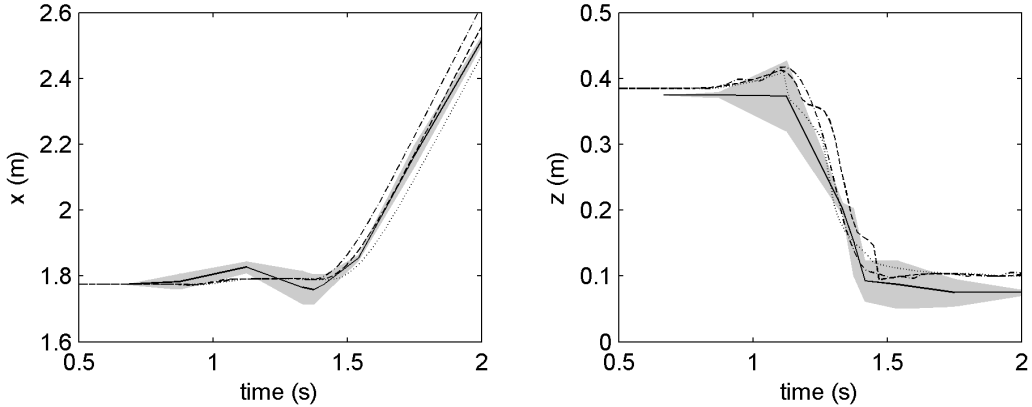
Figure 5.32: Top left cube. Left - x coordinates, Right - y coordinates. Experimental (-), DualSPHysics $L/Dp = 10(- \cdot -)$, $L/Dp = 15(--)$, $L/Dp = 45(\cdots)$.

Figure 5.33: Top left cube. z coordinates. Experimental (-), DualSPHysics $L/Dp = 15(--)$, $L/Dp = 10(- \cdot -)$, $L/Dp = 45(\cdots)$.

more sudden collapse on the numerical solution comparing to experimental data. An increase of height immediately prior to main motion, similarly to the behavior on Configuration II, is also observed.

The motion of the top cube is summarized in Figure 5.34. The results show the same trends as

Figure 5.34: Top cube. Left - X coordinates, Right - Z coordinates. Experimental (-), DualSPHysics $L/Dp = 15(--)$, $L/Dp = 10(- \cdot -)$, $L/Dp = 45(\cdots)$.

for other cubes. Both motions along the x and z directions show very good agreement, except for the defect along the z axis at motion start. The effect seems to be independent from resolution, again indicating that the rigid body concept introduces an unavoidable small error for high velocity cases with multiple large bodies and multiple contacts.
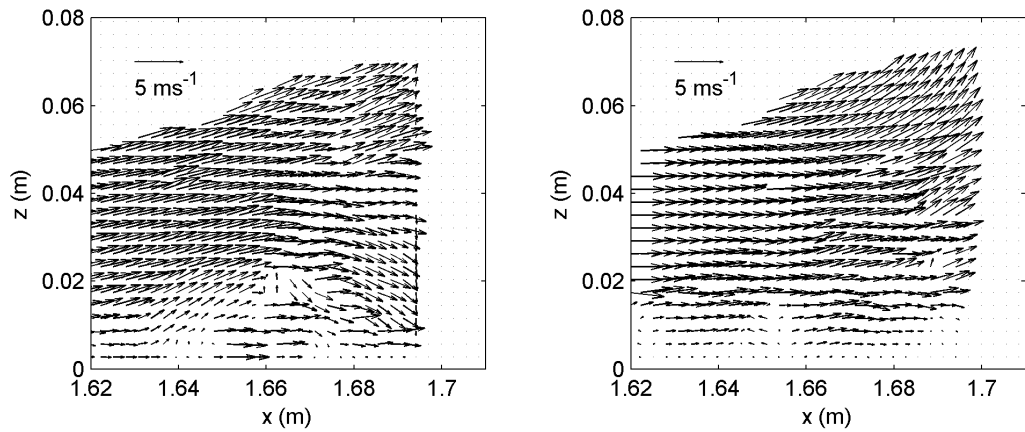
5.2.5 Flow field at impact locus

Reproducing Configuration I, a PIV setup was used to recover the flow field once the front of the dam-break wave impacts the cube. The PIV results may suffer with degraded signal since conditions are far from ideal: difficulty in homogeneous seeding due to transient nature, very unstable and discontinuous free surface, air bubbles are entrapped in the flow and may have a non-negligible velocity contribution and there is a large distance trough the flow from the laser sheet to the wall of the flume (Ferreira, 2011).

The PIV system consisted of an 8-bit 1600×1200 px^2 CCD camera and a double-cavity Nd-YAG laser with pulse energy of 30 mJ at wavelength of 532 mn. The system was operated at 15 Hz with a time delay of 1500 μs between frames. The seeding consisted of polyurethane particles with mean diameter of 60 μm in a range from 50 to 70 μm and density of 1.31 g/cm^3. At the available frequency, only one velocity field was captured, due to both movement of the object and free-surface deformation (initiation of splashes). Eight runs were completed and similar results were obtained each time, somewhat alleviating the concerns with the difficult test conditions. In order to facilitate the comparison of the flow field, SPH data from a $L/Dp = 45$ resolution was interpolated to the regular mesh produced at the output of the PIV analysis, using the same SPH kernel (Equation (3.20)) as used to solve the system, with the same parameters. Figure 5.35 details the flow fields for experimental and numerical data.

A separation point is detectable at mid-height of the flow depth in the experimental data, together with the formation of a recirculation structure near the bed. These structures are not fully formed, as their characteristic time scales are not compatible with the highly transient nature of the flow.

Figure 5.35: Flow field at the impact locus, upstream of the cube in Configuration I. $t = 0.88$ s. Left - Experimental data; Right - DualSPHysics $L/Dp = 45$

The SPH solution shows all fundamental features of the flow: a stagnation point, a reduction of the velocity in the approach of the cube (indicating increasing pressure) and the influence of the bottom boundary. A less prominent stagnation point and a lack of a bottom recirculation pattern are visible. The velocity vectors are represented with the same scale, with maximum velocities around 3.7 ms^{-1}, compatible with the Ritter solution (Stoker, 1957) of 3.035 ms^{-1} for the front of the wave.

6

Applications

Contents

6. Applications

Fulfilling the objectives of the dissertation, fringe areas (in the sense that there is hardly any numerical tool that tackled these issues without serious simplifications) are explored in this chapter. These are intrinsically preliminary results and analysis of the solutions. There are no complete set of measurements on any of these cases and, as such, validation of the solution can not be performed directly. It is the hope of the author that the model can inspire more research on this class of topics, by presenting the first available interactive sketch on them.

For the sake of completeness, simulation times are included. All of the simulations were performed on a Nvidia Titan GPU from 2013.

6.1   Coastal Geomorphology

The Portuguese coast presents high tsunami inundation risk in comparison with other locations of the Atlantic Europe due to its close location in relation to the Azores-Gibraltar plate boundary. The Portuguese coastline presents several high-energy sedimentary deposits[1] associated with onshore depositional activity from the AD 1755 Lisbon event, with both large and small boulders located above mean sea level and occurring between Lisbon and the central Algarve attributed to deposition by this and older tsunamis (Scheffers and Kelletat, 2005; Costa et al., 2008). Furthermore, the western Portuguese coast is also very exposed to Atlantic storms, and wave power associated with wind-generated waves is also very high (Oliveira et al., 2011).
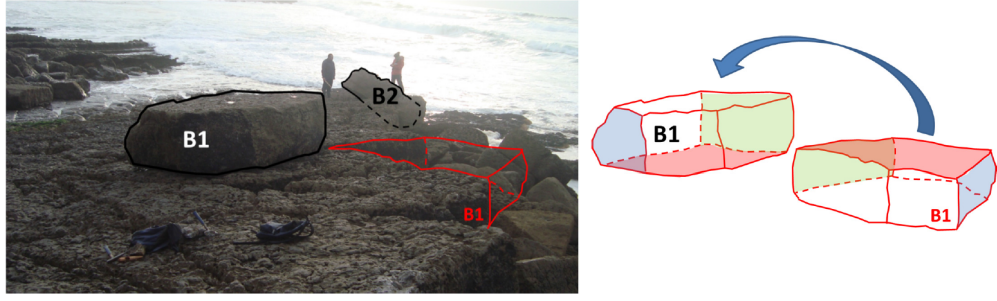
Such characteristics make the western coast of Portugal an important study area regarding entrainment and transport of large clasts (including megaclasts) by storm or tsunami waves, a matter that has been profusely discussed in the literature in the last decade. Although the exact mechanism that originates such deposits still lacks an exact comprehension, several authors used conventional numerical solutions that simulate particle transport, sometimes with contradictory results (Nandasena et al., 2011; Kain et al., 2012). The biggest challenge has been the differentiation of the events (storm or tsunami), and the reconstruction of wave parameters (e.g. wave height, length, direction) responsible for the entrainment and transport of these megaclasts. Conceptual efforts have been made to distinguish between the two, with the most popular approach being Nott and Bryant (2003) methodology, that attempts to differentiate the two origins in a variety of dynamic and geological environments, but disregarding local features.

A practical example of such phenomena can be observed in Praia das Maçãs, Portugal. The location is a pocket beach encased in a high energy exposed cliffed coast. The geology consists of Cretaceous soft marls alternated with resistant limestone. A seaward sloping close to 80 m wide stepped rock platform develops at the cliff toe. The step characteristics are controlled by practically vertical fractures and the thickness of the resistant limestone layers, typically close to 1 m. In Figure 6.1, two boulders that suffered transport are identified.

Boulder B1 is $2.80 \times 2.0 \times 1.0$ m and weighs approximately 14 ton. It appears to have suffered a rotation and a small translation from the initial position. In this exploratory Section, the proposed model is applied as an inverse-problem, attempting to reproduce the dislodgement of megaclast, i.e, it

---
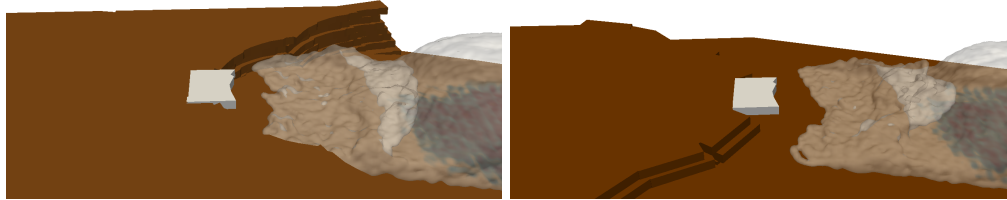
[1]Typically associated with intense wave activity, promoting resuspension and transport of larger particles.
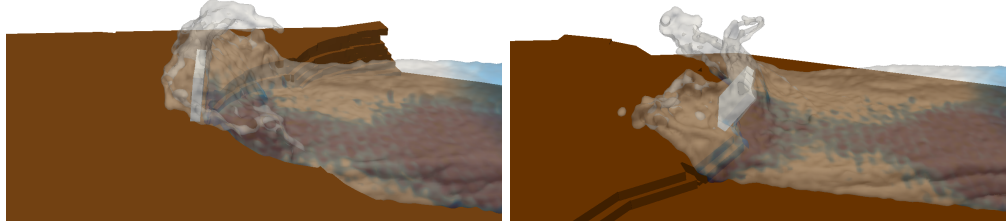
Figure 6.1: Praia das Maçãs, Portugal. Boulder identification and orientation. Oliveira et al. (2011)

is hypothesized that the pattern of deposition may be partially explained by actually modeling specific events in real geometries, attempting to recover the final observed state.

The geometry of the problem is idealized but represents the key features of the overhanging layers related with fractures, bedding and differential erosion of sub-horizontal layers that originated block B1. In plan view, concave and convex coastline shapes are tested to assess the influence of momentum accumulation. A paddle with prescribed motion was used to generate a wave with $40\ m$ wavelength and $15\ m$ height, reproducing a large storm wave that breaks at the beach section. The lateral dimension is periodic to avoid any wall effects and the 2.84×10^6 particles are a result of $Dp = 0.10\ m$ resolution, forcing 13 h long computations for 25 s events. The megaclast is assumed to be homogeneous limestone, with $E = 4.5 \times 10^8 Nm^{-2}$, $\nu = 0.15$ and $\mu = 0.60$. Figures 6.2 to 6.5 show the evolution of the system as the wave impacts the overhanging boulder.

Figure 6.2: Concave and convex geometries, $t = 10.5$ s.
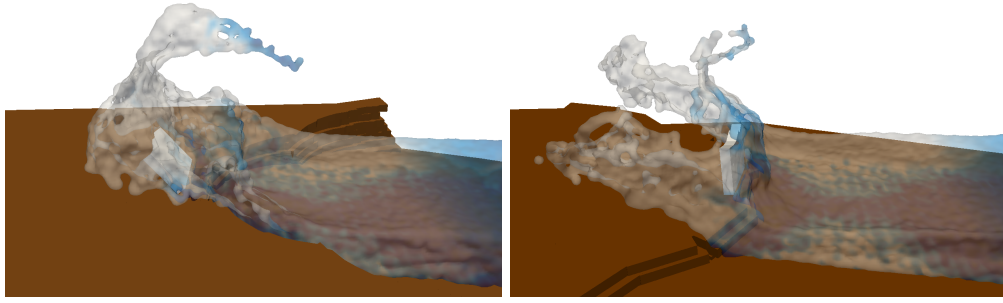
Figure 6.3: Concave and convex geometries, $t = 11.5$ s.
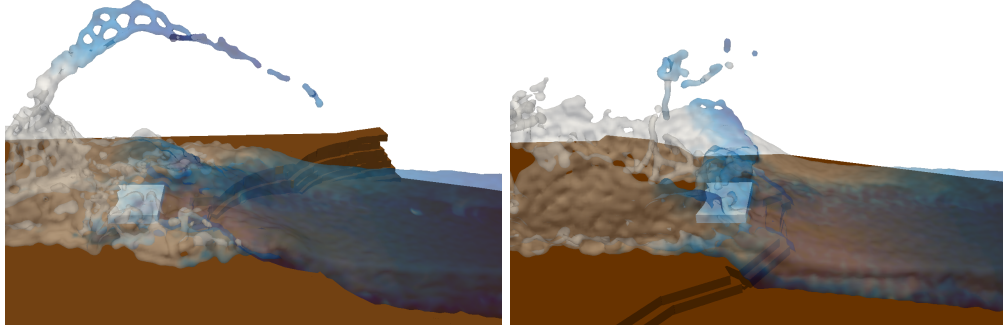
Differences in concave to convex geometries are within expectation: momentum seems to be concentrated in the concave case, as the megaclast rotates faster (Figure 6.4) and is transported around 1 m further comparing to the convex case.

Another fundamental aspect of the phenomenon is overhanging versus supported geometry. Two contact forces are responsible for the dislodgement of the boulders: pressure and momentum flux.

6. Applications
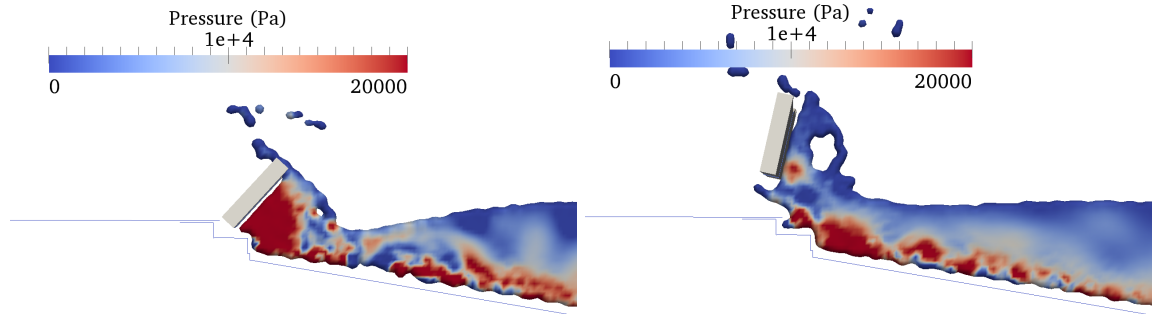
Figure 6.4: Concave and convex geometries, $t = 12.0$ s.
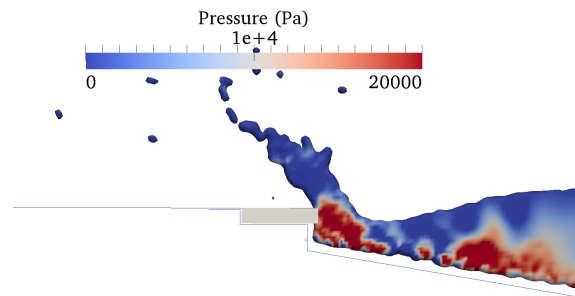
Figure 6.5: Concave and convex geometries, $t = 13.0$ s.

The main working force is the momentum flux, but the work of both for the boulder movement is proportional to the area exposed. Figures 6.6 and 6.7 show the pressure field on the impact locus.

Figure 6.6: Concave geometry. Vertical plane over domain axis. Overhanging case. Left-$t = 10.9$ s, right-$t = 11.5$ s.

Figure 6.7: Concave geometry. Vertical plane over domain axis. Supported case. $t = 11.5$ s.

As expected, a significant pressure build-up occurs in the impact locus. The cavity in the over-

hanging configuration allows the contact forces to produce work on the boulder, in contrast with the supported case.

The local (micro to meso-scale) geomorphological conditions in rocky coastal contexts strongly control the capability of waves to entrain and transport large particles upward and inland. The flow modulation induced by these features is not adequately addressed by conventional numerical solutions and requires the application of models capable of explicitly resolving the momentum transfer between phases and take into account complex geometrical considerations.

6.2 Sines Port

The Sines Container Terminal, called Terminal XXI, is a major infrastructure in the Portuguese coast, currently capable of handling 1,100,000 TEU, with plans of extending up to 1,700,000 TEU. As mentioned in Section 6.1 Portugal's Atlantic coast, especially southwards of Lisbon, is subject to a non negligible risk of tsunami waves caused by seismic events that occur offshore. These results show the influence of a wave in stacked containers and other obstacles in a reduced subsection of the quay, detailed in Figure 6.8.
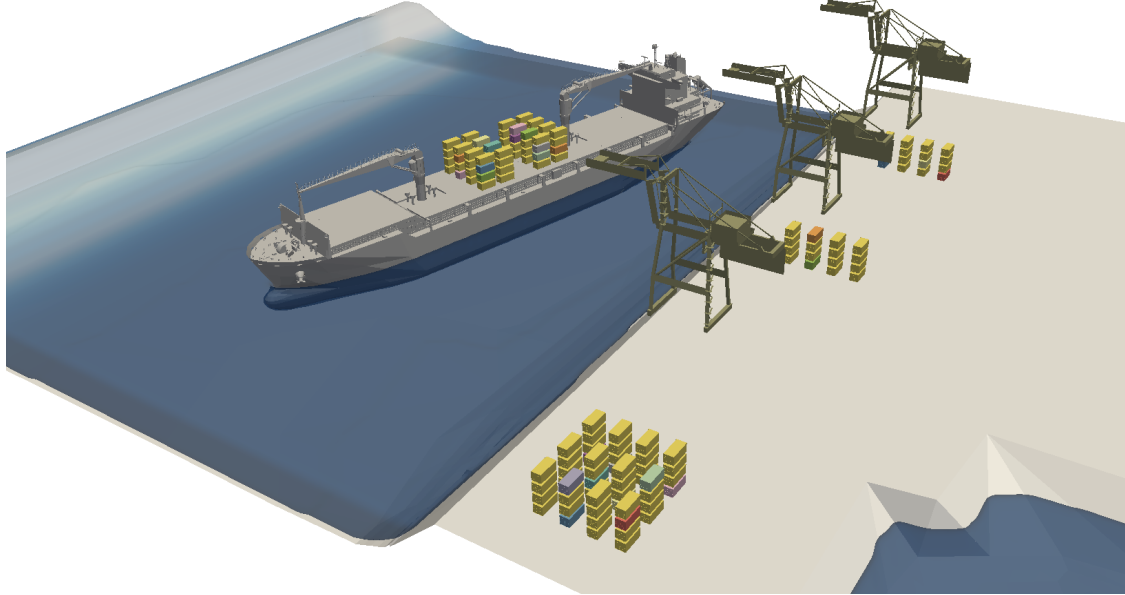
Figure 6.8: Aerial view of the Terminal XXI of the Sines Port. Red square indicates the computational domain.

The section of the harbor is partially protected by a breakwater to the east, neglected in this case to simplify the behavior of the wave on the area of interest. The chosen domain originates an excess of 12×10^6 particles, for a $Dp = 0.5$ m, resulting in a 57 h long computation for the 60 s event. The type of wave to be generated must observe some limitations, since the wavelength must be less than the domain extent, to avoid issues at the boundaries. As stated, the breakwater is disregarded, not having any influence in the simulated wave. The equations used to generate the solitary wave were (Dean and Dalrymple, 1991)

6. Applications

$$V = \sqrt{\frac{4D^3}{3H}}; \quad \eta(x') = \frac{D}{\cosh^2\left(\frac{x'}{V}\right)}; \quad v(x') = \eta(x')\sqrt{\frac{-g}{D}} \tag{6.1}$$

where D is the fluid depth, H is the maximum wave height, $\eta = D + H$ and x' is a coordinate normal to the wave axis measured from the wave apex. Propagating a wave from a synthetic tsunami generates a wave height of 15 m, corresponding, according to equations (6.1) to a top velocity of about 5.6 ms^{-1} and wavelength of approximately 130 m, against the expected several hundreds of an actual tsunami Baptista et al. (2011). The initial conditions of the system can be seen in Figure 6.9.

Figure 6.9: Initial conditions of the system.
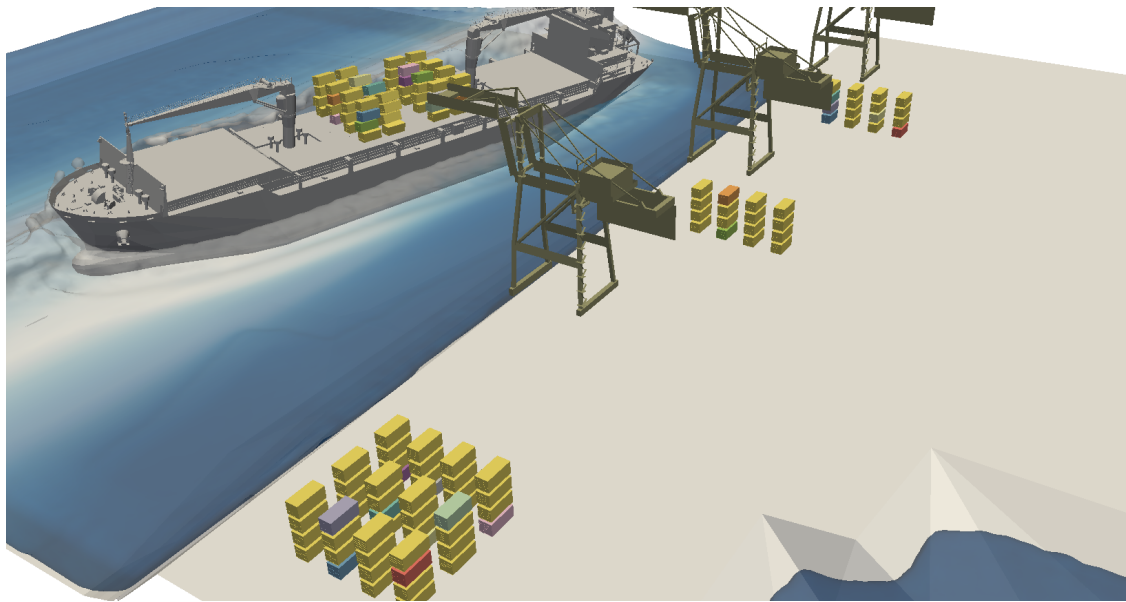
The direction of the wave is normal to the quay wall structure. A cargo ship is placed in the domain, as well as a total of 143 ship containers, 64 of which on the ship. The ship has a density of $\rho = 0.3\rho_w$ and the center of gravity was made to coincide with that of the actual ship. The geometry consists of the actual 3D scan of a ship hull, and was discretized as hollow, since no information on the internal structure of the ship is available and it would result in the most accurate inertia tensor. The ship containers are assumed half-full and as such with a $\rho = 2.5\rho_w$ density. Each individual body has 6 degrees of freedom, no restrictions are applied, and are made of steel. The gantry cranes are also made of steel but are represented as fixed boundaries and the terrain was considered limestone. Table 6.1 details the parameters used in the simulations. The CFL constant was used as $C = 0.2$, artificial viscosity with $\alpha = 0.05$ and $h = \sqrt{3Dp^2}$.

	Material	$E\ [Nm^{-2}]$	$\nu_p\ [-]$	$e\ [-]$	$\mu_f\ [-]$
Containers/Gantry cranes/Ship	Steel	200×10^9	0.30	0.85	0.55
Terrain	Limestone	4.5×10^9	0.15	0.80	0.60

Table 6.1: Young modulus, Poisson coefficient, restitution coefficient and friction coefficient used in the simulations.
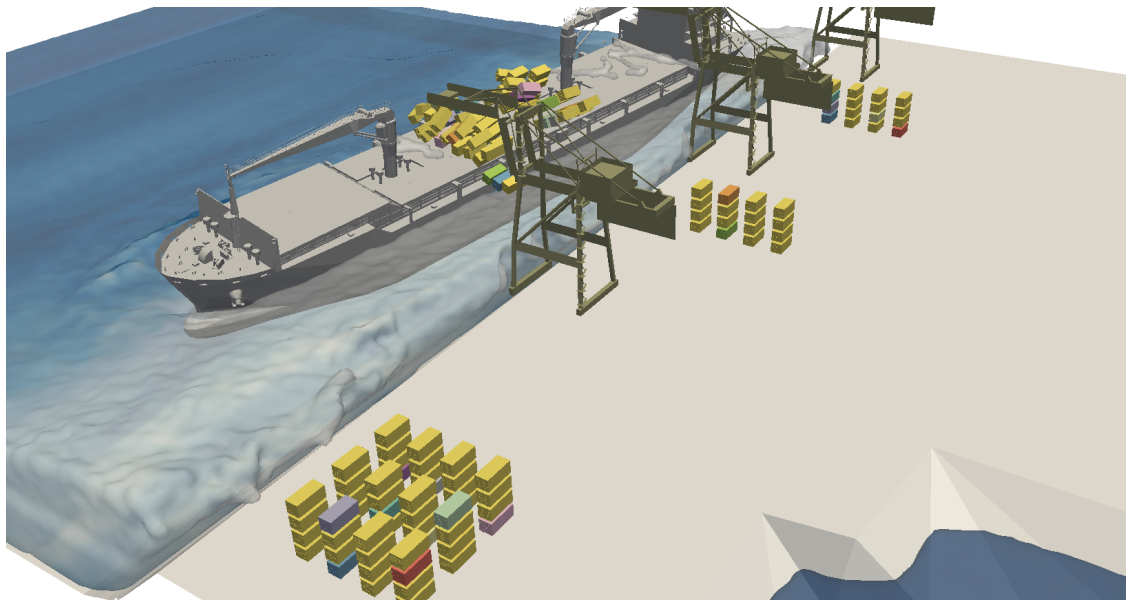
The wave travels approximately 7 s until it hits the ship. The large acceleration immediately causes the instabilization of the most forward container stacks. Figure 6.10 represents the beginning of the

ship motion and one can notice the beginning of the instabilization of the containers on the port-side.

Figure 6.10: General view of the application case, $t = 7.6$ s.
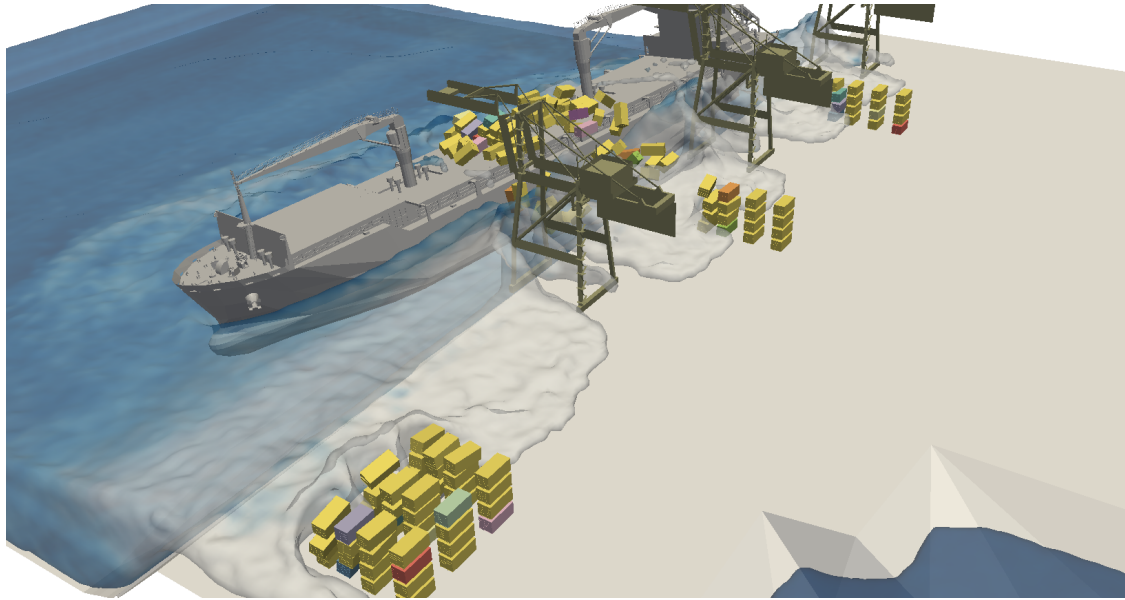
Figure 6.11, at $t = 12.0$ s, shows the container motion after the wave passage.
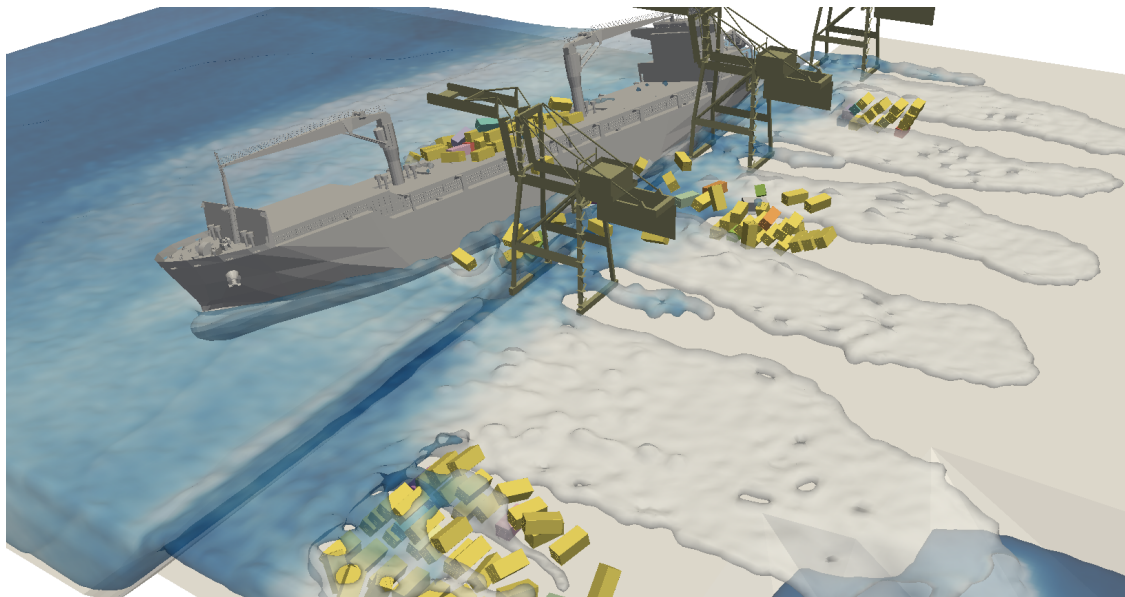
Figure 6.11: General view of the application case, $t = 12.0$ s.

Figures 6.12 and 6.13, at $t = 14.0$ s and $t = 18.0$ s, respectively, demonstrate the wave overtopping the quay and deforming at the base of the gantry cranes and the container stacks.

6. Applications
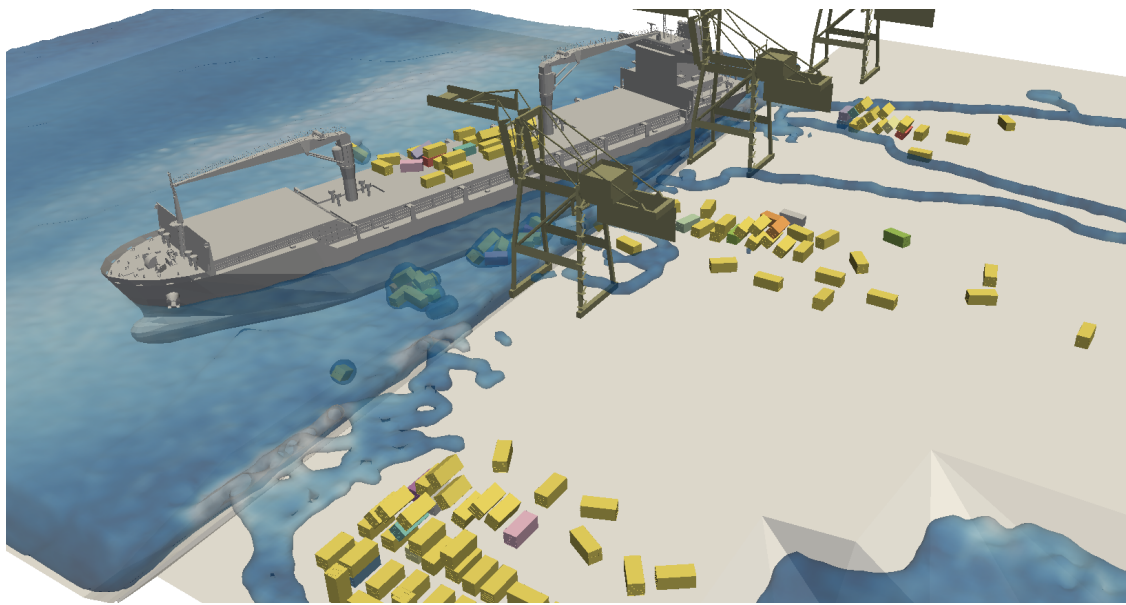
Figure 6.12: General view of the application case, $t = 14.0$ s.

Figure 6.13: General view of the application case, $t = 18.0$ s.

Instabilization of the piles is evident, with complex contact events being treated with no aberrant results. Containers initially aboard the ship are now in the water, most of them between the ship hull and the harbor structure.
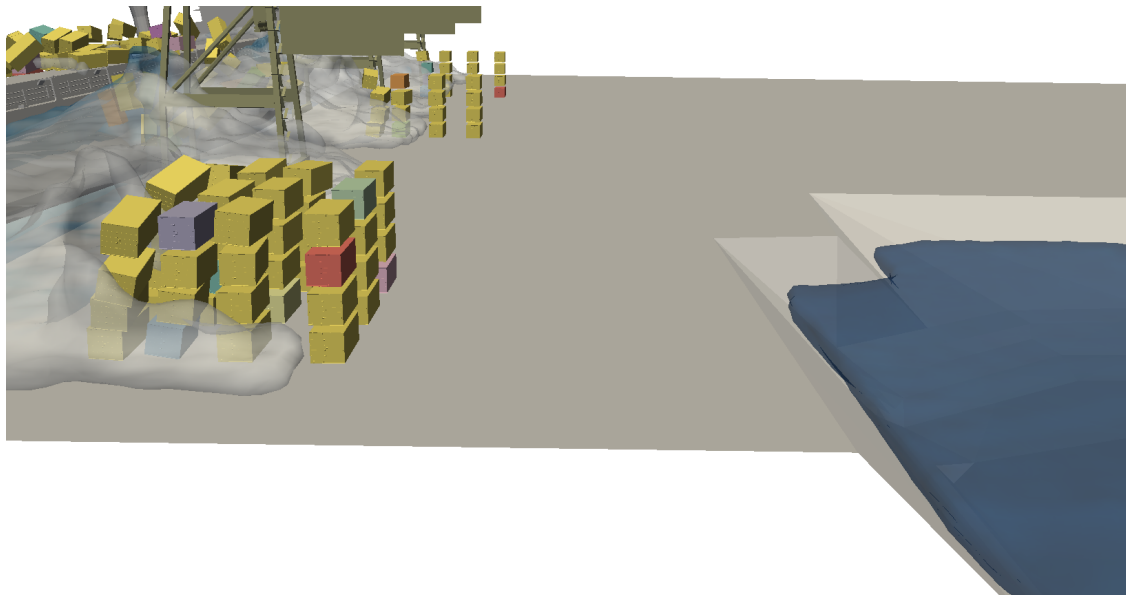
Figure 6.14, at $t = 60.0$ s, show the state of the system at the end of simulated time.

Figure 6.14: General view of the application case, $t = 60.0$ s.

Some containers were dragged a considerable length, over $100\times$ its own characteristic dimensions. Large piles of containers can be seen, formed after the initial configurations were perturbed, since the wave did not have enough momentum to transport all the containers.
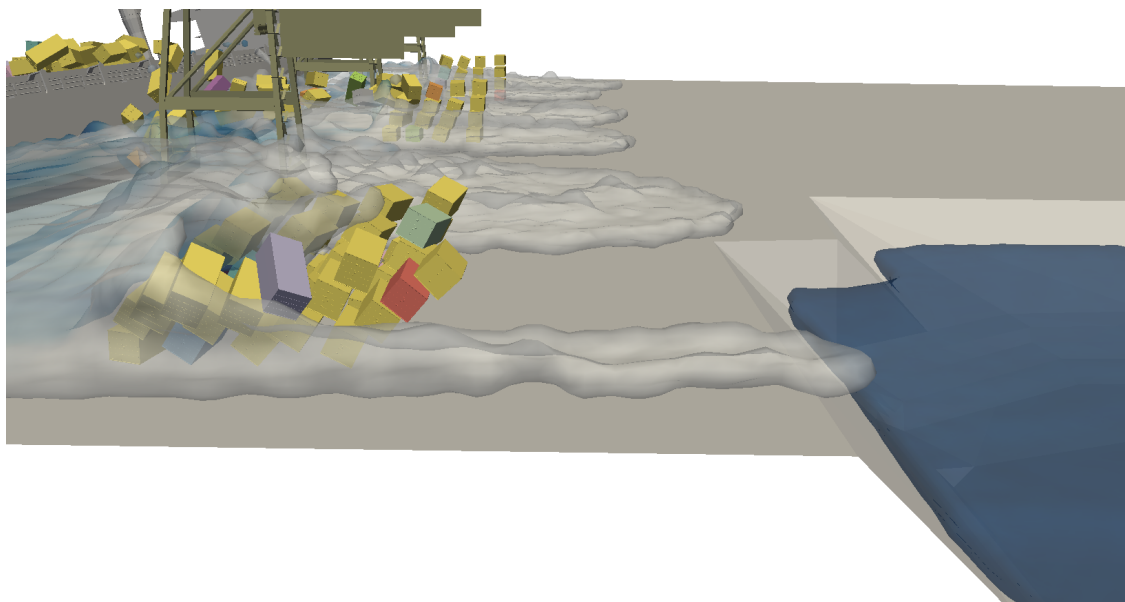
With a more detailed perspective over a set of containers, Figure 6.15, at $t = 14.0$ s, shows the instant immediately after wave impact.
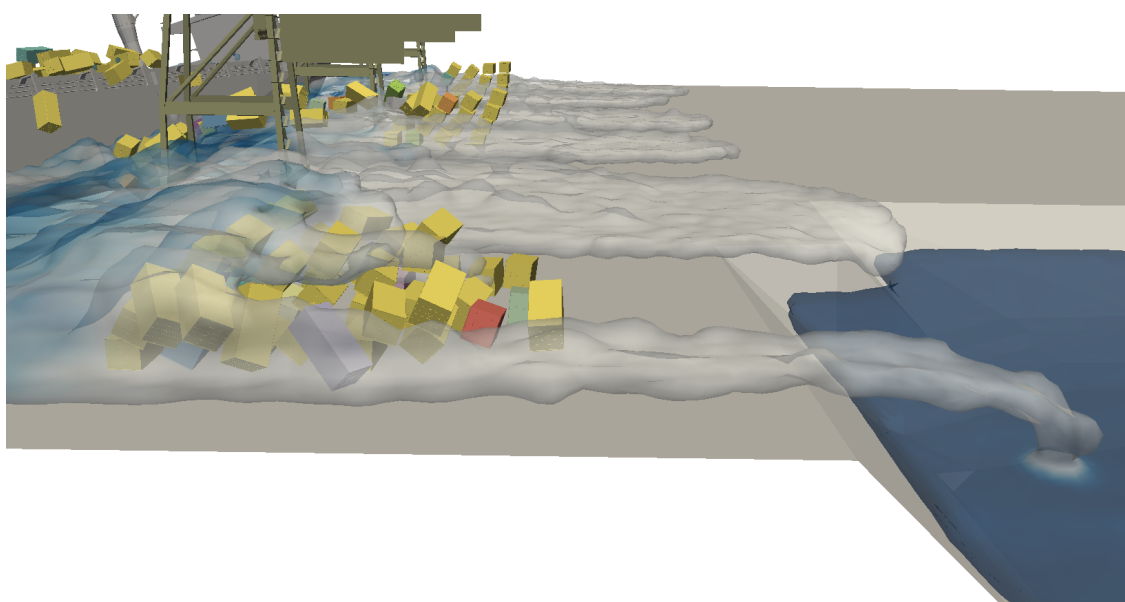
Figure 6.15: Details of a set of container stacks, $t = 14.0$ s.

Figures 6.16,6.17 and 6.18 show the collapse of the set of containers due to the impact of the wave. Little motion of the containers is due to sustained transport, most of the momentum arises from the potential energy in the vertical pile and short contact forces due to the collisions.
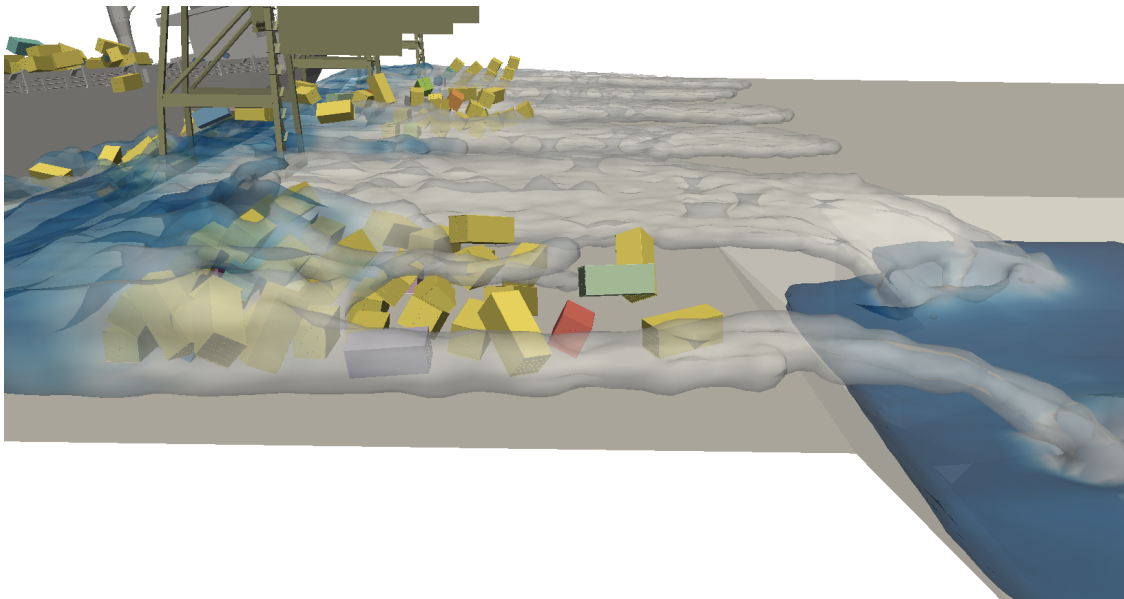
Figure 6.16: Details of a set of container stacks, $t = 16.0$ s.
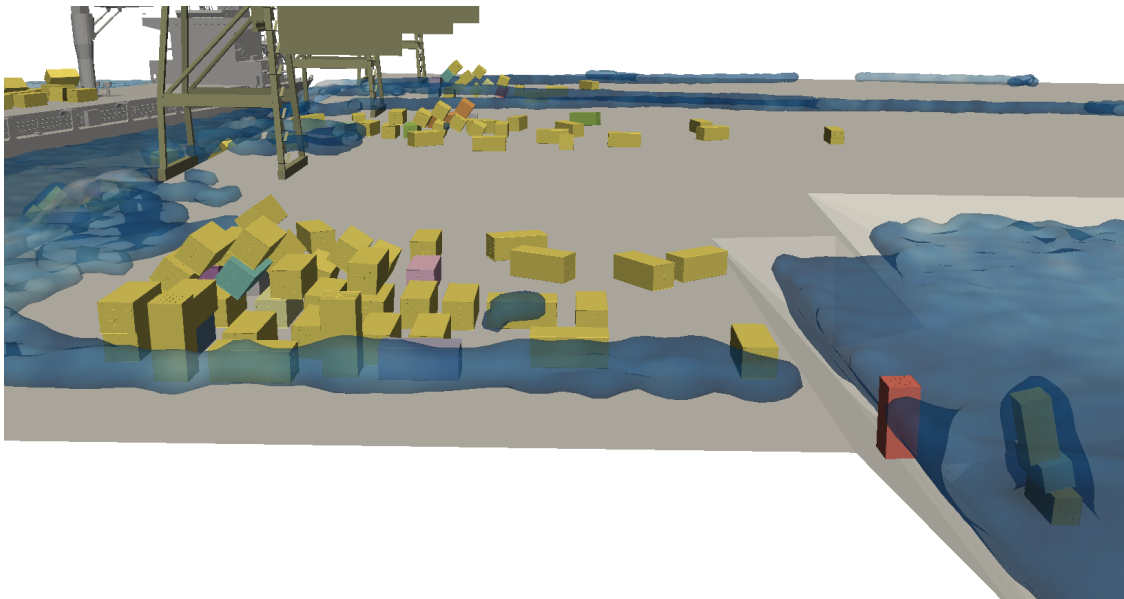
Figure 6.17: Details of a set of container stacks, $t = 17.0$ s.

Figure 6.18: Details of a set of container stacks, $t = 18.0$ s.

At $t = 60.0$ s, Figure 6.19 shows the final set of the numerical solution.
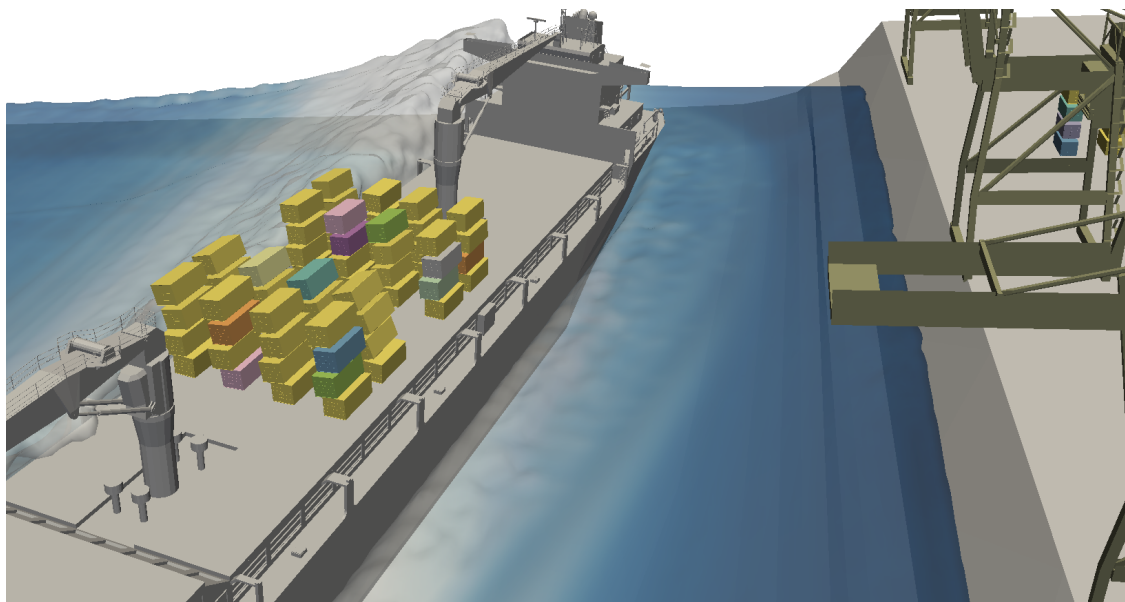
Figure 6.19: Details of a set of container stacks, $t = 60.0$ s.
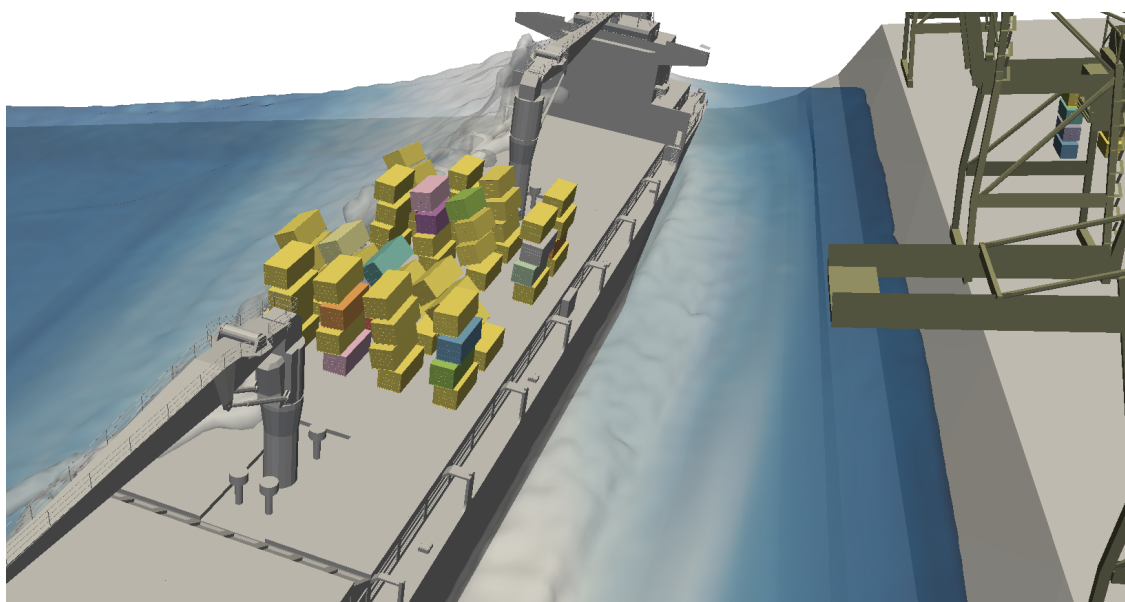
Some containers were projected across the structure platform but most did not incur in a significant dislocation. New equilibrium positions were achieved by the group of containers, showing the effectiveness of the contact mechanisms to provide balanced solutions even in complex configurations.

Focusing on the behavior of the ship containers aboard the ship, Figures 6.20 and 6.21 show the beginning of the instabilization as the wave passes, at $t = 7.6$ s and $t = 9.0$ s, respectively.
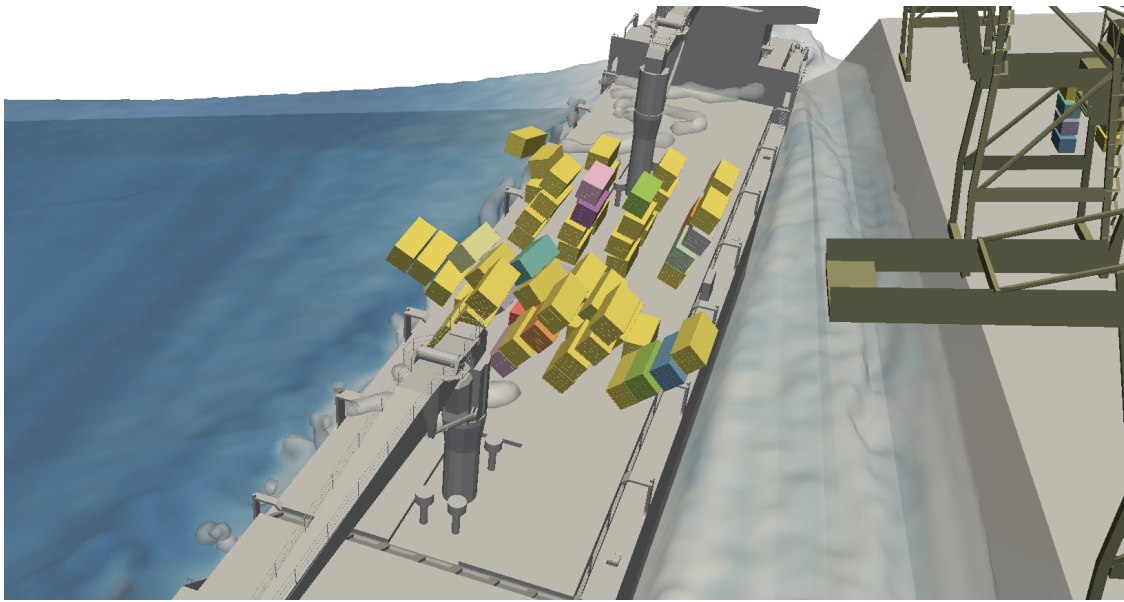
Figure 6.20: Behavior of the ship-containers system, $t = 7.6$ s.
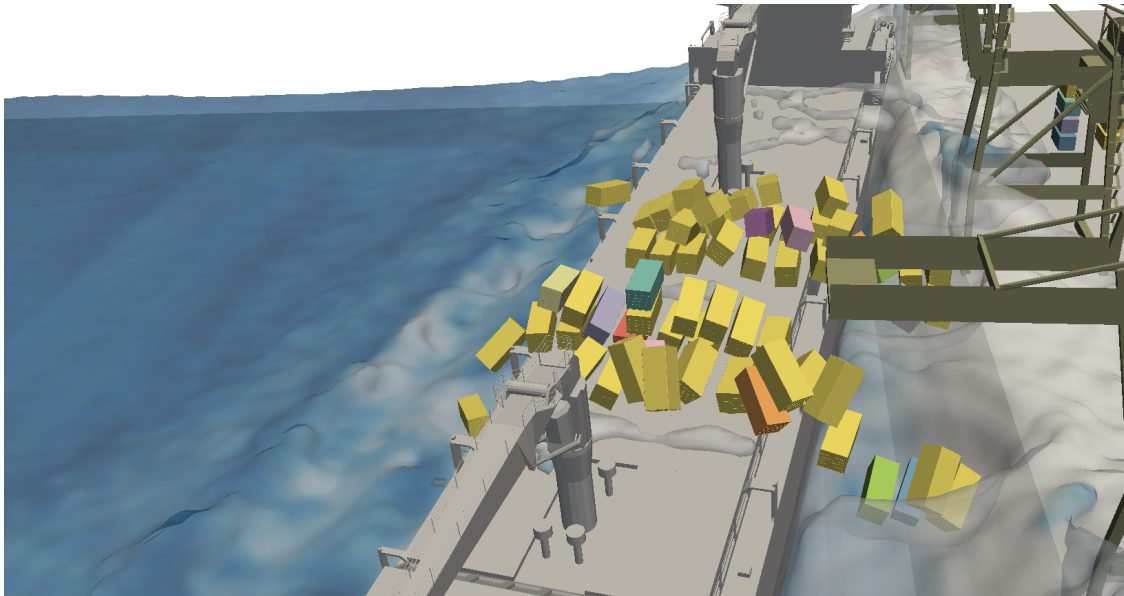
Figure 6.21: Behavior of the ship-containers system, $t = 9.0$ s.

Figure 6.22 reflects the state of the system at $t = 11.0$ s, were every set of containers is now in significant motion.

Figure 6.22: Behavior of the ship-containers system, $t = 11.0$ s.
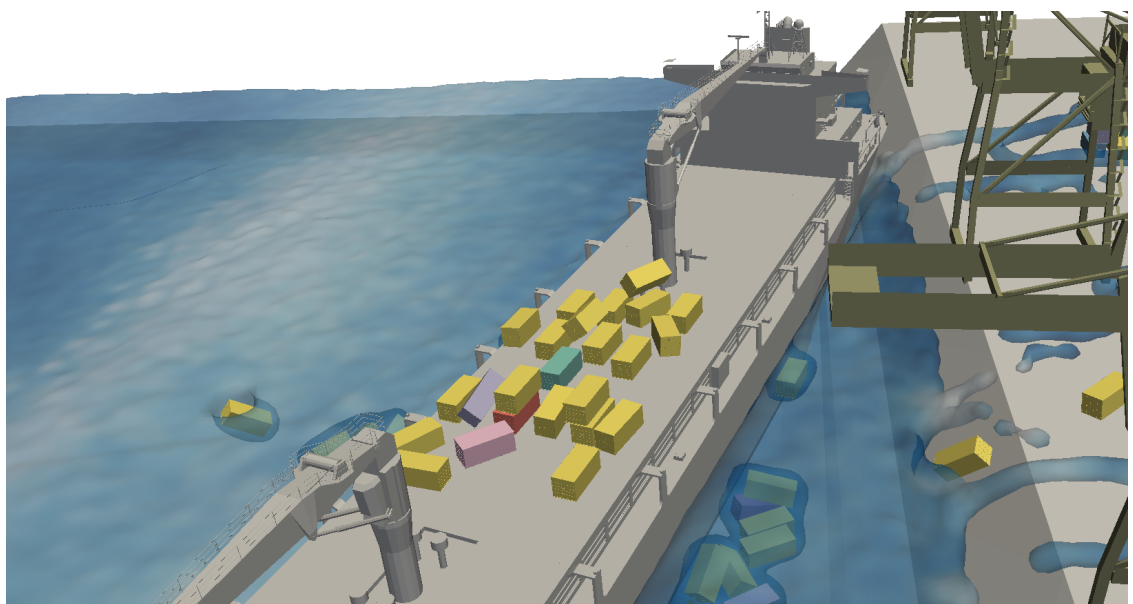
The uppermost containers are falling over the ship starboard-side, mostly due to inertia. The bottom containers, after being imprinted with the ship velocity by the friction mechanism, start sliding and falling port-side, as can be seen in Figure 6.23. Such is due to the sudden acceleration of the ship caused by collision with the bottom and padding by the wave, now mostly between the ship and the harbor structure.

Figure 6.23: Behavior of the ship-containers system, $t = 13.0$ s.

At the end of the simulation a considerable number of containers were transferred inland and a small amount fell overboard and are now in the fluid. The remaining containers have a solitary motion with the ship, as can be seen in Figure 6.24, at $t = 60.0$ s.

Figure 6.24: Behavior of the ship-containers system, $t = 60.0$ s.

6.3   Debris Flow
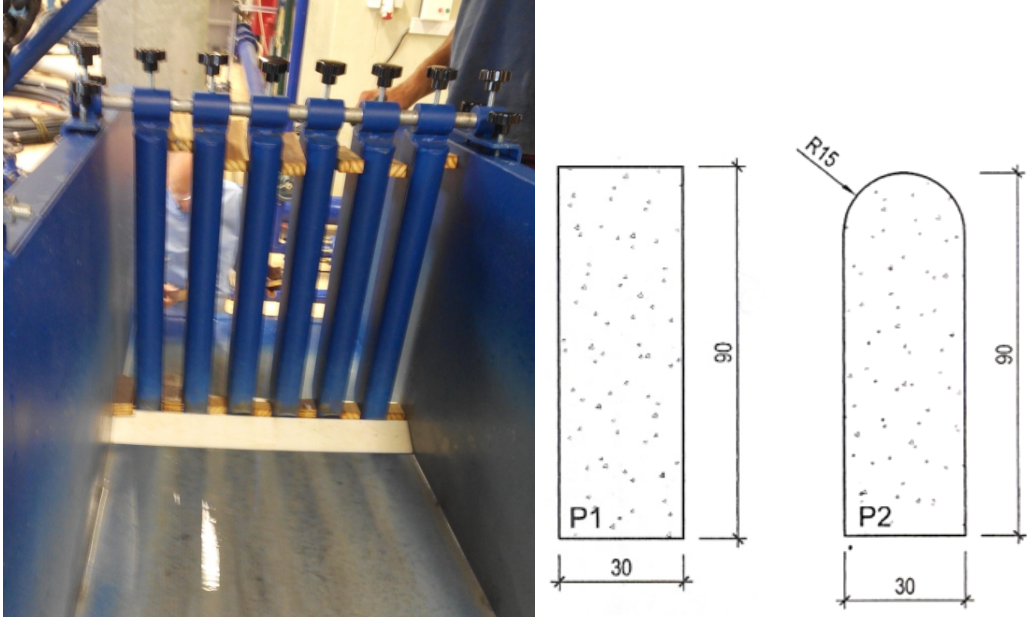
Debris flows are regarded as one of the most feared flow-related phenomena, due to the large destructive potential of infrastructure and danger to human lives. It is no surprise that a large body of work has been produced concerning its genesis, behavior and mitigation measures, both by fundamental phenomenological approaches reduced to analytic or simplified numerical problems and experimental campaigns. The flow characteristics ensure that complex measurements on important quantities remain difficult to perform. The inwards of a debris flow has only been accessible by analogy with simpler flows and conceptual work. Hope is therefore deposited in numerical work, to provide increasingly plausible insights into the mechanics of the flow. The amount of data amassed does not meet a reliable numerical solution, however. Existing conceptual models map poorly to a satisfactory numerical solution: the span of spacial scales involved in these flows start at the smaller energy carrying flow structures, up to the largest particles in the flow, possibly in the order of meters; the time scales range from millisecond inter-particle collisions to the duration of the flow; large deformations on the non-continuous multiphasic medium difficult any traditional approximation and the highly unsteady flow and free-surface deformations pose a challenge for state-of-the-art Finite-Volume codes, considering just single phase flows.

The application of the proposed model to a debris flow is done by reproducing an experimental campaign where debris flow mitigation measures are studied. A flume is fitted with a check-dam, intended to control the transport and deposition processes of the sediments carried downstream by debris flows. Since check-dams are considered as one of the simplest and most effective engineering measures against debris flows (Zeng et al., 2008; Remaitre et al., 2008) they were widely applied all over the world as a short-term mitigation measure. Check dams are composed of a weir, two wings and a robust foundation, although there is a variety of other check dam solutions. Open-type check dams present a very attractive characteristic: they allow small sediment particles to pass through, while trapping larger blocks. The implemented open-type check dam is a slit dam, whose effectiveness in debris flows mitigation has been documented in the literature.

The simulations are based on a flume described in Silva et al. (2015), where vertical slits with a spacing s, a 20% slope and a recirculating mechanism are the main characteristics. The numerical flume presents fully periodic conditions, allowing for both fluid and solid phase recirculation. Two slit typologies were tested, named P1 and P2, as defined in Silva et al. (2015). Three spacings were tested, $s/d95 \in [1.18; 1.36; 1.49]$, as per the experiments. Figure 6.25 shows the dam section apparatus and defines the cross section of slits P1 and P2.

The scales of the sediment grain interactions are orders of magnitude inferior to the $d50$ of the granulometric curve. This may represent a problem for the numerical discretization, as even smaller distances need to be evaluated for the force computations (Equation (3.54)), and machine precision can start to affect the computations after a large number of iterations. In order to curb such effect, the geometric scale of the numerical experiment was doubled, as

6. Applications

Figure 6.25: Experimental dam configuration. Slits P1 and P2 specifications. (Silva et al., 2015)

$$\lambda_l = \frac{L_m}{L_p} = 2 \tag{6.2}$$

where λ_l is the geometrical scale, L_m is the characteristic length of the model and L_p the same length on the physical prototype. Assuming Froude similarity, the discharge scales as

$$\lambda_Q = \frac{\lambda_V}{\lambda_t} = \frac{\lambda_l^3}{\lambda_l^{1/2}} = \lambda_l^{5/2} \tag{6.3}$$

It is considered that liquid and solid discharges introduced upstream are independent, i.e., it is not intended that the solid discharge corresponds to the capacity discharge for the given liquid discharge, considering the inclination, geometry and roughness of the flume. Table 6.2 shows the used model discharges and the corresponding prototype values.

	Prototype	Model
$Q_l(m^3 s^{-1})$	0.018	0.1018
$Q_s(m^3 s^{-1})$	0.00033	0.0018

Table 6.2: Model and prototype discharges
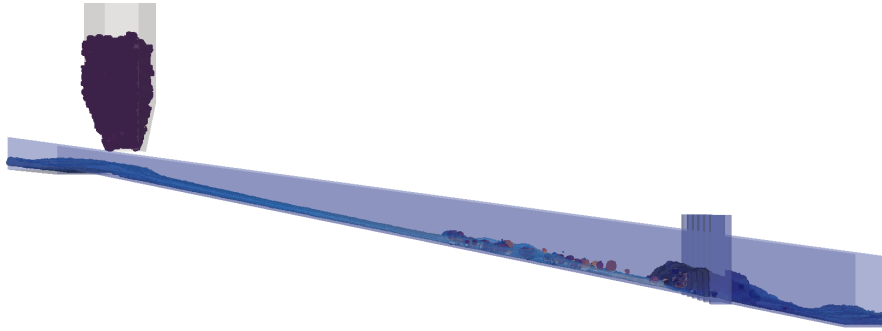
To promote a correct inlet of solid material, a hopper is modeled, placed on top of the channel. It was heuristically dimensioned to ensure an average solid discharge compatible with the one presented in Table 6.2. Solid sediment grain sizes are generated according to a random algorithm that reproduces a log-normal function, effectively approximating the granulometric curve from Silva et al. (2015). The grains are dispersed in the hopper and are let to achieve their natural equilibrium positions at the start of the simulation. The initial conditions generation routines allows to create entirely distinct solutions based on the same granulometric curves, hence with comparable statistical properties, effectively corresponding to different experimental runs.

The proposed parameters for the material properties, used in Equations (3.54) to (3.61), are summarized in Table 6.3.

$E(GNm^{-2})$	45
$\nu(-)$	0.35
$\mu(-)$	0.35

Table 6.3: Sediment mechanical characteristics

The resolution of the model was set at $0.008\ m$, resulting in over 1.6×10^6 particles. 8 parallel simulations were carried out at a time on a Nvidia K20x cluster, each taking in excess of 280 h to model the 70 s runs, due to the very demanding stability constraints on time step. An overview of the domain can be seen in Figure 6.26.

Figure 6.26: Overall domain configuration.

The sediment trapping efficiency is accounted by measuring the solid discharges at a position sufficiently upstream and immediately downstream of the dam. The experimental procedure estimated these by measuring the volumes of the sediment that was trapped downstream of the dam and by knowing the volume placed at the inlet. Due to the recirculation of solid particles, for the analysis of the numerical solution such approach is impractical, and discharges are computed directly by analyzing the flux of solid particles crossing a given plane.
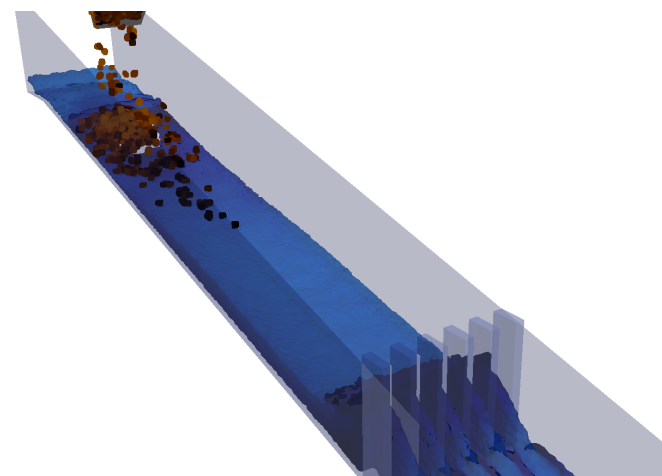
Immediately after the opening of the hopper, a substantial amount of material falls to the flume, as indicated in Figure 6.27, at $t = 3.0$ s.

As the material is carried downstream, deposition starts at the dam section. Figure 6.28 shows in detail a render of the solution in the dam area, at $t = 8.0$ s.
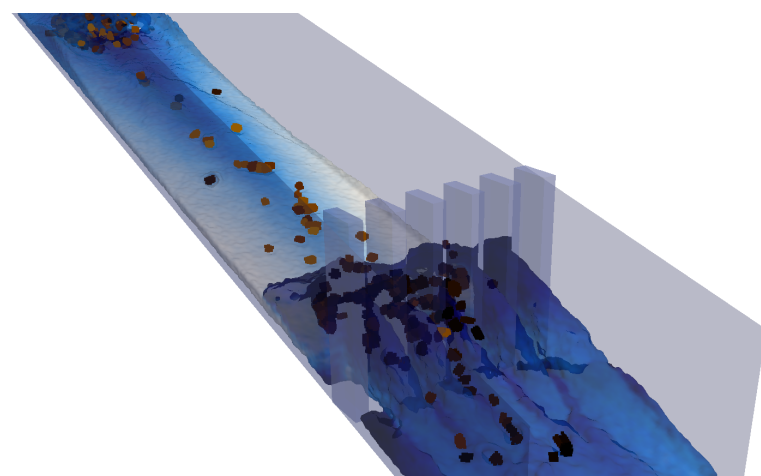
As the material is dispensed from the hopper, the retention upstream of the dam becomes more effective. At $t = 35.0$ s, the state of the solution is represented in Figure 6.29.

Figures 6.27 to 6.29 are rendered from a particular simulation. As the sediment particles are generated with a random arrangement as initial conditions, significant instantaneous variations occur if one compares similar runs. On average, at $t = 40.0$ s the hopper is exhausted and the flow is assumed to reach equilibrium conditions close to 10 s after that, when the last solid particle reaches the backwater of the dam. A 15 s interval was used to count solid discharges and derive retention trapping rates. Table 6.4 and Figure 6.30 show the relationship between sediment trapping efficiency, E, and the relative spacing $s/d95$ for each tested solution.
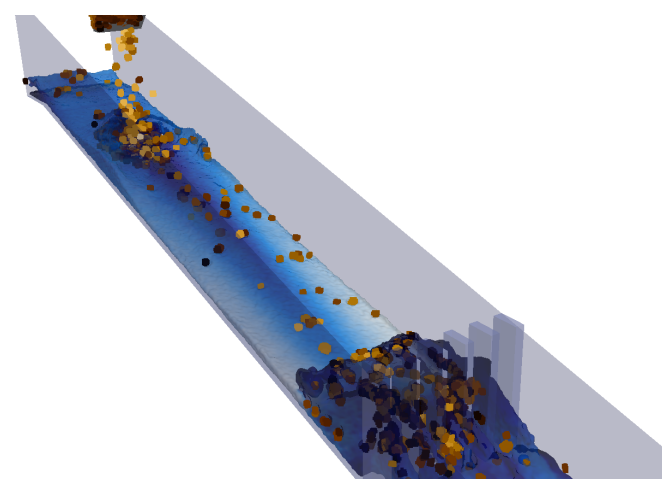
6. Applications

Figure 6.27: P1 type slits, $t = 3.0$ s
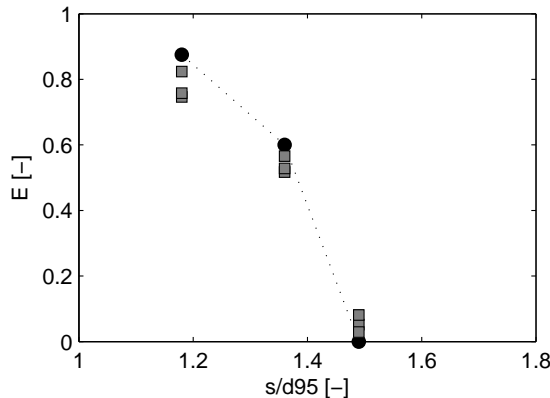
Figure 6.28: P1 type slits, $t = 8.0$ s

Figure 6.29: P1 type slits, $t = 35.0$ s

$s/d95$	E[-] (Exp)	E[-] (Run I)	E[-] (Run II)	E[-] (Run III)
1.180	0.900	0.786	0.802	0.810

Table 6.4: Sediment trapping efficiency results. P1 type slits.

Figure 6.30: Sediment trapping efficiency results. P2 type slits. Experimental ($\cdot$) Numerical ($\square$)
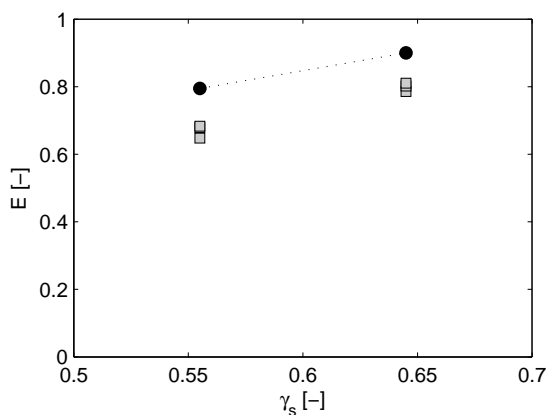
The numerical results present a good comparison with the experimental data. A noticeable under prediction of the efficiency for small spacings is shown, for both slit geometries. For P2 slits the trend is accompanied with increasing spacing, but no zero efficiency is established for $s/d95 = 1.49$, contrasting with the experimental results. This is due to single sediment particles getting retained for long enough to affect the measurements on the numerical solution.

The differences should be explained both by discretization shortcomings and differences in the initial conditions from the experimental to numerical experiments. Besides conceptual considerations, the doubling of the geometrical dimensions to allow for more relaxed length and time scales is bound to introduce differences in the flow depth in the locus of the dam. This is because Froude similarity is not an exact hypothesis in the vicinity of the slits. This may affect the retention properties of the numerical dam, but insufficient experimental data is available to provide more insight. Another important difference is related to the initial conditions of the experimental procedure. These are not marked by a smooth, fixed bed: an approximately 5 *cm* thick layer of sediment is deposited along the flume, also contributing to the total amount of mobile solid material if the flow is capable of mobilizing it, besides introducing considerable resistance to the flow.

The slit density, γ_s, is given by the ratio between the sum of all functional openings and the dam width, that influences water and solid discharges. Figure 6.31 shows the sediment trapping rate E versus the slit density.

An increase in slit density appears to induce increased efficiency of the solution, enhancing deposition upstream of the slit-dam. This is in line with the findings of Wenbing (2006). For the same discharge, the average flow velocity decreases and the local stream power decreases too, resulting in the local reduction of sediment transport capacity. This effect seems to be captured in the numerical solution, albeit with the already discussed differences.

Figure 6.31: Sediment trapping rate as a function of slit density. P1 type slits for $s/d95 = 1.18$. Experimental (·) Numerical (□)

7

Conclusions and Recommendations

7. Conclusions and Recommendations

7.1 Conclusions

The present work introduces a framework where fluid-solid flow are treated with a minimum number of *ad-hoc* formulas, where cases with arbitrarily complex geometry are supported and where very unsteady behavior presents little difficulty for the numerical approach.

To fulfill this general objective, a Lagrangian description, coupled with the meshless description of the SPH and DEM methods is adopted. A conceptual description of both the fluid phase and the contact mechanics problems is introduced and discussed. The conservation equations, closures and contact laws are subjected to the discretization, and a set of algebraic equations representing the original Partial Differential Equations (PDE) system is derived, together with a numerical strategy for solution and time integration. Several numerical solutions are compared to known solutions, recovered from either analytical studies or experimental measurements. The model is applied to actual problems, at large scales, compiling completely novel data. This corresponds to scenarios that either by scale or nature of the flow, present difficulties in direct observation and recording, fully complying with the objectives of the dissertation.

Careful derivation of the basic properties of the numerical approximation were introduced, with a discussion on predictable sources of errors and accuracy. The fluid and solid models are made compatible by using a dual SPH-DCDEM description: both fluid and solid are presented by the same numerical element, a dual entity, described as both a interpolation node and a material particle.

Solid, rigid bodies are described by a collection of particles with special properties, as fixed relative positions and a dual nature (both SPH and DEM). Since this subset of particles can take any configuration desirable, the accuracy to which a real volume is described depends strongly on the resolution. On the other hand, solid volumes, shells or any other combination of the two is trivial to reproduce with a particulate description. After the initial approximation (the representation of the continuous object with a set of particles), physical quantities as mass and inertia tensor are exact and trivial to compute, independent of geometry. At every pair wise interaction, a distinction is made: solid contact or fluid interface, corresponding to different contact forces being computed. By using a solid particle in the fluid equations, stresses are locally continuous and the solid-fluid interface is implicitly described.

The implementation of the numerical model is done on DualSPHysics, a collaborative, open source effort to produce a high-quality and high-performance code. The numerical complexity of particulate methods implies that large, repetitive calculations need to be performed. The CPU implementation shares much of the common strategies in parallel HPC codes. The GPU implementation however, demands unique novel solutions to be explored, in order to achieve runtimes compatible with the time scale of the problem at hand. The implementation for large machines using MPI was described, and the major difficulties of the unfinished MPI-CUDA version for rigid bodies were discussed.

Attempts at quantifying the quality of the obtained solutions considering exclusively the flows structure of a fluid flow were carried out. After an initial review of results obtained with DualSPHysics

from highly transient free-surface flows, low R_e flows with analytical solutions were studied:

- The laminar Hagen-Poiseuille and Couette flows provide a relevant metric of the accuracy of the method for flows where particles are not intensely disorganized. Since the flow is laminar most of the regular lattice, imposed as initial condition for position of the particles, is maintained, with slow deformations occurring;

- Error for these flows is in the 1% order, showing that the adopted Dynamic Boundary Conditions are capable of correctly reproducing a solid boundary for laminar flow conditions.

- The standard Smagorinsky approach to the eddy-viscosity is known to introduce a net stress even in laminar flows, were the SPS contribution should be null. The observed error hints that this value is residual and of no consequence to these computations.

The model is compared with non-traditional experimental dam break measurements. The velocity field on the dam break was recovered using a heavily modified PIV technique. The downward gate motion introduced interesting aspects in the experiments, since traditionally, upward gates are employed. The numerical solution follows the experimental conditions with precision: the same dimensions were used and the gate motion was reconstructed and rebuilt numerically. The numerical velocity fields present very good agreement with the experimental values, as well as the free-surface shape, along time. The largest deviations occur in the vertical velocity signal, where the largest doubts on the experimental procedure are also concentrated. The model is considered accurate and stable regarding fluid flows. The tests, spanning from internal laminar flows to free surface unsteady flows demonstrate the robustness of the model.

A series of validations in order to test the fluid-solid description are proposed:

- Free-stream consistency tests indicate that the integrator described in Section 3.4 is adequate to treat the two systems simultaneously, as expected. No errors are detected in the flow field, indicating that the interface is at least well balanced, no artificial repulsion-attraction forces are being developed in a free-stream regime;

- The effectiveness of the δ-SPH term is studied as a mechanism to curb the creation of an artificial density gradient across the interface, due to an unbalance on the kernel completeness;

- The model compares favorably to known solutions regarding free buoyancy problems with large density differences. The solutions are comparable to analytical solutions to simplified models and traditional mesh-based VOF results, indicating that the viscous terms seem to correctly function under large variations of R_e in very unsteady flows;

- Original experimental data on a settling sphere was compiled, allowing for direct comparisons of the behavior of the system. The results show an accurate solution is possible. It is hypothesized that, due to the small scale of the experimental set-up, forces such as surface tension may have more influence on the system and partly explain the error or the numerical solution;

7. Conclusions and Recommendations

- Studying the equilibrium position of floating bodies subjected exclusively to buoyant forces, an interesting property of the discretization and the implementation is discussed: the solution appears to naturally avert states other than global stable equilibrium. Considering the large number of computations involved every time-step, it is trivial to conceive a small truncation error resulting in a small force unbalance in the system. Adding to the effects of the dynamic scheduling of the paralelization of thousands of threads in a GPU, this small force contributes to the instabilization of a precarious local unstable equilibrium. The VOF code used as a reference used a user-defined force to promote the instabilization.

These results show that the treatment of solid-fluid interfaces seems to be effective. Discontinuous geometries were employed, not leading to erroneous behaviors. The accuracy of the treatment of the involved forces allow for confidence when using any geometry for a rigid body, assuming sufficient resolution.

Collision modeling is studied by recovering experimental data compiled by Kruggel-Emden et al. (2007), used to compare the dependency of the restitution coefficients on the impact velocity.

- The reproduced behavior is similar to the experimental data, for a sufficiently high impact velocity. The solutions corresponding to velocities lesser then $0.1 \, \mathrm{ms}^{-1}$ do not seem to fit the trend of the experimental data, that shows $e_n \rightarrow 1.0$ as $V_0 \rightarrow 0.0$. This behavior, expected to a certain degree as viscous, elastic waves and plastic deformation energy dissipation mechanisms depend on impact velocity, may be difficult to capture as it implies the recording of small velocities;

- For higher V_0, e_n seems to be correctly recovered. The model reproduces the restitution coefficients using known material parameters, and the viscous damper can be further calibrated, offering the possibility of fine-tuning the results for specific applications.

In an attempt to fulfill the core objectives of this dissertation, an experimental campaign was designed and carried out. A large scale dam break flow provided the highly unsteady setting, and cubes packed in complex configurations subjected to that flow were competent targets for modeling. The cubes introduced discontinuities in the flow, and were subjected to normal, friction, buoyant and drag forces. By employing several cameras and a series of markers, DTL algorithms provided a means to track individual cubes as they moved trough the flume.

- Single cube experiments, were the object is dragged in intermittent contact with the bottom of the flume, the correct recovery of the velocities implies that the net momentum transfer, considering both fluid forces and friction at the bottom, was mostly accurate;

- In a pile of objects, the cube in contact with the bed presented a delay in initiation of motion, independently of resolution. Since other objects do not show this behavior, it is hypothesized that the frictional spring over estimates the static friction, due to the weight of the top cubes;

- The top cube shows coherent behavior but an artifact is introduced in the vertical direction. The cube vibrates slightly, in what may be described as a consequence of the use of perfectly rigid

bodies: the viscous damper is insufficient to filter all of the high frequency oscillations that arise when the cubes bellow begin to move;

- A more elaborate configuration, the third set up showed that lateral motion in a cube not placed along the center line of the flume is well captured.

Overall, the results showed that the method is capable of providing accurate solutions to highly non-linear problems, where less flexible approaches would suffer greatly with the deformation and fragmentation of the free-surface, as well as the discontinuous geometry of the cubes. A PIV method allowed the derivation of the flow field immediately before the impact locus. The SPH solution presents the same flow structures, indicating that the fluid to solid momentum transfer occurs in a similar fashion, given enough resolution.

Chapter 6 provides an exploratory tour of actual scenarios where the application of the presented method may provide significant advantages. Most of all, these remain problems that, either by scale, complexity or both, are uncharted territory for resolved state-of-the art numerical solutions. The coastal geomorphology case, in Section 6.1, introduces an innovative view on a necessarily multi-disciplinary subject. The possibility of modeling events derived from recorded time series in real geometries opens a new field. The inverse problem of the one posed so far may now be studied, i.e., instead of mapping simplified conceptual models to the available data, specific events may be traced to configurations compatible with the ones currently observed. This simple shift entails the passing of a fitting technique to a descriptive tool, with prediction capabilities that may support future research directions, as well as decision making.

Section 6.2 embodies most of the questions raised by Section 6.1, applying them in a larger and more visible domain: an industrial and shipping harbor. Physical modeling is of extreme importance to the design of the harbors and sea protection, but that accounts exclusively for infrastructure. The proposed model was applied to a section of a real harbor, recreating realistic functioning conditions, at an infinitesimal fraction of the cost of physical modeling.

Finally, Section 6.3 takes a different stance. Experimental facilities are capable of reproducing averaged size debris flows, but, as previously discussed, measuring techniques are still difficult to put in place. Large amounts of data has been collected on global and macroscopic quantities of these flows: discharges, flow depths and average velocities. As such, the application of the present model stands between a novel application and a validation case. The model reproduced acceptably the available data, correctly recovering tendencies of retention rates by the checked-dam. In doing so, more information than available before on the mechanics of a debris flow was produced. New research prompts are bound to emerge, even considering the embryonic stage of the results.

7.2   Recommendations for Future Developments

The fluid discretization model presented in Chapter 3 is susceptible to a number of critiques. The WCSPH formulation depends on the δ-SPH term to stabilize the density field, and most importantly,

7. Conclusions and Recommendations

to mitigate the effects of persistent entropy jumps, as shown in Section 5.2.2.A. More robust δ-SPH terms are available (Antuono et al., 2012), at the expense of computational efficiency. Alternative implementation strategies could offset this cost, providing a balanced term that does not corrupt hydrostatic solutions and is less diffusive, better preserving steep gradients on the density field that are physically inspired. Regarding viscous stresses, the SPS formulation used in this work relies on the outdated Smagorisnky model for the eddy viscosity definition. A Wall-Adapting Local Eddy-Viscosity (WALE) model could be used, effectively tackling two problems at once. The turbulent viscosities would be null for laminar regions and wall bounded flows would have a better approximation of eddy viscosity near the wall, witout a stringing need for added resolution in that area.

Variable resolution models (Vacondio et al., 2013) could provide impressive gains in terms of resolving the boundary layers around objects and solid walls, while optimizing the computational cost of the simulations. These schemes require careful implementation to ensure that no bottlenecks are introduced in the computation, now with a possibly varying number of particles per time step.

Boundary conditions are a major difficulty in SPH models. The dynamic boundary conditions (Crespo et al., 2007), used in the current version of DualSPHysics and in this work, provide unparalleled simplicity, both conceptual and computational, but introduce serious artifacts in the simulation. New strategies to approach boundary integrals, making them computationally accessible, should be devised as well as for new ghost particle stencil methods (Fourtakas et al., 2014). This would apply both to static boundaries and also to moving boundaries, such as floating bodies.

Regarding the rigid bodies described in this work, important energy dissipating mechanisms are not being taken into account. Considering elasto-plastic bodies would potentially expand on the potential applications of the model. Elasticity equations could be solved by SPH (Cleary and Das, 2008), in parallel with the momentum equations, resulting in a unified method. Impressive results using local maximum-entropy approximation schemes (Arroyo and Ortiz, 2006; Ortiz et al., 2010), a recent class of meshless methods suitable for trivial coupling with SPH, could also lead to a promising model. Also regarding the solid phase, all of the bodies in this work have 6 DOF. The possibility to add kinematic restraints like joints and sliders would provide immediate support for mechanism simulations, with applications on fields such as renewable energy production. The integration of the DualSPHysics code with an HPC multiphysics library could provide efficient solutions.

A troubling issue with the presented model is the lack of effective lubrication forces between contacts once the distance between bodies is less than the fluid resolution. Potapov et al. (2001) mentioned that only *ad-hoc* ideas would be able to complete the model, such as the ones used in Kempe and Fröhlich (2012).

Regarding implementation issues, the MPI version of the code with floating bodies is not operational. The topological connectivity constraints that a body crossing between processes poses were exposed in Chapter 4. Further optimizations are required and are under way.

Bibliography

Adams, G. and M. Nosonovsky (2000). Contact modeling-forces. *Tribology International 33*(5), 431–442.

Aleixo, R. (2013). *Experimental Study of the Early Stages of a Dam-Break Flow Over Fixed and Mobile Beds*. Ph. D. thesis, Universite catholique de Louvain.

Aleixo, R., S. Soares-Frazao, and Y. Zech (2011). Velocity-field measurements in a dam-break flow using a ptv voronoi imaging technique. *Experiments in Fluids 50*, 1633–1649.

Antuono, M., A. Colagrossi, and S. Marrone (2012). Numerical diffusive terms in weakly-compressible sph schemes. *Computer Physics Communications 189*.

Antuono, M., A. Colagrossi, S. Marrone, and D. Molteni (2010). Free-surface flows solved by means of sph schemes with numerical diffusive terms. *Computer Physics Communications 181*(3), 532 – 549.

Aris, R. (1962). *Vectors, Tensors and the Basic Equations of Fluid Mechanics*. Dover Publications, INC.

Armanini, A., L. Fraccarollo, and M. Larcher (2008). Liquid-granular channel flow dynamics. *Powder Technology 182*(2), 218 – 227. Granular Temperature.

Arroyo, M. and M. Ortiz (2006). Local maximum-entropy approximation schemes: a seamless bridge between finite elements and meshfree methods. *International Journal for Numerical Methods in Engineering 65*(13), 2167–2202.

Ayachit, U. (2015). The paraview guide: A parallel visualization application.

Bagnold, R. (1954). Experiments on a gravity-free dispersion of large solid spheres in a newtonian fluid under shear. *Proc. of the Royal Soc. of London 225*(1160), 49–63.

Baptista, M. A., J. M. Miranda, R. Omira, and C. Antunes (2011). Potential inundation of lisbon downtown by a 1755-like tsunami. *Natural Hazards and Earth System Science 11*(12), 3319–3326.

Batchelor, G. K. (2000). *An Introduction to Fluid Dynamics*. Cambridge University Press.

Brilliantov, N. and T. Pöschel (2001). Granular gases with impact-velocity-dependent restitution coefficient. In T. Pöschel and S. Luding (Eds.), *Granular Gases*, Volume 564 of *Lecture Notes in Physics*, pp. 100–124. Springer Berlin Heidelberg.

Bibliography

Brilliantov, N. V., F. Spahn, J.-M. Hertzsch, and T. Pöschel (1996, May). Model for collisions in granular gases. *Phys. Rev. E 53*, 5382–5392.

Brookshaw, L. (1985). A method of calculating radiative heat diffusion in particle simulations. *Proceedings of the Astronomical Society of Australia 6*, 207–210.

Calantoni, J., K. T. Holland, and T. G. Drake (2004). Modelling sheet flow sediment transport in wave bottom boundary layers using discrete element modelling. *Philosophical Transactions of the Royal Society of London A: Mathematical, Physical and Engineering Sciences 362* (1822), 1987–2001.

Campbell, C. S. (2006). Granular material flows - an overview. *Powder Technology 162*, 208 – 229.

Campbell, C. S. and C. E. Brennen (1985). Chute flows of granular material: Some computer simulations. *Journal of Applied Mechanics 52(1)*, 172–178.

Canelas, R., A. Crespo, J. Domínguez, and R. Ferreira (2013). A generalized SPH-DEM discretization for the modelling of complex multiphasic free surface flows. In 8th *international SPHERIC workshop*.

Canelas, R., A. Crespo, J. Domínguez, R. Ferreira, and M. Góimez-Gesteira (2015). SPH-DCDEM model for arbitrary geometries in free surface solid-fluid flows. *Computer Physics Communications Submitted*.

Canelas, R., J. Domínguez, A. Crespo, and R. Ferreira (2014). Modelling of wave impacts on harbour structures and objects with SPH and DEM. In 9th *international SPHERIC workshop*.

Canelas, R., J. Domínguez, A. Crespo, M. Gómez-Gesteira, and R. Ferreira (2015). A smooth particle hydrodynamics discretization for the modelling of free surface flows and rigid body dynamics. *International Journal for Numerical Methods in Fluids* (in press).

Canelas, R., J. Domínguez, and R. Ferreira (2013, June). Coupling a generalized DEM and an SPH models under a heterogeneous massively parallel framework. In SEMNI (Ed.), *CMN 2013*.

Capart, H., D. L. Young, and Y. Zech (2002). Voronoï imaging methods for the measurement of granular flows. *Experiments in Fluids 32*, 121–135.

Capel, D., A. Fitzgibbon, P. Kovesi, T. Werner, Y. Wexler, and A. Zisserman. Matlab functions for multiple view geometry.

Cleary, P. W. (1996). New implementation of viscosity: Tests with Couette flows. Technical report, CSIRO Division of Maths and Stats, Tech. Report DMS - C 96/32.

Cleary, P. W. (2014). Prediction of coupled particle and fluid flows using DEM and SPH. *Minerals Engineering*.

Cleary, P. W. and R. Das (2008). The potential for SPH modelling of solid deformation and fracture. In *IUTAM symposium on theoretical, computational and modelling aspects of inelastic media*, pp. 287–296. Springer.

Colagrossi, A., M. Antuono, A. Souto-Iglesias, and D. Le Touzé (2011). Theoretical analysis and numerical verification of the consistency of viscous smoothed-particle-hydrodynamics formulations in simulating free-surface flows. *Phys. Rev. E 84*.

Colagrossi, A. and M. Landrini (2003). Numerical simulation of interfacial flows by smoothed particle hydrodynamics. *Journal of Computational Physics 191*, 448–475.

Costa, P., C. Andrade, M. Freitas, M. Oliveira, R. Taborda, and C. Silva (2008). High energy boulder deposition in barranco and furnas lowlands, western algarve (south portugal). In *Proc. 2nd Intern. Tsunami Field Symposium*, pp. 19–22.

Crespo, A., J. Domínguez, A. Barreiro, M. Gómez-Gesteira, and B. Rogers (2011). GPUs, a new tool of acceleration in CFD: Efficiency and reliability on smoothed particle hydrodynamics methods. *PLoS ONE 6(6)*.

Crespo, A., J. Domínguez, B. Rogers, M. Gómez-Gesteira, S. Longshaw, R. Canelas, R. Vacondio, A. Barreiro, and O. García-Feal (2015). Dualsphysics: open-source parallel CFD solver on smoothed particle hydrodynamics (SPH). *Computer Physics Communications 187*, 204–216.

Crespo, A., J.-C. Marongiu, E. Parkinson, M. Gómez-Gesteira, and J. Domínguez (2009). High performance of SPH codes: Best approaches for efficient parallelization on GPU computing. In *4th SPHERIC Int. Workshop*.

Crespo, A. J. C., M. Gomez-Gesteira, and R. A. Dalrymple (2007). Boundary conditions generated by dynamic particles in SPH methods. *Computers, Materials, & Continua 5*(3), 173–184.

Crowe, C., J. Schwarzkopf, M. Sommerfeld, and Y. Tsuji (1998). *Multiphase Flows with Droplets and Particles*. CRC Press.

Cummins, S. J. and P. W. Cleary (2011). Using distributed contacts in DEM. *Applied Mathematical Modelling 35*(4), 1904 – 1914.

Dalrymple, R. and B. Rogers (2006). Numerical modeling of water waves with the SPH method. *Coastal Engineering 53*(2-3), 141 – 147. Coastal Hydrodynamics and Morphodynamics.

Dalrymple, R. A. and O. Knio (2000). SPH modelling of water waves. In *Proc. Coastal Dynamics*.

Dean, R. G. and R. A. Dalrymple (1991). *Water Wave Mechanics for Engineers and Scientists*. World Scientific.

Dehnen, W. and H. Aly (2012). Improving convergence in smoothed particle hydrodynamics simulations without pairing instability. *Monthly Notices of the Royal Astronomical Society 425*(2), 1068–1082.

Domínguez, J., A. Crespo, A. Barreiro, M. Gómez-Gesteira, and A. Mayrhofer (2011). Development of a new pre-processing tool for sph models with complex geometries. In *6th International SPHERIC workshop, ISBN*, Volume 978, pp. 117–124.

Bibliography

Domínguez, J., A. Crespo, and M. Gómez-Gesteira (2013). Optimization strategies for cpu and gpu implementations of a smoothed particle hydrodynamics method. *Computer Physics Communications 184*(3), 617–627.

Domínguez, J., A. Crespo, M. Gómez-Gesteira, and J. Marongiu (2011). Neighbour lists in smoothed particle hydrodynamics. *International Journal for Numerical Methods in Fluids 67*(12), 2026–2042.

Domínguez, J., A. Crespo, D. Valdez-Balderas, B. Rogers, and M. Gómez-Gesteira (2013). New multi-gpu implementation for smoothed particle hydrodynamics on heterogeneous clusters. *Computer Physics Communications*.

Douxchamps, D., B. Spinewine, H. Capart, Y. Zech, and B. Macq (2002). Particle-based imaging methods for the characterisation of complex fluid flows. In *Proc of the IEEE Oceans Conf.*

Drazin, P. and N. Riley (2006). *The Navier-Stokes equations: a classification of flows and exact solutions.* Cambridge University Press.

Ellero, M. and N. Adams (2011). Sph simulations of flow around a periodic array of cylinders confined in a channel. *International Journal for Numerical Methods in Engineering 86*(8), 1027–1040.

Evans, M. W., F. H. Harlow, and E. Bromberg (1957). The particle-in-cell method for hydrodynamic calculations. Technical report, DTIC Document.

Fekken, G. (2004). *Numerical simulation of free surface flow with moving rigid bodies.* Ph. D. thesis, University of Groningen.

Ferrand, M., D. Laurence, B. Rogers, D. Violeau, and C. Kassiotis (2013). Unified semi-analytical wall boundary conditions for inviscid, laminar or turbulent flows in the meshless sph method. *International Journal for Numerical Methods in Fluids 71*(4), 446–472.

Ferreira, R. M. (2011). Turbulent flow hydrodynamics and sediment transport: Laboratory research with lda and piv. In *Experimental Methods in Hydraulic Research*, pp. 67–111. Springer.

Fourtakas, G., J. Dominguez, R. Vacondio, A. Nasar, and B. Rogers (2014). Local uniform stencil (lust) boundary conditions for 3-d irregular boundaries in dualsphysics. In *Proc. 9th Int. SPHERIC Workshop, Paris*, pp. 103–110.

Frank, W. (1967, October). Oscillation of cylinders in or below the free surface of deep fluids. Technical Report 2375, Naval Ship research and Development Center, Hydromechanics Laboratory.

Fukushima, E. (1999). Nuclear magnetic resonance as a tool to study flow. *Annual Review of Fluid Mechanics 31*(1), 95–123.

Gingold, R. and J. Monaghan (1977). Smoothed particle hydrodynamics - theory and application to non-spherical stars. *Monthly Notices of the Royal Astronomical Society 181*, 375–389.

Gingold, R. and J. Monaghan (1982). Kernel estimates as a basis for general particle methods in hydrodynamics. *Journal of Computational Physics 46*(3), 429 – 453.

Gómez-Gesteira, M., B. Rogers, A. Dalrymple, R., and A. Crespo (2010). State-of-the-art of classical sph for free-surface flows. *Journal of Hydraulic Research 48*, 6–27.

Gonzàlez, L. M., J. M. Sánchez, F. Macià, and A. Souto-Iglesias (2009). Analysis of WCSPH laminar viscosity models. In *4th ERCOFTAC SPHERIC workshop on SPH applications*.

Gotoh, H., T. Shibahara, and T. Sakai (2001). Sub-particle-scale turbulence model for the MPS method - Lagrangian flow model for hydraulic engineering. *Advanced Methods for Computational Fluid Dynamics 9-4*, 339–347.

Hertz, H. R. (1882). *Ueber die Beruehrung elastischer Koerper (On Contact Between Elastic Bodies)*, Volume 1. Leipzig, Germany.

Hoomans, B. (2000, January). *Granular dynamics of gas-solid two-phase flows*. Ph. D. thesis, University of Twente, Enschede.

Idelsohn, S. R., E. Oñate, and F. D. Pin (2004). The particle finite element method: a powerful tool to solve incompressible flows with free-surfaces and breaking waves. *International journal for numerical methods in engineering 61*(7), 964–989.

Issa, R. (2004). *Numerical assessment of the Smoothed Particle Hydrodynamics gridless method for incompressible flows and its extension to turbulent flows*. Ph. D. thesis, UMIST.

Johnson, K. L. (1987). *Contact mechanics*. Cambridge university press.

Johnson, K. L., K. Kendall, and A. D. Roberts (1971). Surface energy and the contact of elastic solids. *Proc. R. Soc. London*, 301–3013.

Joseph, G., R. Zenit, M. Hunt, and A. Rosenwinkel (2001). Particle–wall collisions in a viscous fluid. *Journal of Fluid Mechanics 433*, 329–346.

Kain, C., C. Gomez, and A. Moghaddam (2012). Comment on reassessment of hydrodynamic equations: Minimum flow velocity to initiate boulder transport by high energy events (storms, tsunamis), by n.a.k. nandasena, r. paris and n. tanaka [marine geology 281, 70-84]. *Marine Geology 319-322*(0), 75–76.

Kempe, T. and J. Fröhlich (2012, 10). Collision modelling for the interface-resolved simulation of spherical particles in viscous fluids. *Journal of Fluid Mechanics 709*, 445–489.

Koshizuka, S., A. Nobe, and Y. Oka (1998). Numerical analysis of breaking waves using the moving particle semi-implicit method. *International Journal for Numerical Methods in Fluids 26*, 751–769.

Kruggel-Emden, H., E. Simsek, S. Rickelt, S. Wirtz, and V. Scherer (2007). Review and extension of normal force models for the discrete element method. *Powder Technology 171*(3), 157 – 173.

Kuwabara, G. and K. Kono (1987). Restitution coefficient in a collision between two spheres. *Japanese Journal of Applied Physics 26*(8R), 1230.

Bibliography

Lauber, G. and W. H. Hager (1998). Experiments to dambreak wave: Horizontal channel. *Journal of Hydraulic Research 36*(3), 291–307.

Lee, E., D. Violeau, R. Issa, and S. Ploix (2010). Application of weakly compressible and truly incompressible sph to 3d water collapse in waterworks. *Journal of Hydraulic Research 48*.

Lemieux, M., G. Leonard, J. Doucet, L. Leclaire, F. Viens, J. Chaouki, and F. Bertrand (2008). Large-scale numerical investigation of solids mixing in a v-blender using the discrete element method. *Powder Technology 181*(2), 205 – 216.

Lemonnier, H. (2010). Nuclear magnetic resonance: A new tool for the validation of multiphase multidimensional cfd codes. *Nuclear Engineering and Design 240*(9), 2139–2147.

Liu, G. (2003). *Mesh Free methods: Moving beyond the finite element method.* CRC Press.

Lo, E. and S. Shao (2002). Simulation of near-shore solitary wave mechanics by an incompressible sph method. *Applied Ocean Research 24*, 275–286.

Lucy, L. B. (1977). A numerical approach to the testing of the fission hypothesis. *Astronomical Journal 82*, 1013–1024.

Macià, F., A. Colagrossi, M. Antuono, and A. Souto-Iglesias (2011). Benefits of using a wendland kernel for free-surface flows. In *6th ERCOFTAC SPHERIC workshop on SPH applications*, pp. 30–37. Hamburg University of Technology.

Martin, M. P., U. Piomelli, and G. V. Candler (2000). Subgrid-scale models for compressible large-eddy simulations. *Theoretical and Computational Fluid Dynamics 13*(5), 361–376.

Mayrhofer, A., M. Ferrand, C. Kassiotis, D. Violeau, and F.-X. Morel (2015). Unified semi-analytical wall boundary conditions in sph: analytical extension to 3-d. *Numerical Algorithms 68*(1), 15–34.

Molteni, D. and A. Colagrossi (2009). A simple procedure to improve the pressure evaluation in hydrodynamic context using the sph. *Comput. Phys. Comm 180*, 861–872.

Monaghan, J. (1989, May). On the problem of penetration in particle methods. *Journal of Computational Physics 82*, 1–15.

Monaghan, J. (1992). Smoothed particle hydrodynamics. *Annual Review of Astronomy and Astrophysics*.

Monaghan, J. (2005). Smoothed particle hydrodynamics. *Reports on Progress in Physics 68*(8), 1703.

Monaghan, J. (2006, January). Smoothed particle hydrodynamic simulations of shear flow. *Monthly Notices of the Royal Astronomical Society 365*, 199–213.

Monaghan, J., A. Kos, and N. Issa (2003). Fluid motion generated by impact. *J. Waterway, Port, Coastal, Ocean Eng. 129(6)*, 250–259.

Monaghan, J. J. and A. Kos (1999). Solitary waves on a cretan beach. *Journal of Waterway, Port, Coastal and Ocean Engineering 125*.

Morris, J. P., P. J. Fox, and Y. Zhu (1997). Modeling low reynolds number incompressible flows using SPH. *Journal of Computational Physics 136*(1), 214 – 226.

Moyo, S. and M. Greenhow (2000). Free motion of a cylinder moving below and through a free surface. *Applied Ocean Research 22*, 31–44.

Nandasena, N., R. Paris, and N. Tanaka (2011). Reassessment of hydrodynamic equations: Minimum flow velocity to initiate boulder transport by high energy events (storms, tsunamis). *Marine Geology 281*(1-4), 70–84.

Nott, J., J. and E. Bryant (2003). Extreme marine inundations (tsunamis?) of coastal western australia. *J. Geology* (111), 691–706.

Oertel, M. and D. B. Bung (2012). Initial stage of two-dimensional dam-break waves: laboratory versus vof. *Journal of Hydraulic Research 50*(1), 89–97.

Oger, G., M. Doring, B. Alessandrini, and P. Ferrant (2007). An improved sph method: Towards higher order convergence. *Journal of Computational Physics 225*(2), 1472–1492.

Oliveira, M., C. Andrade, M. Freitas, P. Costa, R. Taborda, C. Janardo, and R. Neves (2011). Transport of large boulders quarried from shore platforms of the portuguese west coast. *Journal of Coastal Research 64*, 1871–1875.

Oñate, E., S. R. Idelsohn, F. Del Pin, and R. Aubry (2004). The particle finite element method-an overview. *International Journal of Computational Methods 1*(02), 267–307.

Ortiz, A., M. Puso, and N. Sukumar (2010). Maximum-entropy meshfree method for compressible and near-incompressible elasticity. *Computer Methods in Applied Mechanics and Engineering 199*(25), 1859–1871.

Peskin, C. S. (1977). Numerical analysis of blood flow in the heart. *Journal of computational physics 25*(3), 220–252.

Pope, S. B. (2000). *Turbulent Flows*. Cambridge: Cambridge University Press.

Potapov, A. V., M. L. Hunt, and C. S. Campbell (2001). Liquid-solid flows using smoothed particle hydrodynamics and the discrete element method. *Powder Technology 116*(2-3), 204 – 213.

Price, D. (2008). Modelling discontinuities and Kelvin Helmholtz instabilities in SPH. *Journal of Computational Physics 227*, 10040–10057.

Prosperetti, A. and G. Tryggvason (2007). *Computational methods for multiphase flow*. Cambridge university press.

Bibliography

Quinlan, N. J., M. Basa, and M. Lastiwka (2006). Truncation error in mesh-free particle methods. *International Journal for Numerical Methods in Engineering 66*(13), 2064–2085.

Randles, P. and L. Libersky (1996). Smoothed particle hydrodynamics: Some recent improvements and applications. *Computer Methods in Applied Mechanics and Engineering 139*(1-4), 375–408.

Remaitre, A.and van Asch, T. J., J. P. Malet, and O. Maquaire (2008). Influence of check dams on debris-flow run-out intensity. *Natural Hazards and Earth System Sciences* (8), 1403–1416.

Robinson, M., M. Ramaioli, and S. Luding (2014). Fluid particle flow simulations using two-way-coupled mesoscale sph-dem and validation. *International Journal of Multiphase Flow 59*, 121–134.

Rogers, B., R. Dalrymple, and P. Stansby (2010). Simulation of caisson breakwater movement using 2-D SPH. *Journal of Hydraulic Research 48*, 135–141.

Saitoh, T. and J. Makino (2013, May). A Density-independent Formulation of Smoothed Particle Hydrodynamics. *The Astrophysical Journal 768*, 44.

Scheffers, A. and D. Kelletat (2005). Tsunami relics on the coastal landscape west of lisbon, portugal. *Science of Tsunami Hazards 23*(1), 3–16.

Shäfer, J., S. Dippel, and D. E. Wolf (1996). Force schemes in simulations of granular materials. *Journal de Physique I, EDP Sciences*, 5–20.

Shu, C., J. Xia, R. Falconer, and B. Lin (2011). Incipient velocity for partially submerged vehicles in floodwaters. *Journal of Hydraulic Research 49*.

Silva, M., S. Costa, and A. H. Cardoso (2015). Slit check-dams for stony type debris flows mitigation. experimental study to evaluate sediment control efficiency. In *Second International Dam World Conference*.

Spinewine, B., H. Capart, M. Larcher, and Y. Zech (2003). Three-dimensional voronoï imaging methods for the measurement of near-wall particulate flows. *Experiments in Fluids 34*(2), 227–241.

Spinewine, B. and Y. Zech (2007). Small-scale laboratory dam-break waves on movable beds. *Journal of Hydraulic Research 45*(sup1), 73–86.

Stoker, J. (1957). *Water waves. The mathematical theory with applications.* Interscience Publishers.

Swegle, J., D. Hicks, and S. Attaway (1995). Smoothed particle hydrodynamics stability analysis. *Journal of Computational Physics 116*(1), 123 – 134.

Truesdell, C. (1954). *The kinematics of vorticity.* Bloomington: Indiana University Press.

Vacondio, R., B. Rogers, P. Stansby, P. Mignosa, and J. Feldman (2013). Variable resolution for sph: A dynamic particle coalescing and splitting scheme. *Computer Methods in Applied Mechanics and Engineering 256*, 132–148.

Vetsch, D. (2011). *Numerical Simulation of Sediment Transport with Meshfree Methods*. Ph. D. thesis, ETH Zurich.

Violeau, D. (2012). *Fluid Mechanics and the SPH method: theory and applications*. Oxford University Press.

Violeau, D. and R. Issa (2007). Numerical modelling of complex turbulent free-surface flows with the sph method: an overview. *International Journal for Numerical Methods in Fluids 53*(2), 277–304.

Wenbing, H. & Guoqiang, O. (2006). Efficiency of slit dam prevention against non-viscous debris flow. *Wuhan University Journal of Natural Sciences 11*, 865–869.

Wendland, H. (1995). Piecewise polynomial, positive definite and compactly supported radial functions of minimal degree. *Advances in Computational Mathematics 4*(1), 389–396.

Yang, F.-L. and M. L. Hunt (2006). Dynamics of particle-particle collisions in a viscous liquid. *Physics of Fluids 18*.

Yoshizawa, A. (1986). Statistical theory for compressible turbulent shear flows, with the application to subgrid modeling. *Physics of Fluids (1958-1988) 29*(7), 2152–2164.

Zel'dovich, Y. and Y. P. Raizer (1967). *Physics of Shock Waves and High-Temperature Hydrodynamic Phenomena*. Academic Press.

Zeng, Q. L., Z. Q. Yue, Z. F. Yang, and X. J. Zhang (2008). A case study of long term field performance of check-dams in mitigation of soil erosion in jiangjia stream, China. *Environmental Geology* (58), 897–911.

Bibliography